Models for Instabilities of Fronts

by

Alan Mohammed Omar

Thesis submitted to The University of Nottingham

for the degree of Doctor of Philosophy

2020

THE UNIVERSITY OF NOTTINGHAM

PHD. THESIS

Abstract

Understanding the characteristics of interface motion and front propagation is an important feature in many scientific areas such as invasive species, avalanche, combustion, solidification and many other industrial processes. This thesis is concerned with introducing, investigating, solving and discussing some models for the front instabilities that suit the shapes of fronts observed in applications better than the Kuramoto-Sivashinsky equation. Our attention has been focused on dealing with three systems that have the growth rate proportional to $|k|$ for small wavenumber k, where the front dynamics takes different shapes such as lobe-and-cleft patterns. These systems are the nonlocal Kuramoto-Sivashinsky (nonlocal KS), Michelson-Sivashinsky (MS) and modified Michelson-Sivashinsky (MMS) equations.

In this work, we examine all three systems numerically in one and two dimensions, varying the domain size. For a small domain in one dimension, the dynamics of the front for all three systems shows coarsening from initial disturbances until it reaches a stable steady state solution with one cusp. The dynamics of the front for the MS and MMS equations in a large domain coarsens from initial disturbances until it reaches a state with a few cusps. Then this state seems to be unstable and new small cusps appear in the troughs and move toward the large cusps. The dynamics of the front for the nonlocal-KS equation in a large domain shows similar behaviour, but with a small nonlocal term is fully unstable with no coherent structure. In addition, travelling wave and heteroclinic cycle solutions between the large and small domains have been found for the nonlocal-KS equation. The dynamics of the front in two dimensions has similar behaviour to the one-dimensional case for all three systems. The most novel finding of this work is a family of analytical solutions of the MS equation in one and two dimensions.

Declaration

I declare that the work in this thesis was carried out in accordance with the regulations of the University of Nottingham. The work is original and has not been submitted for any other degree at the University of Nottingham or elsewhere.

Name: Alan Mohammed Omar

Signature:

Date: 2020

Acknowledgements

First and foremost, I would like to express my sincere gratitude to my supervisors, **Dr. Paul Matthews** and **Dr. Stephen Cox**, for their unlimited support, patience, motivation, and immense knowledge. Their guidance helped me in all the time of research and writing of this thesis. I could not have imagined having better advisors and mentors for my PhD study. Without their insightful commentary, this thesis would never have been completed.

I would also like to thank all staff of the School of Mathematical Sciences of the University of Nottingham for their support, help, and advice.

I am deeply grateful to The Higher Committee for Education Development in Iraq for offering me this scholarship and for their financial support during my study.

Finally, many thanks to my family and friends, who have supported and encouraged me throughout writing this thesis and my life in general.

Contents

1 Introduction and literature review **1**

1.1 Introduction 2

1.2 Examples of front propagation 2

1.2.1 Hele-Shaw cells 2

1.2.2 Muskrat invasion 3

1.2.3 Avalanche 4

1.2.4 Combustion 6

1.2.5 Solidification 8

1.3 History of front propagation 9

1.4 Reaction-diffusion systems 11

1.5 Kuramoto-Sivashinsky equation 14

1.6 Systems with $O(k)$ growth rate 17

1.7 Thesis aims and objectives 21

1.8 Discussion of Michelson-Sivashinsky equation 22

1.9 Previous work on MS equation 24

2 Numerical solutions of nonlocal front equations **26**

2.1 Introduction 27
2.2 The scaling of nonlocal front equations 27
2.2.1 Nonlocal-KS equation 27
2.2.2 The Michelson-Sivashinsky (MS) equation 29
2.2.3 The Modified Michelson-Sivashinsky (MMS) equation 29
2.3 Dispersion relation of nonlocal front equations 30
2.4 Numerical study of nonlocal front models 35
2.4.1 Numerical method 35
2.4.2 Numerical results 36
2.4.3 Speed of front 51
2.5 Conclusion 54

3 Approximate analytical solution of nonlocal front equations by using Fourier series 57
3.1 Introduction 58
3.2 Approximate analytical solutions by using three and four modes Fourier series 58
3.2.1 Nonlocal-KS equation 59
3.2.2 MS equation 65
3.2.3 MMS equation 68
3.3 Approximate analytical solutions by using general form of Fourier series 70
3.4 Approximate analytical solutions by using complex Fourier series . . . 79
3.5 Conclusion 86

4 Analytical solution of the MS equation 88
4.1 Introduction 89

4.2 Infinite case . . . 91
4.3 Periodic case . . . 96
4.4 Conclusion . . . 109

5 Solutions of all three nonlocal-KS, MS and MMS systems in 2D 111
5.1 Introduction . . . 112
5.2 Numerical solution of the MS equation in two dimensions . . . 112
5.2.1 Numerical method . . . 113
5.2.2 Numerical results . . . 114
5.2.3 Speed of the front . . . 123
5.3 Analytical solution of the MS equation in two dimensions . . . 123
5.4 Weakly nonlinear analysis . . . 128
5.5 Numerical solution of the nonlocal-KS and MMS equations in two dimensions . . . 133
5.5.1 The nonlocal-KS equation in two dimensions . . . 133
5.5.2 The MMS equation in two dimensions . . . 136
5.6 Conclusion . . . 140

6 Conclusions and further work 143
6.1 Conclusions . . . 144
6.2 Further work . . . 148

Bibliography 149

Chapter 1

Introduction and literature review

1.1 Introduction

An interface is a common phenomenon in nature and has attracted the attention of scientists for many years [4, 14, 29, 44, 61, 72]. It is commonplace in biology, ecology, chemistry, physics and various interdisciplinary. An interface is a boundary between two forms of matter, it appears whenever at least two non-equilibrium physical or chemical states connect. For example, the boundary between glass beaker and water is a solid-liquid interface, whereas between the air and water in a glass of water is a gas-liquid interface and two immiscible liquids form a liquid-liquid interface. The moving of an interface, shown in the time progression of a system, resulting in an invasion of one matter into the other is usually called a front. The theory of front propagation is one of the main problems in non-equilibrium systems and plays an important role in many real-life applications which involve separating different phases. In order to better understand the phenomenon of front propagation, a few simple examples in nature are explained in the next section.

1.2 Examples of front propagation

1.2.1 Hele-Shaw cells

A well-known example of front propagation is seen in Hele-Shaw cells, which describe a flow between two parallel plates separated by a very small gap [13, 25, 58, 62]. Suppose that a low-viscosity fluid, for example air, has been pumped in a Hele-Shaw cell containing viscous fluid, for instance oil, at one of the ends of the Hele-Shaw cell. The moving planar interface between air and oil with constant velocity is unstable. Initially many fingers of air, which are unstable pattern formations of the interface similar to human fingers, are created. Then one of the fingers develops more than

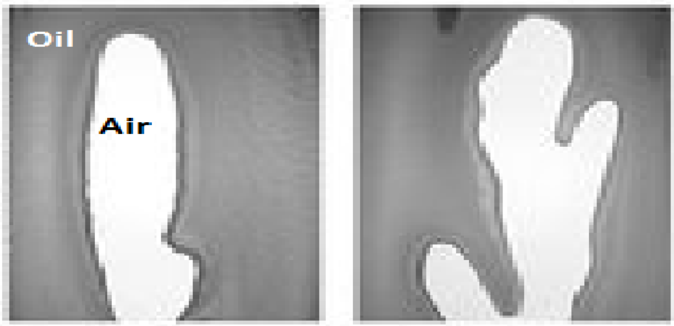

Figure 1.1: Viscous fingering occurring during the injection of air into Hele-Shaw cell filled with oil [63].

the others and then moves with constant velocity and stationary shape. For larger air pressure, other fingers are formed either on the side of the main finger or splitting from the tip of it. This type of front is referred to as fingering front propagation, figure 1.1.

1.2.2 Muskrat invasion

Invasive species are non-native organisms to a specific location (an introduced species) and that have a tendency to adapt and spread in the new area [46]. They are often considered a serious threat to the environment, human economy, human health and other species. The lack of natural predators allows populations of these species to grow very rapidly. They are not just animals and plants, bacteria can also be invasive species which cause invasive disease. There are many examples of species invasion such as the invasion of brown snake tree [21], ash dieback [28], epidemics [30] and muskrats [70]. The scenario of muskrats is an ecological diffusion example. The muskrat is an animal originally from the north of America which did not exist in Europe. A few of them were accidentally transferred to Central Europe, now the Czech Republic, at the beginning of the 20th century. They reproduced

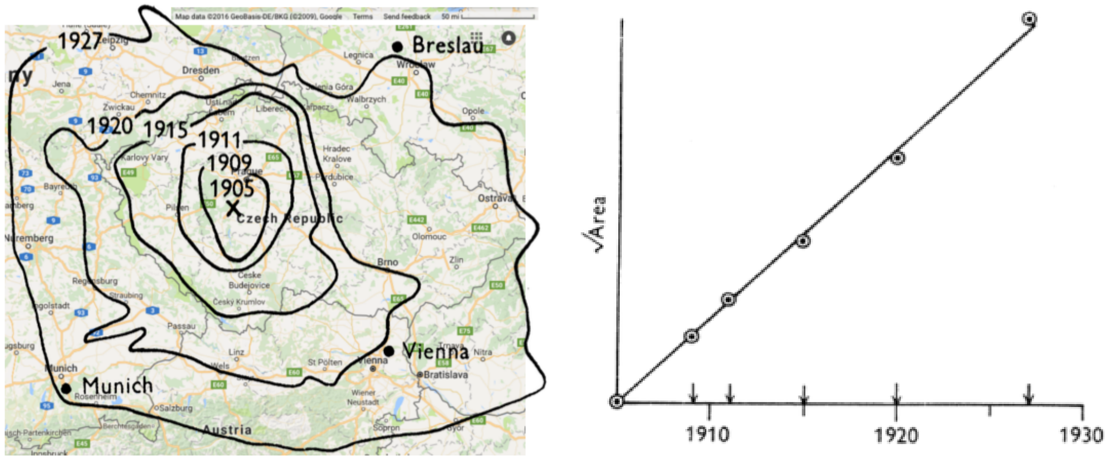

(a) (b)

Figure 1.2: The diffusion of the muskrat in central Europe since its introduction [70].

and became an invasive species in that area and they nowadays number in millions. In 1951 [70], Skellam introduced a mathematical model to investigate the spread of this species from 1905-1927, figure 1.2(a). Although muskrats have spread randomly because of the natural obstacles such as mountains, rivers and so on, he found by his theoretical study that the square root of the contour's area increases linearly in time, figure 1.2(b). The moving of the contour in this example can be considered as non-regular front propagation.

1.2.3 Avalanche

One of the examples of nature in front propagation is a snow avalanche, which is an extremely dangerous and destructive natural phenomenon [56, 59]. Snow avalanche accidents involving damages of life and properties have often happened in the past. Thus the study of avalanche dynamics became a topic of scientists concerned to avoid the danger induced by the avalanche. An avalanche begins when a slab of

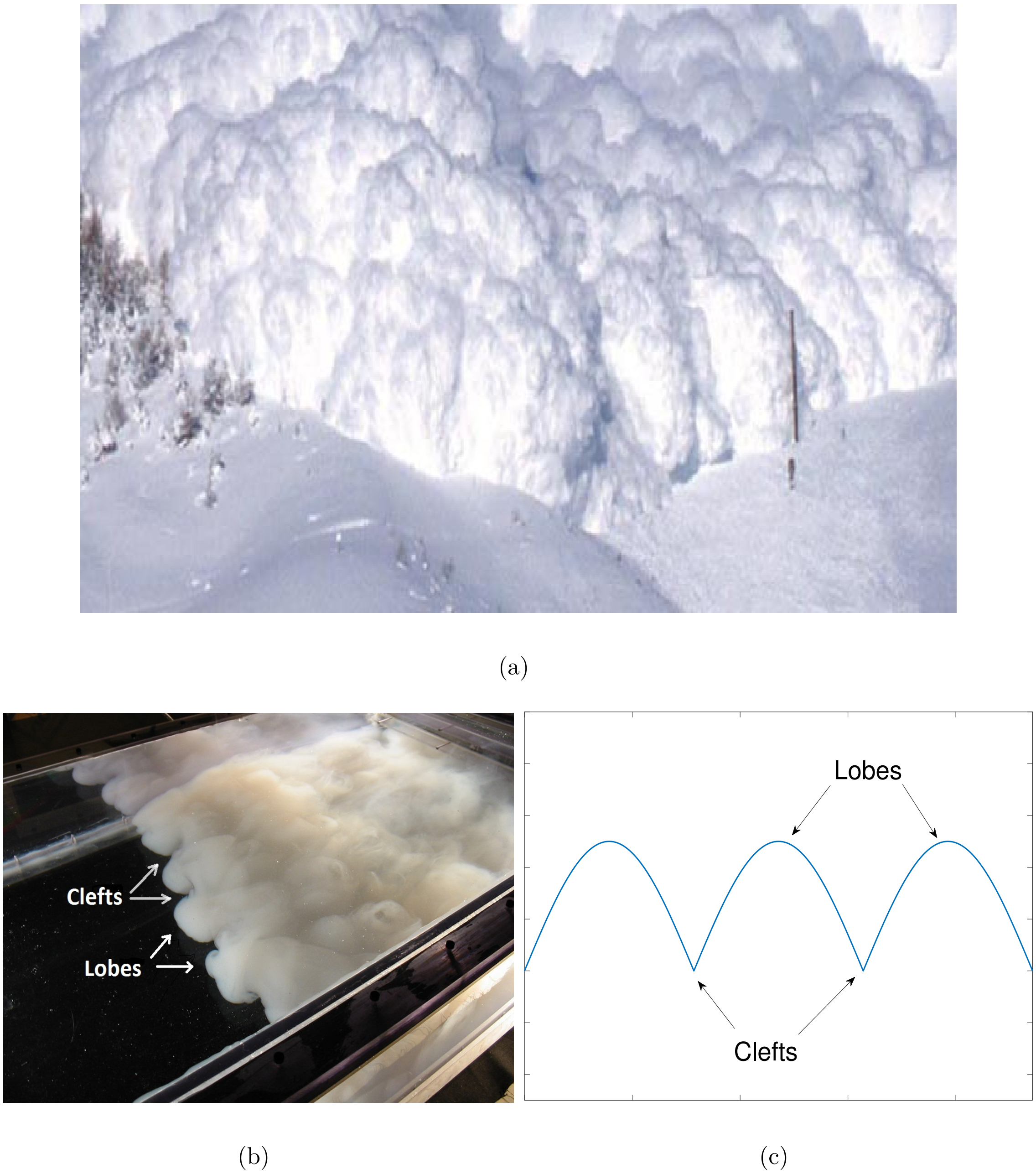

Figure 1.3: Lobe-and-cleft type patterns at the front of: (a) a natural powder snow avalanche, [52], (b) a laboratory-scale homogeneous particle-laden gravity current, [56], (c) the lobe-and-cleft diagram.

snow breaks or the cohesion of snow grains reduces and creates smaller particles. During the initial period of movement, it is considered as a laminar motion like the laminar fluid. However, the speed increases quickly and the motion becomes turbulent. The smallest particles of snow mix with air at the front of the avalanche. These particles move and create a structure of the lobe-and-cleft pattern. In this case, it can be considered as a lobe-cleft front propagation, figure 1.3(c), which is the pattern that also can be seen at the leading edge of gravity currents, figure 1.3(b).

1.2.4 Combustion

People have always been fascinated by combustion and fire since ancient times. Combustion is one of the most important phenomena for human civilization [44, 45]. Although it has dangerous effects such as pollutants, greenhouse gases which cause global warming, unwanted fires and explosions, figure 1.4, nowadays it has a wide variety of uses in industrial applications. Scientifically speaking, combustion is a chemical process of burning a substance to produce energy in the form of heat and light. Industry has made fantastic progress in the development and production of engines over the past one and a half centuries. The Industrial Revolution accelerated the process of using combustion, in particular, it generated such a powerful source of energy as burning of turbulent gases in internal combustion engines, especially in transportation. There are major applications of combustion in our daily life, for instance, two simple applications are cooking food and heating houses. In general, nowadays combustion is utilized in heating devices, explosives, internal-combustion engines and chemical reactions. Flames have a complex composition.

Figure 1.4: Fires in Amazon rainforest [76].

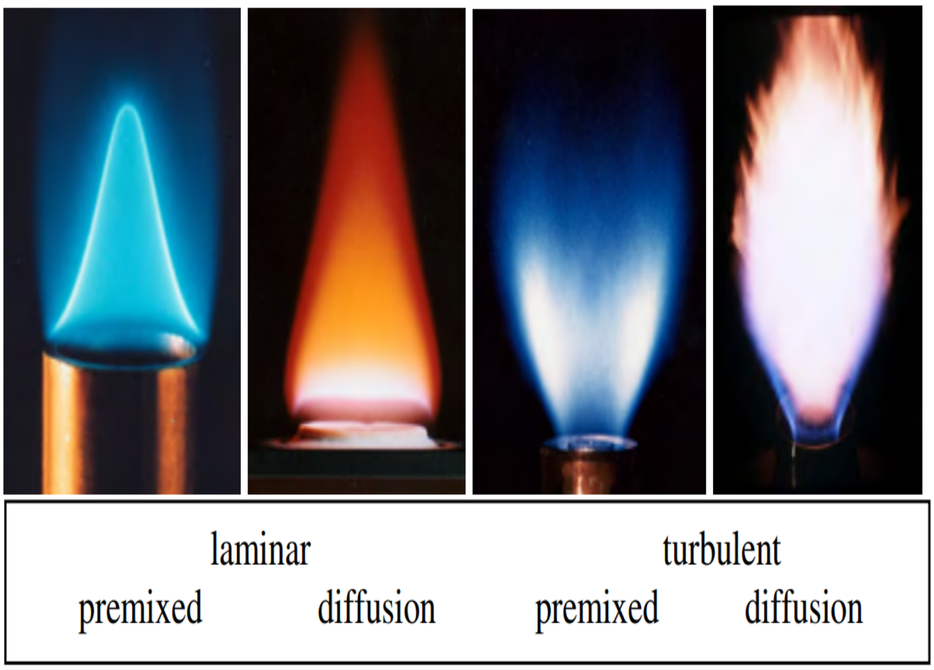

Figure 1.5: Flame types under laminar and turbulent flow [8].

There are two types of flames which are premixed and nonpremixed flames [48]. A premixed flame is produced when a fuel is mixed with an oxidizer, oxygen for instance, in the air before ignition. However, when the oxidizer combines with the fuel by diffusion, the flame is called nonpremixed flame, figure 1.5. Usually, during combustion, the flame propagation proceeds in a thin layer between burned and unburned substance. This layer is known as the flame front propagation.

1.2.5 Solidification

Solidification is a phase transition in which a liquid turns into a solid when its temperature is lowered to its freezing point. During the solidification, a front propagation is observed in many cases. One example is when a pure fluid is introduced in a container with walls that are held at a temperature less than the melting temperature [43]. Then the heat will extract through the sides of the container. In this case, the liquid is initially at a temperature greater than melting temperature, then the solidification process begins and the solid starts to form at the walls. This solidification can be considered as a solidification front propagation. The solidification front is stable and moves toward the centre of the container, figure 1.6(a). This case is more likely to be used in industrial applications, for example in the metal casting which is usually used for making complex shapes that would be difficult or expensive to make by different methods. In the second case, when a seed crystal is introduced in a vessel which contains supercooled liquid, the interface at the seed grows and generates crystals of dendritic shape [58]. In addition, at the tip of a primary dendrite, secondary dendrites are formed which grow on the sides. In this case, the front is unstable, figure 1.6(b).

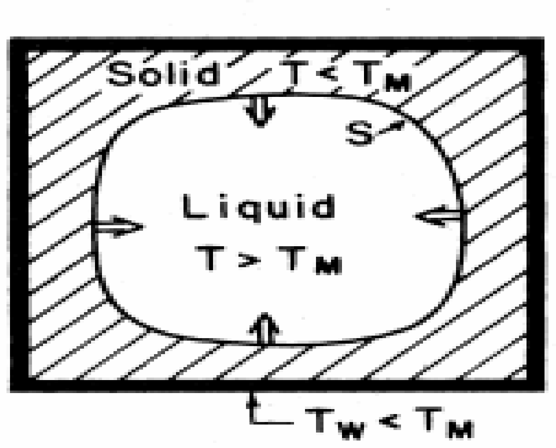

(a) Stable front [43]

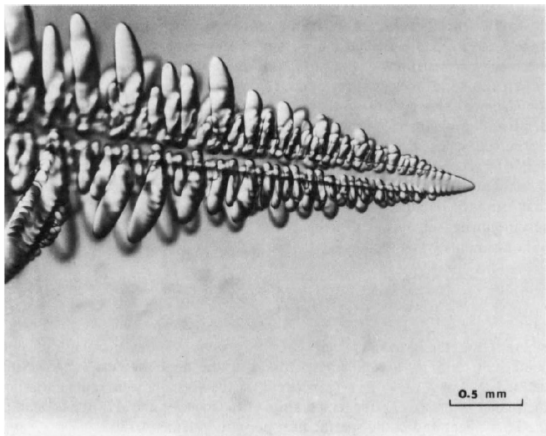

(b) Unstable front [58]

Figure 1.6: Schematic illustration of solidification.

1.3 History of front propagation

The front propagation field started essentially in 1937 with the work of Fisher [23] and Kolmogorov et al. [37] on a nonlinear diffusion equation (we will explain it in more details in section 1.4). They characterized the spread of an advantageous gene in the context of population dynamics. Furthermore, the existence of a travelling wavefront was proved. In 1951, Skellam [70] used the diffusion equation to introduce a mathematical model for biological invasion. He studied the spread of Muskrats in Central Europe. In 1959, front propagation appeared in the context of gravity currents in the natural environments, such as between salt and freshwater in the rivers [15]. In 1977, Sivashinsky [67] introduced a model for instability of laminar flame fronts. The nonlinear growth of a disturbed plane flame front in a hydrodynamic instability regime caused by thermal expansion of the burnt gas was studied by Michelson and Sivashinsky [51]. In the early 1980s, physicists started to work with problems in crystal growth, dendritic solidification and pattern selec-

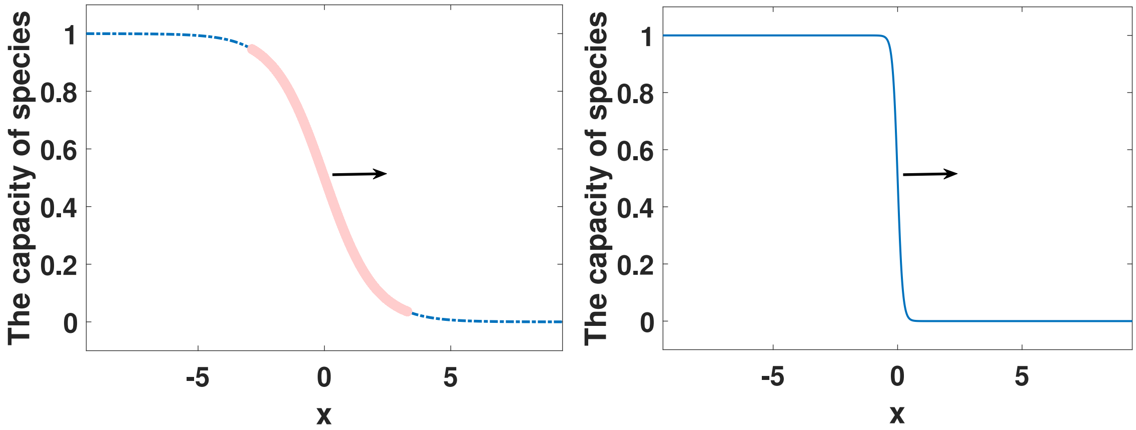

(a) Smooth front.

(b) Sharp front.

Figure 1.7: Wavefront propagation shapes.

tion propagation mainly by Langer and his coworkers [6, 19, 42, 43]. Thual [73] illustrated numerically that the Michelson Sivashinsky equation has stable steady solutions with the poles aligned parallel to the imaginary axis in the context of the dynamics of wrinkled flame fronts. Turbulent premixed flames for mixtures of methane-air in a high-pressure were examined experimentally [36, 71]. Experimentally, the buoyancy-driven instability of an autocatalytic reaction front was studied by Böckmann and Müller [9]. They showed that the unstable density stratification at an ascending front leads to convection that results in a finger-like front deformation. De Wit [18] exhibited the influence of chemical reaction on the dynamics of the fingering instability in porous media. Front propagation also appeared in spread of epidemics [54, 55] and snow avalanches [56, 59].

Mathematical models for wavefronts have been studied by scientists since the 1930s [23, 37]. Their models are formulated in terms of the concentration of substances. For convenience, if we return to our previous example of the muskrat, ignoring one spatial dimension for simplicity, then we get a density of population function against a direction of diffusion. In other words, we restrict attention to one spatial dimension by taking a cross-section of one of the contours from the centre towards the spread direction in figure 1.2(a). Thus, we get a smooth function describing the density of population in one spatial dimension x, figure 1.7(a). So the edge from the maximum to the minimum point of the curve, described as the solid line in figure 1.7(a), is called a wavefront.

However, sometimes a wavefront can be a sharper wavefront more like a step function, figure 1.7(b). This means the density or the concentration of the substance is nearly maximum or minimum. In our combustion example, if a flame front is considered as a geometrical surface of zero thickness, then it is easy to choose a coordinate system moving with the flame front, so the boundary between burnt and unburnt land is considered as a flame front propagation, figure 1.4.

1.4 Reaction-diffusion systems

The reaction-diffusion is one of the most significant classes of partial differential equations. During the past few decades, the reaction-diffusion system has received much attention in many areas of the sciences. The system has been used to describe dynamical processes in various science areas in nature such as chemistry, ecology, biology and physics (see for example [3, 11, 22, 49, 74]). The reaction-diffusion system is a combination of logistic and diffusion (heat) equations. Thus it has been used for modelling many natural phenomena. In ecology, this system is used to understand the interactions of organisms with each other and with the environment [12]. In addition, it is used to describe the spatiotemporal dynamics of the population where the density of species is known. An example was given in section 1.2.2, where the non-native species attempts to establish itself in the new environment or invade the area. Similarly, this system is modelled to describe the biological phenomena such as the spread of disease. The simplest reaction-diffusion equation in one dimension can be represented in the general form

$$\frac{\partial w}{\partial t} = D\frac{\partial^2 w}{\partial y^2} + f(w), \tag{1.4.1}$$

where D is the constant diffusion coefficient, $\frac{\partial^2 w}{\partial y^2}$ represents the diffusion term, $f(w)$ is the reaction term, w is the concentration or density of a substance and y is the direction of the front propagation. One of the simplest examples of a nonlinear reaction-diffusion system is the Fisher-KPP equation model.

Fisher [23] and Kolmogorov et al. [37] in 1937 determined this equation in their papers in the context of population dynamics to characterize the spread of an advantageous gene. The nondimensional Fisher-KPP equation can be written as

$$\frac{\partial w}{\partial t} = \frac{\partial^2 w}{\partial y^2} + w(1-w). \tag{1.4.2}$$

There are two steady state solutions of this equation, $(w = 1)$ and $(w = 0)$ which are respectively stable and unstable [55]. In addition, Kolmogorov et al. [37] demonstrated the existence of a travelling wave solution of Fisher-KPP equation for every wave speed $c \geq 2$. A travelling wave is a wave that travels at a constant speed without changing in the shape. Mathematically the form of a travelling wave solution is $w(y,t) = W(y - ct)$, where c is the speed of the wave. By assuming that $z = y - ct$, equation (1.4.2) can be written as an ordinary differential equation

$$\frac{d^2 W}{dz^2} + c\frac{dW}{dz} + W(1-W) = 0, \tag{1.4.3}$$

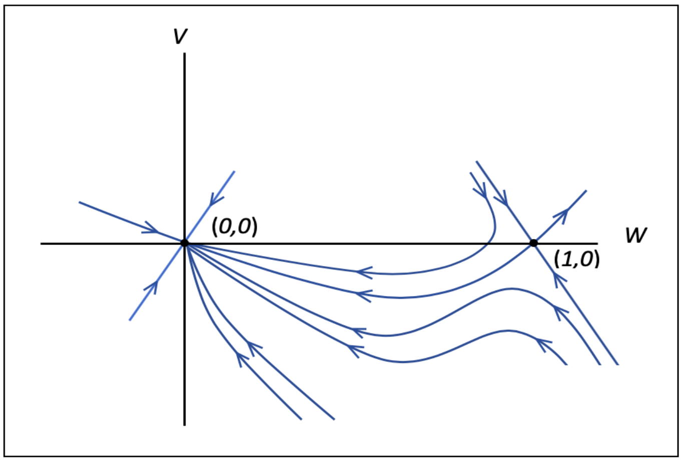

Figure 1.8: Phase plane trajectories for the Fisher-KPP equation (1.4.2) for the travelling wave solution when $c \geq 2$.

which can be solved subject to conditions

$$\lim_{z \to \infty} W(z) = 0, \qquad \lim_{z \to -\infty} W(z) = 1.$$

The equation (1.4.3) can be studied by converting it to a system of first order ordinary differential equations using $W^{'} = V$. We get

$$\begin{aligned} W^{'} &= V \\ V^{'} &= -cV - W(1 - W). \end{aligned}$$

This system gives two equilibrium points $(0, 0)$ and $(1, 0)$. The Jacobi matrix of the system is

$$J = \begin{bmatrix} 0 & 1 \\ 2W - 1 & -c \end{bmatrix}.$$

Therefore when $c \geq 2$, the equilibrium point $(0, 0)$ has two negative eigenvalues so it is stable node, and $(1, 0)$ has a positive and a negative eigenvalue so it is saddle point, figure 1.8.

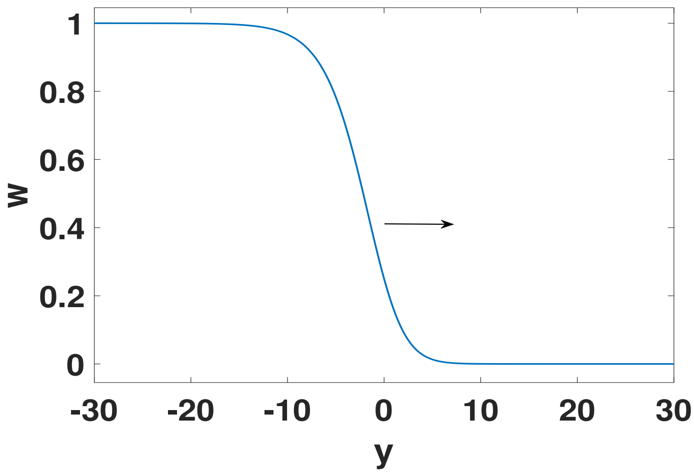

Figure 1.9: Travelling wavefront solution of the Fisher-KPP equation (1.4.2) when the wavefront speed $c = \frac{5}{\sqrt{6}} \approx 2.0412$.

One analytical solution of the Fisher-KPP equation (1.4.2), which is shown in figure 1.9, for a particular choice of $c = \frac{5}{\sqrt{6}} \approx 2.0412$ was found in [1],

$$w(y,t) = W(z) = \frac{1}{[1+\exp(z/\sqrt{6})]^2}. \tag{1.4.4}$$

1.5 Kuramoto-Sivashinsky equation

The Kuramoto-Sivashinsky (KS) equation is a simple partial differential equation that describes complex properties in both time and space. The KS equation arises as a model for transitions between steady planar fronts, curved fronts and complex spatiotemporal behaviour as a propagation of fronts. This equation has been studied by a great variety of researchers because it has a wealth of nontrivial dynamical behaviour. In 1976, Kuramoto and Tsuzuki [39] derived it to model wave propagation in reaction-diffusion chemical systems. In 1977, Sivashinsky [67] introduced it as a model for instability of laminar flame fronts. Furthermore, it has been studied as a model for a variety of applications such as falling-film flows [64, 68], chemical fronts [38], combustion fronts [66], phase turbulence [65] and interfacial instabilities in directional solidification [57]. The KS equation in one dimensional space can be written in integral form as

$$\frac{\partial u(x,t)}{\partial t} = -\frac{1}{2}\left(\frac{\partial u(x,t)}{\partial x}\right)^2 - \frac{\partial^2 u(x,t)}{\partial x^2} - \frac{\partial^4 u(x,t)}{\partial x^4}, \tag{1.5.1}$$

or in derivative form, where $v = u_x$, as

$$\frac{\partial v(x,t)}{\partial t} = -v\left(\frac{\partial v(x,t)}{\partial x}\right) - \frac{\partial^2 v(x,t)}{\partial x^2} - \frac{\partial^4 v(x,t)}{\partial x^4}, \tag{1.5.2}$$

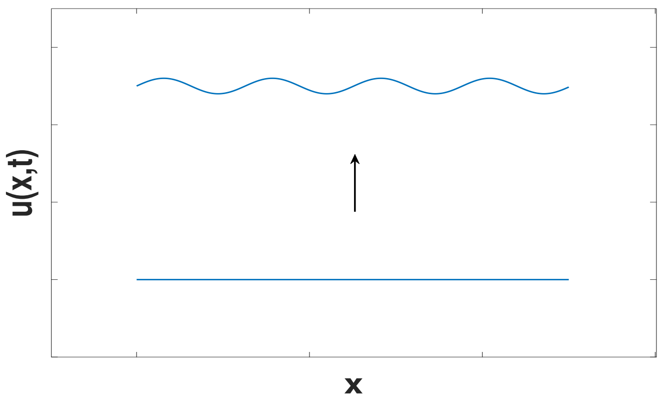

Figure 1.10: Front propagation of unstable states.

where $u(x,t)$ is the location of the front or the direction of travelling and x-axis is directed along the front, figure 1.10. The KS equation (1.5.1) includes a fourth-order dissipation term and a negative second-order term which acts to destabilize the solution of the KS equation.

We can see that $u = H_0$ is a solution of the KS equation for any constant H_0 representing a flat front. Thus, the stability of a solution of this equation can be tested by adding a small perturbation to the front under consideration. If the perturbation decays then the front is stable, but if it grows then the front is unstable.

The dispersion relation (the relation between growth rate λ and wavenumber k) can be determined to analyse the stability of the flat-front solution, by introducing small perturbations to the stationary state solution, $u = H_0$. This gives $H(x,t) = H_0 + \delta H_1(x,t)$, where $0 < \delta \ll 1$. By substituting $H(x,t)$ into (1.5.1) and linearising it, we get $(H_1)_t = -(H_1)_{xx} - (H_1)_{xxxx}$. Now, we seek a solution in the form $H_1(x,t) = e^{\lambda t}e^{ikx}$, where λ is growth rate and k is the wavenumber, then the dispersion relation is

$$\lambda = k^2 - k^4. \tag{1.5.3}$$

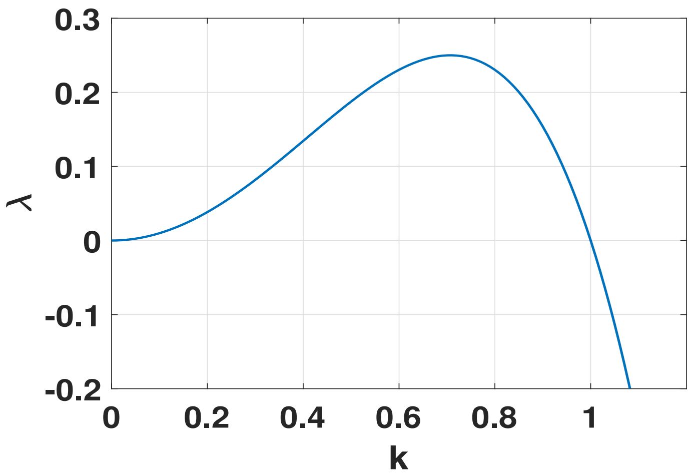

Figure 1.11: Dispersion relation of KS equation (1.5.3).

We can notice that at small wavenumbers the k^2 term dominates the term k^4 and leading to the positive growth rate (unstable). As the wavenumber increases the term k^4 becomes stronger and leads to a negative growth rate (stable). It can be recognized from figure 1.11 that the flat front solution of the KS equation is unstable when the wavenumber $0 \le k < 1$, and stable otherwise.

In the nonlinear regime, the KS equation cannot be solved analytically. Thus, the KS equation is solved numerically. The behaviour of solutions of the KS equation

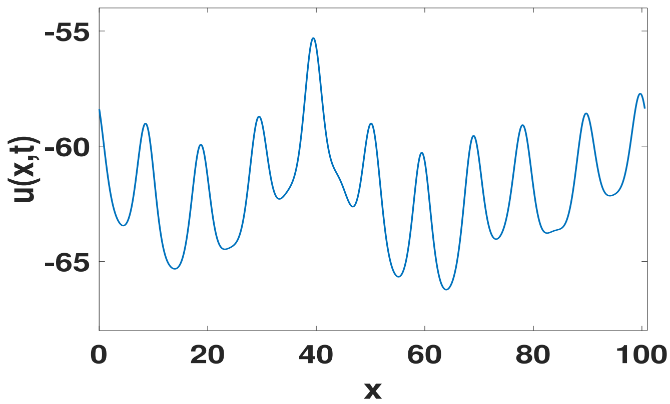

Figure 1.12: The chaotic solution of the KS equation when $t = 120$.

is complex and interesting because it acts as a chaotic dynamics. In the past few decades, the KS equation has been solved numerically by many methods [2, 33, 40, 47, 53, 75]. An example solution of the KS equation at a certain time, using a small initial condition $u(x, 0) = 10^{-6}r$ where r is a vector containing random values between 0 and 1, is shown in figure 1.12. The KS equation describes the problems that have growth rate proportional to k^2 for small k as is shown in the dispersion relation. In the present study, we are interested in the problems, such as those discussed in the following section, that have growth rate proportional to $|k|$ or k for small wavenumber. This kind of problem is described by nonlocal-KS equations.

1.6 Systems with $O(k)$ growth rate

The dispersion relation curve of the KS equation, figure 1.11, in the unstable region seems to have a parabolic appearance for small wavenumber and the growth rate λ=$O(k^2)$ as $k \to 0$. In this section, we look further insight into how the growth rate depends on the order of k for small k, or how to include the term of $O(k)$ in the dispersion relation.

As we have symmetric front, the KS equation or any PDEs that we have to describe this front must have the growth rate proportional to even powers of k. So the growth rate that is proportional to k for small k cannot be described by any PDEs. One way to include $O(k)$ terms in the dispersion relation which give us the growth rate proportional to $|k|$ for small k is to include the nonlocal term in the system that describes our front. This will be the main focus in the thesis as we will see in the next section.

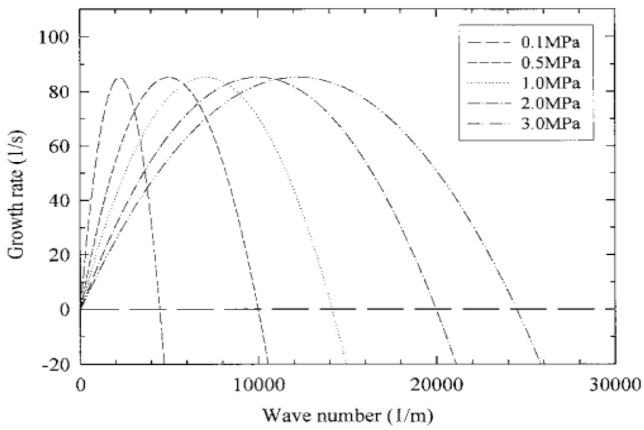

Figure 1.13: Effects of elevated pressure on flame front instability [36].

A great deal of experimental work has been done in the past to explore the speed, dynamics of front and front instability of the problems that have the growth rate proportion to k for small k. These problems are different from that has growth rate proportional to k^2 for small k such as the KS equation. For instance, turbulent premixed flames for mixtures of methane-air in a high-pressure was examined experimentally [36, 71]. It was shown that, when flame front instability theory was applied to flames in high-pressure environments, the area of the wavenumbers where the flame front is unstable increases to larger wavenumbers with increasing pressure and the growth rate is proportional to k for small k, figure 1.13. This is due to the effect of the thermal diffusivity decreasing with increasing pressure. Consequently, as pressure is increased the dynamics of the flame front becomes more unstable and strongly wrinkled.

Experimentally the growth rate of the buoyancy-driven instability of an autocatalytic front was determined by Böckmann and Müller [9]. They compare the experimental dispersion relation with theory and show that the experimental growth rate is proportional to k for small k and agrees with theoretical study, figure 1.14. They also indicate that the stability is found at large wavenumber while the system is unstable at small wavenumber. The figure shows that the growth rate is proportional to wavenumber for small wavenumber.

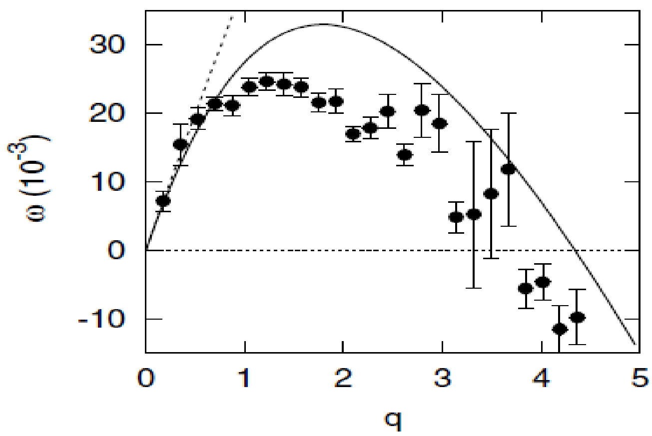

Figure 1.14: Comparison of the dimensionless measured growth rates with a 2D-Navier-Stokes model (solid trace) and a Hele-Shaw flow model (dotted trace), [9].

Khain and Sander [35] formed a simple reaction-diffusion model that captured the behaviour of the malignant brain tumor growth dynamics. They show that when the ratio of the nutrient and cell diffusion coefficients exceeds some certain value then the flat front becomes unstable. Thus the plane propagating front is unstable for small wavenumber, while the cell diffusion in the transverse direction stabilises the instability for larger wavenumber. The authors determined the dispersion relation (see figure 3 in the same paper), which shows that the growth rate is proportional to k as k tends to 0.

The stability of the chemical reaction in a vertical Hele-Shaw cell was examined theoretically and the instability for two fronts, the up-going and down going in the same time, was studied by Kalliadasis et al. [34]. The authors showed that the unstable wavenumber for the up going front is usually smaller than that for the downgoing front. This leads to the wavelength of the dynamics for the up going front is larger than that for the downgoing front. They have also noticed that the up going front will be unstable before the downgoing front and show fingering because the growth rate for it is larger than that for the downgoing front. Furthermore, they examined the growth rate of both up going and down going fronts $\lambda \propto k$ as $k \ll 1$.

Härtel et al. [31] analysed the linear stability of the flow at the head of two-dimensional gravity-current front numerically. Results are presented that the range of the unstable wavenumbers increases with increasing Grashof number. In addition, this analysis was done to explain that the instability dynamics leads to the formation of the lobe-and-cleft pattern. They also realized that the growth rate is proportional to k for small wavenumber.

1.7 Thesis aims and objectives

The aim of this work is to investigate, introduce, solve and discuss alternative models for front instabilities that fit better with the shapes of fronts observed in applications than Kuramoto-Sivashinsky equation, precisely we deal with systems which have the growth rate proportional to k or $|k|$ for small wavenumber k where the front dynamics takes different shapes such as lobe-and-cleft patterns. In particular, we will consider models that incorporate nonlocal effects, which cannot be written as partial differential equations.

A nonlocal effect has important role in many systems, for example in population dynamics [7, 10], and current instability systems [20]. A nonlocality appears when the system is affected by external influence and can be expressed by an integral term, then the partial differential equation is replaced by an integrodifferential equation.

In this work, we deal with three nonlocal equations which are nonlocal Kuramoto-Sivashinsky, Michelson-Sivashinsky and modified Michelson-Sivashinsky. In 1977, Sivashinsky has developed Kuramoto-Sivashinsky equation in the context of flame propagation when he derived a nonlinear time-dependent equation for the flame front position $u(x,t)$, referred as the nonlocal-KS equation, which includes the integral term and can be written in general form as

$$\frac{\partial u(x,t)}{\partial t} = a\int_{-\infty}^{\infty} \frac{\frac{\partial u(x^*,t)}{\partial x^*}}{x-x^*}dx^* - b\frac{1}{2}\left(\frac{\partial u(x,t)}{\partial x}\right)^2 - c\frac{\partial^2 u(x,t)}{\partial x^2} - d\frac{\partial^4 u(x,t)}{\partial x^4}, \quad (1.7.1)$$

where the integral term represents the Darrieus-Landau hydrodynamic instability [17, 41]. If the integral term is not present ($a = 0$), then the equation is the Kuramoto-Sivashinsky equation. The Michelson-Sivashinsky [50], is referred as the

MS equation, can be written as

$$\frac{\partial u(x,t)}{\partial t} = a\int_{-\infty}^{\infty} \frac{\frac{\partial u(x^*,t)}{\partial x^*}}{x-x^*}dx^* - b\frac{1}{2}\Big(\frac{\partial u(x,t)}{\partial x}\Big)^2 + c\frac{\partial^2 u(x,t)}{\partial x^2}, \tag{1.7.2}$$

We modified the MS equation by changing the integral term, which referred as the modified Michelson-Sivashinsky equation (MMS), and can be written as

$$\frac{\partial u(x,t)}{\partial t} = a\int_{-\infty}^{\infty} \frac{(x-x^*)}{L^2+(x-x^*)^2}\frac{\partial u(x^*,t)}{\partial x^*}dx^* - b\frac{1}{2}\Big(\frac{\partial u(x,t)}{\partial x}\Big)^2 + c\frac{\partial^2 u(x,t)}{\partial x^2} \tag{1.7.3}$$

In our work, it is important to know how the MS equation arises as a model for instability of front dynamics in order to understand the limitations and exceptions for deriving better models. This is what we will do in the next section.

1.8 Discussion of Michelson-Sivashinsky equation

We illustrate how the Michelson-Sivashinsky (MS) equation may arise as a model for instability of front dynamics. In the hydrodynamics theory of front propagation, such as flame front propagation, the diffusion length which is described as the front thickness is very small while comparing it to the domain size L.

Assume that a travelling planar front, in a homogeneous and isotropic medium, is appearing from a system of reaction-diffusion or a combustion problem. In addition, suppose that the location of the front under small perturbation is $y = u(x,t) + st$, where s is the speed of travelling front, y is the direction of travelling and x-axis is directed along the front. So the front is no longer planar and its position depends on the transverse coordinate x, figure 1.10.

The evolution equation for u must not depend on the value of u, it can depend on the derivative of u according to x because of translational invariance. As the evolution equation of u is symmetrical in x, then it depends on the even derivatives of u.

Furthermore, when the problem has the growth rate $\lambda = O(k)$, that we mentioned in section 1.6, the reflection symmetry in x means that the only allowable terms in dispersion relation involve ($|k|$, k^2, $|k|^3$, k^4, ...). It is clear from linearising the MS equation that the terms $\frac{\partial^2 u(x,t)}{\partial x^2}$, $\frac{\partial^4 u(x,t)}{\partial x^4}$, $\frac{\partial^6 u(x,t)}{\partial x^6}$, ... give k^2, k^4, k^6, ... respectively, and from solving the integral term, the nonlocal term gives the term $|k|$, (mathematically will be described in more details in section 2.3). Therefore the linearised equation should have the following form

$$\frac{\partial u(x,t)}{\partial t} = c_1 \int_{-\infty}^{\infty} w(x-x^*)\frac{\partial u(x^*,t)}{\partial x^*}dx^* + c_2\frac{\partial^2 u(x,t)}{\partial x^2} + c_4\frac{\partial^4 u(x,t)}{\partial x^4} + c_6\frac{\partial^6 u(x,t)}{\partial x^6} + ...,$$

where c_is are constants and the function $w(x - x^*)$ that appears in the nonlocal term is known as the kernel. The simplest corresponding dispersion relation is

$$\lambda = |k| - k^2,$$

The value of u will get very large when time goes infinity because of the exponential growth, so a nonlinear term should be present in the equation to limit the growth of the instability. Due to the weakly nonlinear theory, the simplest suitable nonlinear term to add in the equation is quadratic one. As we mentioned in the same case as the linear term, the term u is not allowed to appear. Thus the quadratic of u derivatives according to x might appear in the equation, which are one of these terms $((\partial u/\partial x)^2, (\partial^2 u/\partial x^2)^2, (\partial^3 u/\partial x^3)^2, ...)$. In our case the smallest derivative $(\partial u(x,t)/\partial x)^2/2$ is taken. Thus the MS equation can be written as follows

$$\frac{\partial u(x,t)}{\partial t} = \int_{-\infty}^{\infty} \frac{\frac{\partial u(x^*,t)}{\partial x^*}}{x - x^*}dx^* - \frac{1}{2}\left(\frac{\partial u(x,t)}{\partial x}\right)^2 + \frac{\partial^2 u(x,t)}{\partial x^2}, \tag{1.8.1}$$

The MS equation has been derived physically in details by Fogla [24]. Note that the

MS equation has different behaviour from the KS equation. In the next section, we indicate some works that have done on the MS equation.

1.9 Previous work on MS equation

In 1977 Sivashinsky derived the nonlinear integrodifferential equation for instability of the laminar flat flame front, which may represent as a basis for derivation of equations for a flame front [67], we have referred it as nonlocal-KS equation (1.7.1). In the same year, Michelson and Sivashinsky derived the MS equation (1.8.1) in the context of the evaluation of a disturbed plane flame front [50]. They also solved the KS equation and the MS equation numerically by the finite-difference method to describe the dynamics of the flame front.

In the case of the KS equation, the authors found that even if the characteristic dimension of the initial disturbance is larger than the wavelength that is corresponding to the maximum growth rate, the flame front after a short time of the initial displays a quasi-periodic chaos structure. In addition, they demonstrated that the flame front moves constantly toward the negative direction of y where $y = u(x, t)$, figure 1.10. Furthermore, they confirmed that the flame front settles into a steady state but non-stationary shape.

Michelson and Sivashinsky further reported that their study of MS equation shows that the evaluation of the front dynamics is different from that adopted for the KS equation while it started with the same initial disturbance. The dynamics of the flame front, when the Lewis number equal 1 (in the case of long-wave asymptotic behaviour), settles into a steady and stationary propagation regime. They also showed that the shape of the steady stationary dynamics takes the form of parabola like arcs and convex towards the negative direction of y where $y = u(x, t)$, figure 1.10.

The nonlinear development of hydrodynamic unstable propagating flames was investigated numerically based on the MS equation by Rastigejev and Matalon [60]. The MS equation in their case includes the Markstein number which is placed in front of the second derivative term. They show that, when Markstein number is 0.005, the small disturbances forming from initial data merge and shape up larger cells which eventually coalesce into a steady state with a single-peak structure. Also it is shown in their research that, when the Markstein number equal 0.002, like previous case the small disturbances on the flame front that generate from initial stage merge forming bigger cells which finally form a single-peak structure, but the system never settles into a steady state because continuously the small wrinkles are appearing on the flame front and merging again.

In 2007 Matalon illustrated the numerical solution of the MS equation on the context of the premixed combustion [48]. He emphasized that the short wavelength wrinkles, that introduced through initial disturbances of the evaluation structure of the flame front, merge when there is a parameter in front of the second derivative term which is the Markstein number and it is not too small. Finally, the structure of the flame front translates into a single-peak that propagates at a constant speed, which means the dynamics of the front settle into a steady state stationary shape.

Chapter 2

Numerical solutions of nonlocal front equations

2.1 Introduction

This chapter is concerned with presenting numerical simulations of all three nonlocal-KS (1.7.1), MS (1.7.2)and MMS (1.7.3) systems in one dimension. Before embarking on the numerical solution, however, it is necessary to nondimensionalize all three equations. In addition, we find the dispersion relation of all three equations to investigate the linear stability of them. Thus we start the chapter with the scaling of all three nonlocal equations, section 2.2. Then we find the dispersion relation of them, section 2.3. In section 2.4, by finding the numerical solution we analyze the behaviour of the front propagation based on all three nonlocal equations. The speed of the front is also calculated in this section. We summarise our main results for this chapter in the section 2.5.

2.2 The scaling of nonlocal front equations

Nondimensionalization is a simple important technique that helps simplify differential equations by reducing the number of parameters and rescaling variables. In this section, we nondimensionalize all three nonlocal equations (1.7.1),(1.7.2) and (1.7.3).

2.2.1 Nonlocal-KS equation

The nonlocal-KS equation (1.7.1), is

$$\frac{\partial u(x,t)}{\partial t} = a\int_{-\infty}^{\infty}\frac{\frac{\partial u(x^*,t)}{\partial x^*}}{x-x^*}dx^* - \frac{1}{2}b\left(\frac{\partial u(x,t)}{\partial x}\right)^2 - c\frac{\partial^2 u(x,t)}{\partial x^2} - d\frac{\partial^4 u(u,t)}{\partial x^4}, \quad (2.2.1)$$

where the parameters a, c and d have units of $\frac{length}{time}$, $\frac{length^2}{time}$ and $\frac{length^4}{time}$ respectively. There are two independent variables t and x and one dependent variable u in the equation. To make the equation (2.2.1) dimensionless, we set

$$x = \alpha X, \quad t = \beta T, \quad u = \gamma U, \tag{2.2.2}$$

where α, β and γ are characteristic values of x, t and u respectively. Then we substitute those new dimensionless variables in equation (2.2.1), so the equation becomes

$$\frac{\partial U(X,T)}{\partial T} = a\frac{\beta}{\alpha}\int_{-\infty}^{\infty}\frac{\frac{\partial U(X^*,T)}{\partial X^*}}{X-X^*}dX^* - \frac{1}{2}\frac{\gamma\beta}{\alpha^2}b\Big(\frac{\partial U(X,T)}{\partial X}\Big)^2 - c\frac{\beta}{\alpha^2}\frac{\partial^2 U(X,T)}{\partial X^2} - d\frac{\beta}{\alpha^4}\frac{\partial^4 U(X,T)}{\partial X^4}. \tag{2.2.3}$$

The equation (2.2.3) still has dimensional terms. To make it free of units and set some coefficients equal 1, we choose

$$\gamma = \frac{c}{b}, \quad \alpha = \sqrt{\frac{d}{c}}, \quad \beta = \frac{d}{c^2},$$

we assume that $\frac{d}{c} > 0$ and $b, c \neq 0$ in the original system. As a result, the scaled nonlocal-KS equation becomes

$$\frac{\partial U(X,T)}{\partial T} = \frac{a}{c}\sqrt{\frac{d}{c}}\int_{-\infty}^{\infty}\frac{\frac{\partial U(X^*,T)}{\partial X^*}}{X-X^*}dX^* - \frac{1}{2}\Big(\frac{\partial U(X,T)}{\partial X}\Big)^2 - \frac{\partial^2 U(X,T)}{\partial X^2} - \frac{\partial^4 U(X,T)}{\partial X^4}. \tag{2.2.4}$$

Due to the fact that the number of parameters is four and the number of variables is three in equation (2.2.1), one nondimensional parameter remains in the equation. We can put the remaining parameter in front of any term but we put it in front of the nonlocal term to evaluate the effect of it on the system and define it to be ϵ, then

$$\frac{\partial U(X,T)}{\partial T} = \epsilon\int_{-\infty}^{\infty}\frac{\frac{\partial U(X^*,T)}{\partial X^*}}{X-X^*}dX^* - \frac{1}{2}\Big(\frac{\partial U(X,T)}{\partial X}\Big)^2 - \frac{\partial^2 U(X,T)}{\partial X^2} - \frac{\partial^4 U(X,T)}{\partial X^4}. \tag{2.2.5}$$

2.2.2 The Michelson-Sivashinsky (MS) equation

The Michelson-Sivashinsky equation (1.7.2) is

$$\frac{\partial u(x,t)}{\partial t} = a\int_{-\infty}^{\infty}\frac{\frac{\partial u(x^*,t)}{\partial x^*}}{x-x^*}dx^* - \frac{1}{2}b\Big(\frac{\partial u(x,t)}{\partial x}\Big)^2 + c\frac{\partial^2 u(x,t)}{\partial x^2}. \quad (2.2.6)$$

Since the number of parameters and variables are equal, we can obtain a scaled equation free of units and set all coefficients equal to 1. Again the parameters a and c have the same units that we mentioned above (section 2.2.1). To make the equation (2.2.6) free of units, we substitute x, t and u from (2.2.2) into (2.2.6) to give

$$\frac{\partial U(X,T)}{\partial T} = a\frac{\beta}{\alpha}\int_{-\infty}^{\infty}\frac{\frac{\partial U(X^*,T)}{\partial X^*}}{X-X^*}dX^* - \frac{1}{2}\frac{\gamma\beta}{\alpha^2}b\Big(\frac{\partial U(X,T)}{\partial X}\Big)^2 + c\frac{\beta}{\alpha^2}\frac{\partial^2 U(X,T)}{\partial X^2}. \quad (2.2.7)$$

To make (2.2.7) dimensionless and free of coefficients, we choose

$$\gamma = \frac{c}{b}, \quad \alpha = \frac{c}{a}, \quad \beta = \frac{c}{a^2},$$

where $a, b \neq 0$, then the scaled MS equation becomes

$$\frac{\partial U(X,T)}{\partial T} = \int_{-\infty}^{\infty}\frac{\frac{\partial U(X^*,T)}{\partial X^*}}{X-X^*}dX^* - \frac{1}{2}\Big(\frac{\partial U(X,T)}{\partial X}\Big)^2 + \frac{\partial^2 U(X,T)}{\partial X^2}. \quad (2.2.8)$$

2.2.3 The Modified Michelson-Sivashinsky (MMS) equation

The Modified Michelson-Sivashinsky equation (1.7.3) can be written as

$$\frac{\partial u(x,t)}{\partial t} = a\int_{-\infty}^{\infty}\frac{(x-x^*)}{L^2+(x-x^*)^2}\frac{\partial u(x^*,t)}{\partial x^*}dx^* - \frac{1}{2}b\Big(\frac{\partial u(x,t)}{\partial x}\Big)^2 + c\frac{\partial^2 u(x,t)}{\partial x^2} \quad (2.2.9)$$

We rescale the MMS equation (2.2.9), where the parameters a and c have the same units as the above models (sections 2.2.1 and 2.2.2) and L has the unit of *length*. To make the equation (2.2.9) dimensionless, we use the re-scaling (2.2.2) and substitute in (2.2.9) which leads to

$$\frac{\partial U(X,T)}{\partial T} = a\frac{\beta}{\alpha}\int_{-\infty}^{\infty}\frac{(X-X^*)}{\frac{L^2}{\alpha^2}+(X-X^*)^2}\frac{\partial U(X^*,T)}{\partial X^*}dX^* - \frac{1}{2}\frac{\gamma\beta}{\alpha^2}b\Big(\frac{\partial U(X,T)}{\partial X}\Big)^2 + c\frac{\beta}{\alpha^2}\frac{\partial^2 U(X,T)}{\partial X^2}. \quad (2.2.10)$$

Similarly, to make it dimensionless and set some coefficients equal to 1, we choose

$$\alpha = L, \quad \gamma = \frac{c}{b}, \quad \beta = \frac{L^2}{c},$$

where $b, c \neq 0$. Then the scaled MMS equation becomes

$$\frac{\partial U(X,T)}{\partial T} = \frac{aL}{c}\int_{-\infty}^{\infty}\frac{(X-X^*)}{1+(X-X^*)^2}\frac{\partial U(X^*,T)}{\partial X^*}dX^* - \frac{1}{2}\Big(\frac{\partial U(X,T)}{\partial X}\Big)^2 + \frac{\partial^2 U(X,T)}{\partial X^2}. \quad (2.2.11)$$

As for the nonlocal-KS equation, we get the scaled MMS equation with one nondimensional parameter

$$\frac{\partial U(X,T)}{\partial T} = \epsilon\int_{-\infty}^{\infty}\frac{(X-X^*)}{1+(X-X^*)^2}\frac{\partial U(X^*,T)}{\partial X^*}dX^* - \frac{1}{2}\Big(\frac{\partial U(X,T)}{\partial X}\Big)^2 + \frac{\partial^2 U(X,T)}{\partial X^2}. \quad (2.2.12)$$

2.3 Dispersion relation of nonlocal front equations

In this section, we study the effects of a nonlocal term on the linear stability of the nonlocal front equations. The linear stability of a flat front can be determined by studying the time evolution of a small perturbation of it. In this context, we present a theoretical determination of growth rates of the nonlocal front equations to find the linear stability analysis for the nonlocal-KS, MS and MMS systems. We rewrite the nonlocal-KS equation (2.2.5) as,

$$\frac{\partial u(x,t)}{\partial t} = \epsilon \int_{-\infty}^{\infty} \frac{\frac{\partial u(x^*,t)}{\partial x^*}}{x - x^*} dx^* - \frac{1}{2}\Big(\frac{\partial u(x,t)}{\partial x}\Big)^2 - \frac{\partial^2 u(x,t)}{\partial x^2} - \frac{\partial^4 u(x,t)}{\partial x^4}. \quad (2.3.1)$$

The flat front solution of the nonlocal-KS equation is $u(x,t) = u_0$ where u_0 is constant. We seek the stability analysis of (2.3.1) by setting a small perturbation to its stationary state solution u_0, to give

$$u(x,t) = u_0 + \delta u_1(x,t),$$

where $0 < \delta \ll 1$. Substituting this into (2.3.1) and linearizing it, gives

$$\frac{\partial u_1(x,t)}{\partial t} = \epsilon \int_{-\infty}^{\infty} \frac{\frac{\partial u_1(x^*,t)}{\partial x^*}}{x - x^*} dx^* - \frac{\partial^2 u_1(x,t)}{\partial x^2} - \frac{\partial^4 u_1(x,t)}{\partial x^4}. \quad (2.3.2)$$

If the perturbation is $u_1(x,t) = e^{\lambda t} e^{ikx}$, where λ is growth rate and k is the wavenumber, (2.3.2) becomes

$$\lambda = -\epsilon \int_{-\infty}^{\infty} \frac{ike^{ik(x^*-x)}}{x^* - x} dx^* + k^2 - k^4.$$

Since there is a singularity where $x = x^*$ in the above integral, we use the contour integral to evaluate it. The integral is

$$I = \int_{-\infty}^{\infty} \frac{ike^{ik(x^*-x)}}{x^* - x} dx^*.$$

I can be determined from the integral $\oint_C f(z)dz$, where C is a closed semi-circular contour in the complex plane, figure 2.1. By the Cauchy integral formula, when $k > 0$ we have

$$\oint_C \frac{ike^{ikz}}{z} dz = \int_{-R}^{R} \frac{ike^{ikz}}{z} dz + \int_{Arc} \frac{ike^{ikz}}{z} dz. \quad (2.3.3)$$

By Jordan's lemma, when $R \to \infty$ the integral $\int_{Arc} \frac{ike^{ikz}}{z} dz \to 0$. Then we use the residue theorem to find the integral $\oint_C \frac{ike^{ikz}}{z} dz$. The singularity is located on the

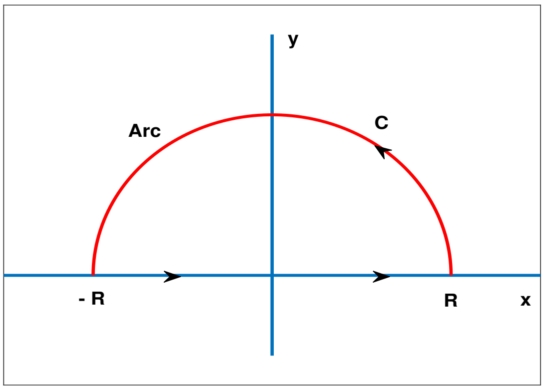

Figure 2.1: Close contour in the upper half-plane.

contour when $z = 0$, so by Cauchy principal value theorems we obtain

$$\oint_C \frac{ike^{ikz}}{z} dz = i\pi \times ik = -\pi k. \tag{2.3.4}$$

However when $k < 0$, we draw a lower half-plane semi circle close contour. Then by the same method that we have used to find (2.3.4), we obtain

$$\oint_C \frac{ike^{ikz}}{z} dz = -i\pi \times ik = \pi k. \tag{2.3.5}$$

So from (2.3.4) and (2.3.5) we have

$$\oint_C \frac{ike^{ikz}}{z} dz = -\pi |k|. \tag{2.3.6}$$

From (2.3.3), (2.3.6) and the Jordan's lemma when $R \to \infty$ we then have

$$I = \int_{-\infty}^{\infty} \frac{ike^{ik(x^* - x)}}{x^* - x} dx^* = -\pi |k|.$$

Thus the dispersion relation of the nonlocal-KS equation is

$$\lambda = -k^4 + k^2 + \epsilon\pi |k|. \tag{2.3.7}$$

Figure 2.2 shows the dispersion relation (2.3.7). The planar front is unstable to a band of wavenumbers for small k (long waves) and stable otherwise. Furthermore,

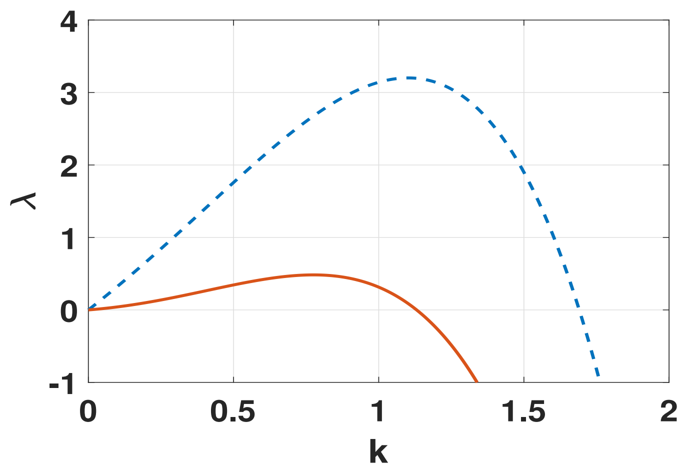

Figure 2.2: Curves illustrating the dispersion relation (2.3.7) for front instabilities for the nonlocal-KS equation (2.3.1): solid curve when $\epsilon = 0.1$ and dashed curve when $\epsilon = 1$.

when $\epsilon = 1$ the region of unstable wavenumber is larger than when $\epsilon = 0.1$ and the λ is bigger so the nonlocal term makes the instability grows faster.

Now, we rewrite the MS equation (2.2.8) as

$$\frac{\partial u(x,t)}{\partial t} = \int_{-\infty}^{\infty} \frac{\frac{\partial u(x^*,t)}{\partial x^*}}{x - x^*} dx^* - \frac{1}{2}\left(\frac{\partial u(x,t)}{\partial x}\right)^2 + \frac{\partial^2 u(x,t)}{\partial x^2}. \tag{2.3.8}$$

We use the similar method that was used above to find the dispersion relation (2.3.7), setting small perturbation ($u_1(x,t) = e^{\lambda t} e^{ikx}$) to stationary solution u_0 of (2.3.8) and linearising it leads to

$$\lambda = -\int_{-\infty}^{\infty} \frac{ike^{ik(x^*-x)}}{x^* - x} dx^* - k^2.$$

The integral term has been solved above by contour integration and gives $-\pi|k|$. Then the dispersion relation of (2.3.8) becomes

$$\lambda = -k^2 + \pi|k|. \tag{2.3.9}$$

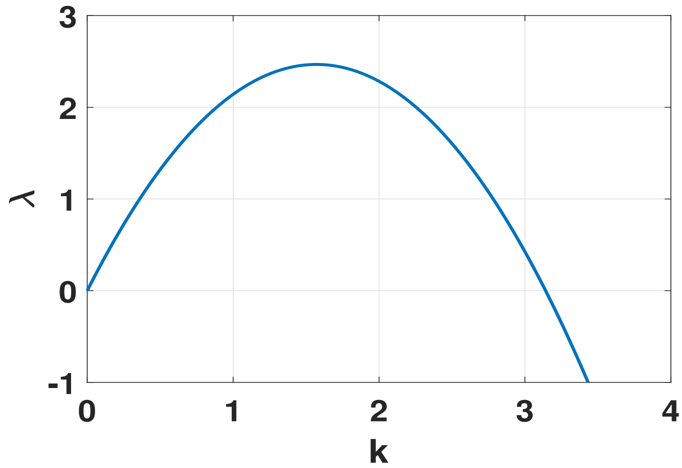

Figure 2.3: Curve illustrating the dispersion relation (2.3.9) for front instabilities for the MS equation (2.3.8).

The dispersion relation (2.3.9) illustrates that the growth rate is positive for small k and negative for large k, see figure 2.3. In this case, we can see that the maximum growth rate is $\frac{\pi}{2}$.

Finally we rewrite the MMS equation (2.2.12) as

$$\frac{\partial u(x,t)}{\partial t} = \epsilon \int_{-\infty}^{\infty} \frac{(x-x^*)}{1+(x-x^*)^2} \frac{\partial u(x^*,t)}{\partial x^*} dx^* - \frac{1}{2}\left(\frac{\partial u(x,t)}{\partial x}\right)^2 + \frac{\partial^2 u(x,t)}{\partial x^2} \quad (2.3.10)$$

The dispersion relation is found by the same way and the Cauchy integral formula is used to solve the integral because we have singularity when $x - x^* = i$ or $-i$. Then the dispersion relation of (2.3.10) can be written as follows

$$\lambda = -k^2 + \epsilon\pi|k|e^{-|k|}. \quad (2.3.11)$$

Figure 2.4 shows the dispersion relation (2.3.11). The growth rate is greater than zero for small k, while for larger k the diffusion term stabilizes the instability. Moreover, the area of wavenumber when the plane front is unstable increases to larger wavenumber with increasing ϵ.

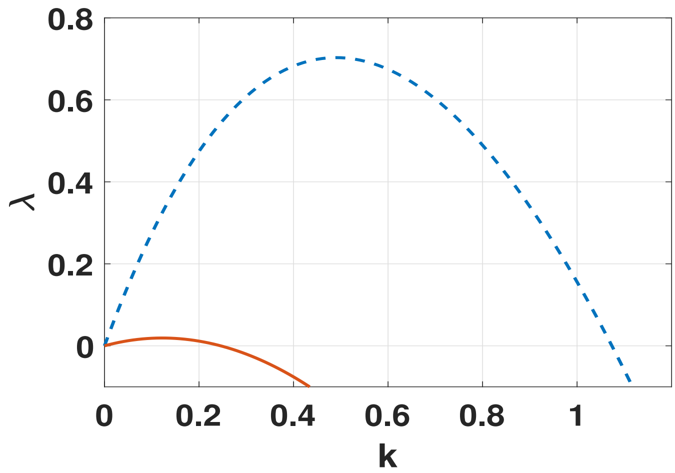

Figure 2.4: Curves illustrating the dispersion relation (2.3.11) for front instabilities for the MMS equation (2.3.10): solid curve when $\epsilon = 0.1$ and dashed curve when $\epsilon = 1$.

We can recognize that these dispersion relations are similar to some dispersion relations that have been found experimentally, for example they are similar to the dispersion relations we have mentioned in chapter 1, figure 1.13 .

2.4 Numerical study of nonlocal front models

2.4.1 Numerical method

We perform numerical simulations for three models (2.3.1), (2.3.8) and (2.3.10) to study the dynamics of a front as it develops from the initial condition. Furthermore, the speed of the front is calculated. We use periodic boundary conditions in these simulations because it is simple and familiar to use. The small random initial condition, $u(x, 0) = 10^{-6}r$ where r is a vector containing random values between 0 and 1, is used in the simulation. The domain size L is discretized by the Fourier spectral method. We use ETD1 method [16] with time step size 0.002 for time discretization. We choose this time step size to balance between time and accuracy. We investigate the dynamics of fronts up to a maximum time $T_m = 300$ for each case except the MMS equation (2.3.10) when $\epsilon = 0.1$ where we have opted $T_m = 10000$ due to the fact that the maximum growth rate λ_m is very small according to linear theory, figure 2.4. Likewise, the domain is discretized by almost 200 point for each wave that is expected according to linear theory because we have a sharp cusp on the front structure in some cases. Cusps are points on the curve defined by a continuous function that are singular points or where the derivative of the function does not exist. But in this work, we mean by cusp a smooth peak.

2.4.2 Numerical results

The simulation of the nonlocal-KS equation (2.3.1) for $\epsilon = 1$ and $L = 32\pi$ (large domain) is shown in the figure 2.5. Each curve in the figure represents the configuration of the front at one instant of time. The front moves along the negative vertical coordinate axis but we subtract the mean of u from all the solutions. The speed of front will be calculated in the next section 2.4.3. Numerical experiments show that the short wavelength corrugations structure of the front arising from initial disturbances merge and form bigger cells and making fewer giant waves when time progresses. According to linear theory, the wavenumber that is corresponding to the maximum growth rate is $k_m = 1.125$ then the wavelength is $l_m = 1.777\pi$. Thus when $L = 32\pi$, we expect 18 peaks on the front near the initial time, figure 2.5(a). Furthermore, we have observed coarsening which is the merging of the small waves to bigger cells gradually making a fewer number of giant waves, figure 2.5(b). This coarsening progress continues between time 40 and 67, when the number of peaks decays gradually, until it reaches one giant cusp which is a pointed end where two roughly parabolic curves meet, figure 2.5(c). The dynamics of this cusp seems to be unstable and new cusps appear on the troughs sporadically and disappear at the crests, figure 2.5(d).

Figure 2.6 shows the number of peaks on the dynamics of the front as a function of time. We show the number of peaks linearly and by using the log to the base 10 scales to be more clear. We observe fast decaying of the number of cusps near the initial time where is between 1 and 3 that is due to a very large number of wrinkles in the small random initial condition. The coarsening is more clearly observed in this figure.

For smaller domain when $k_1 < k < k_2$ where $k_1 \approxeq 0.5$ and $k_2 \approxeq 0.81$, the system has a heteroclinic cycle solution, figures 2.7 and 2.9. It is clear from figure 2.10 that the hetroclinic cycle solution is irregular because it has some spikes. However there is a travelling wave solution when $k_2 < k < k_3$ where $k_3 \approxeq 0.94$, figure 2.8. However the system has steady state stable solution with single cusp for small domain when $k > k_3$, figure 2.11.

In the same equation when $\epsilon = 0.1$ figures 2.12(a)-2.12(d), trace the evolution of the dynamics of the front for some certain times. Overall, in this case it is noticed that the dynamics of the front shows the same behaviour as Kuramoto-Sivashinsky equation (1.5.1) and there is no coarsening. We expect 12 peaks on the front because $k_m = 0.75$ then $l_m = 2.66\pi$ when $L = 32\pi$. Fast decaying of the number of peaks due to the random initial condition is observed, with 12 peaks from time 18 to 58, then it becomes unstable with almost the same number of peaks, figure 2.13. However as for the case when $\epsilon = 1$, for smaller domain the system has a heteroclinic cycle solution and travelling wave solution when $k_1 < k < k_2$ and $k_2 < k < k_3$ respectively where $k_1 \approxeq 0.5$, $k_2 \approxeq 0.55$ and $k_3 = 0.63$. For small domain when $k > k_3$ the model has steady state stable solution with single cusp.

In the MS system (2.3.8) for a large domain, it is clear that the dynamics of the front is similar to the nonlocal-KS system when $\epsilon = 1$ except the current one is smoother, figure 2.14. The number of cusps has decreased to 2 at $t = 45$. These two cusps structure appears to be unstable and new small cusps are created that move toward the giant cusps. As stated by linear theory, $l_m = 4$ when $k_m = \frac{\pi}{2}$ and $L = 32\pi$, the predicted number of peaks on the front is 25. From figure 2.15, we notice that the number of peaks is roughly similar to the case of the nonlocal-KS equation (2.3.1) when $\epsilon = 1$ which has fast decay near initial time due to the random initial condition. In addition, the coarsening appears from time 8 to 45.

In the same system for a small domain when $L < L_n$ where $L_n \approxeq 11\pi$, the dynamics of the front is fast decaying and coarsening until it reaches stable steady state shape with one cusp, for example when $L = 8\pi$ see figures 2.16 and 2.17. In this case, we obtain a structure similar to lobe-and-cleft which has been found in the avalanche front propagation figure 1.3. Although we use the word cusp to describe the giant peaks in the front, we do not mean there is a singularity in the solution or the curve is discontinuous. Figure 2.16(d) shows that the system is well resolved numerically because the curve is smooth.

Figures 2.18(a) through 2.18(d) illustrate the development of the front, based on the MMS equation (2.3.10) for $\epsilon = 1$ and $L = 128\pi$, starting with arbitrary initial data. The small waves introduced through the initial conditions merge until a structure of two cusps is formed. This dynamics of two cusps seems to be unstable and create new small cusps that move towards the giant cusps. In this case $k_m = 0.5$ and then $l_m = 4\pi$ which means the front should have around 32 peaks. We have found the decreasing of the number of peaks near initial time, see figure 2.19, and the dynamics has a clear coarsening from time 30 to 140 until it reaches two cusps. However when $L < L_n$ where $L_n \approxeq 42\pi$, the dynamics of the front has coarsening as time progresses until it reaches a stable steady state propagation regime with a single cusp, for example when $\epsilon = 1$ and $L = 32\pi$ see figures 2.20 and 2.21.

Interestingly even when $\epsilon = 0.1$ in the current model, we have found that the dynamics of the front with small disturbances introduced from initial condition coalesces until it reaches a single cusp. This dynamics also seems to be unstable and new cusps are formed on the troughs and disappear at the crest, figures 2.22(a)-2.22(d). In addition, since $k_m = 0.125$ then $l_m = 16\pi$ while $L = 320\pi$ the front should have nearly 20 peaks, we have found coarsening from time 1000 to 4500 which the number of peaks gradually decreases from 20 to 1, see figure 2.23. In this case, we have obtained the same results but with reaching the stable steady state dynamics with single cusp when $L < L_n$ where $L_n \approxeq 164\pi$.

Note that when $\epsilon = 0$, the MMS equation is Burgers equation which was introduced by Harry Bateman in 1915 [5].

Finally, just to confirm the numerical results we have chosen a different initial condition, $u(x, 0) = 0.1 \cos(kx) + 10^{-3} r$ where r is a vector containing random numbers between 0 and 1. Then we solve all above cases by the same method. Thus we have obtained the same results of the dynamics of the front. We show some figures of some results of this new initial condition to compare with the previous one, for example in the MMS equation (2.3.10) when $\epsilon = 1$ and $L = 32\pi$, see figures 2.24 and 2.25. The results are very similar with a different initial condition, therefore it shows that the initial condition is not very important.

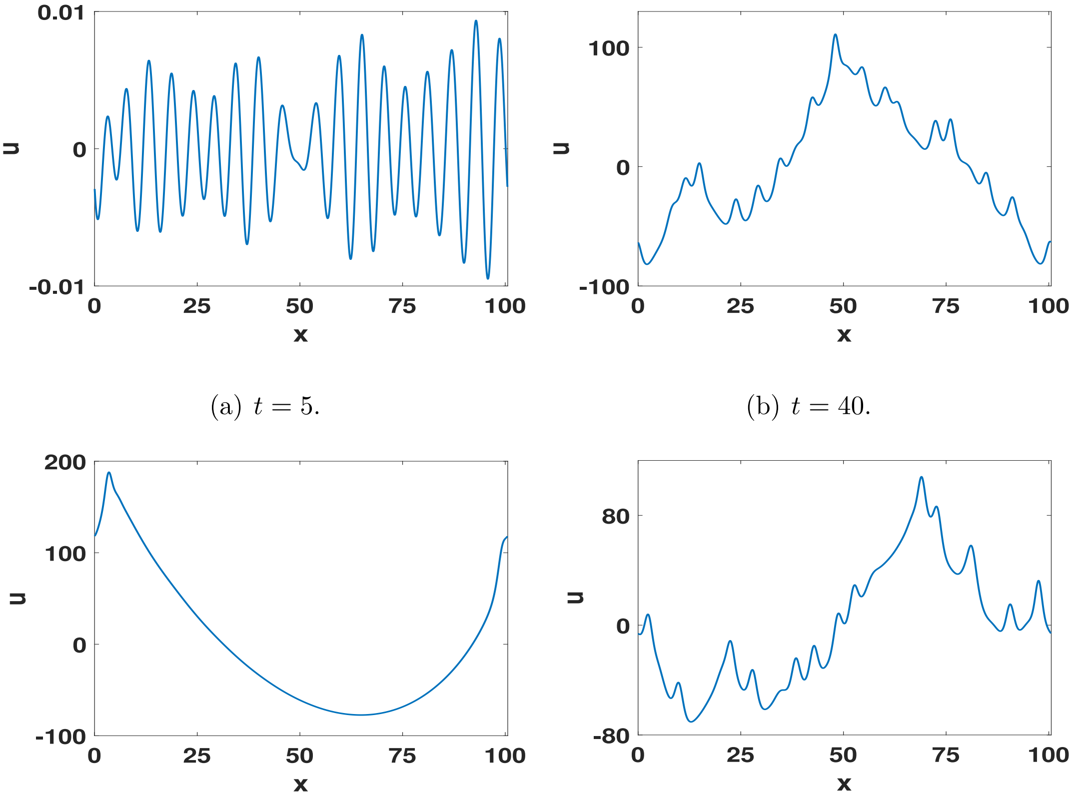

(a) $t = 5$. (b) $t = 40$.

(c) $t = 67$. (d) $t = 300$.

Figure 2.5: Time evolution of a propagating front for the nonlocal-KS equation (2.3.1) for $\epsilon = 1$ and domain $L = 32\pi$.

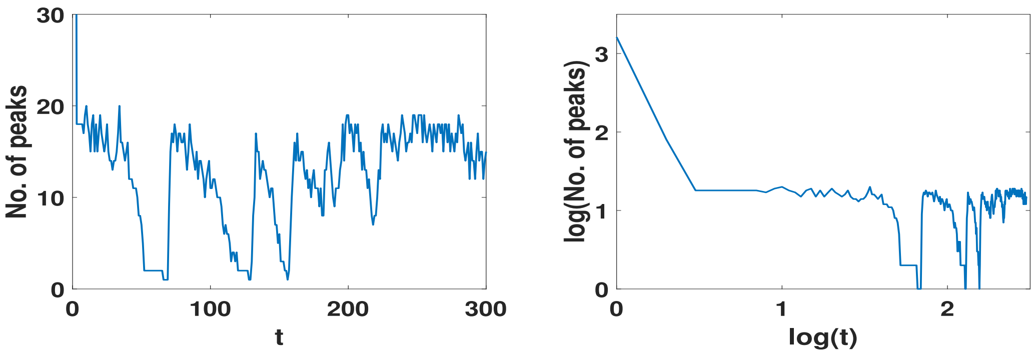

(a) (b)

Figure 2.6: Number of peaks on the front against the time for the nonlocal-KS equation (2.3.1) when $\epsilon = 1$ and $L = 32\pi$.

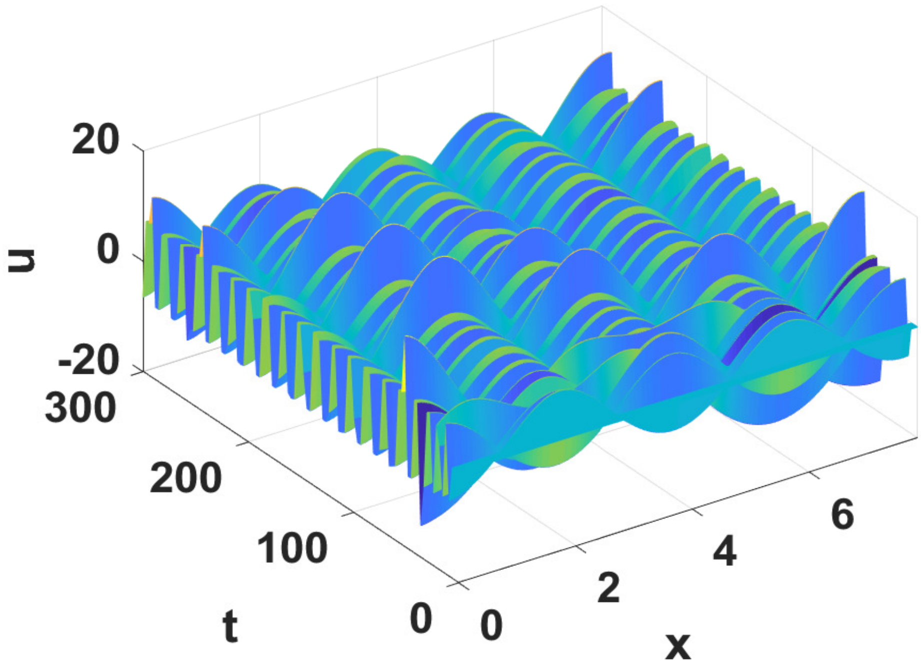

Figure 2.7: Heteroclinic cycle solution of the nonlocal-KS equation (2.3.1) when $\epsilon = 1$ and domain $L = 2.5\pi$.

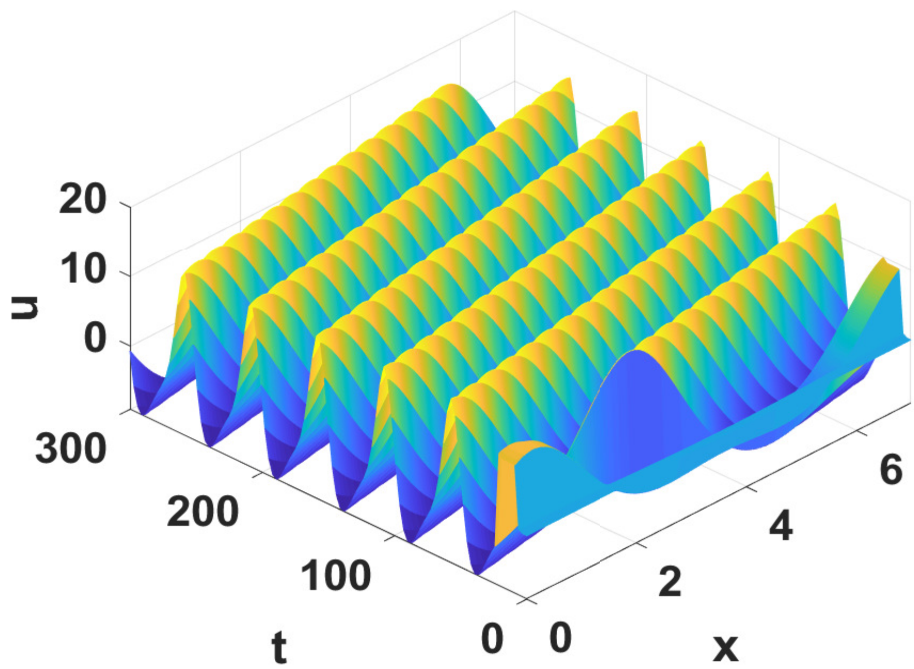

Figure 2.8: Travelling wave solution of the nonlocal-KS equation (2.3.1) when $\epsilon = 1$ and domain $L = 2.2\pi$.

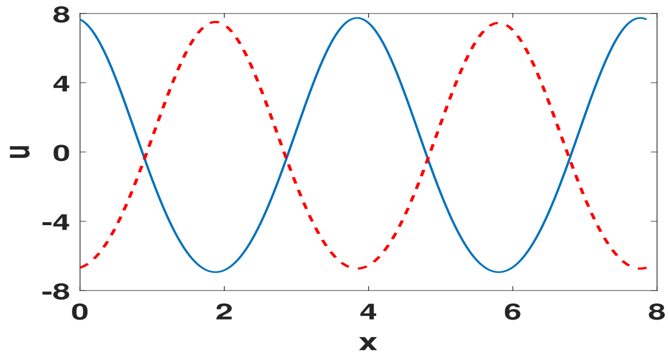

Figure 2.9: Heteroclinic cycle solution of the nonlocal-KS equation (2.3.1) when $\epsilon = 1$ and domain $L = 2.5\pi$ in two different times blue solid line when $t = 200$ and red dashed line when $t = 205$.

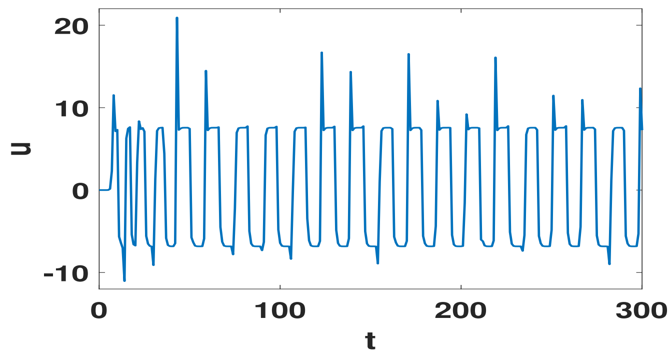

Figure 2.10: u as a function of t from figure 2.7 in a particular value of $x = 2$.

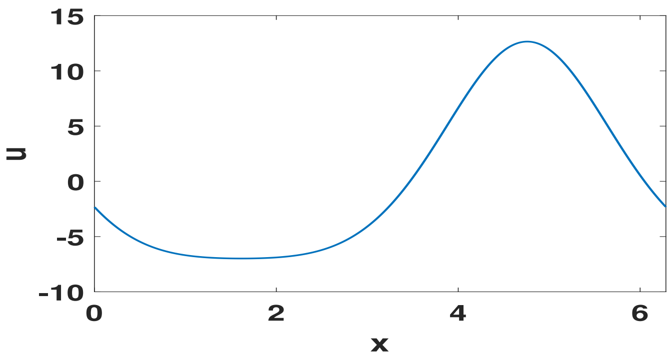

Figure 2.11: Numerical solution of the nonlocal-KS equation (2.3.1) for $\epsilon = 1$ and domain $L = 2\pi$.

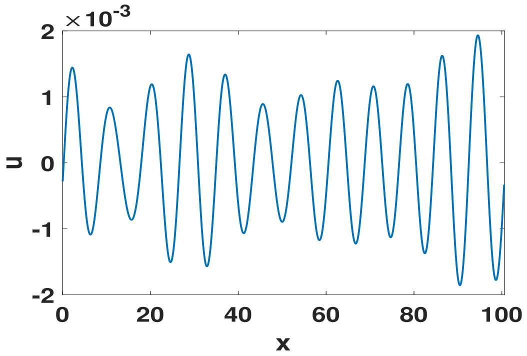

(a) $t = 25$.

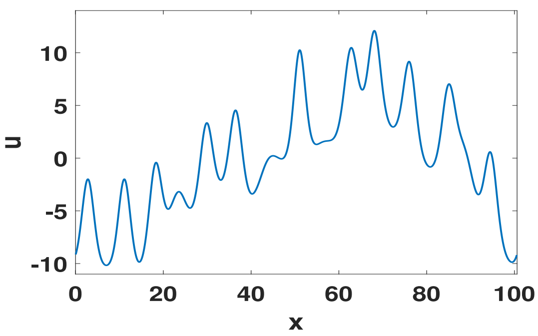

(b) $t = 75$.

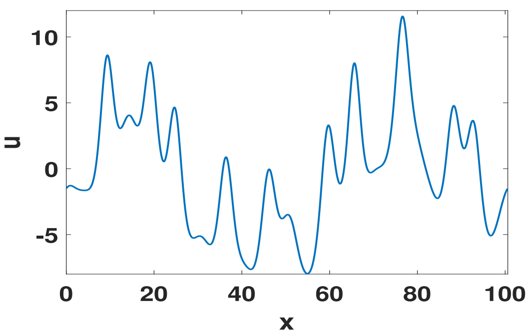

(c) $t = 150$.

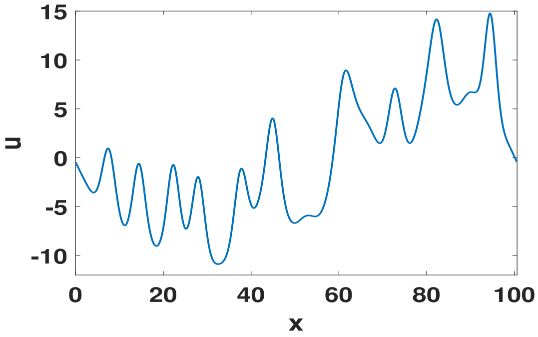

(d) $t = 300$.

Figure 2.12: Time evolution of a propagating front for the nonlocal-KS equation (2.3.1) for $\epsilon = 0.1$ and domain $L = 32\pi$.

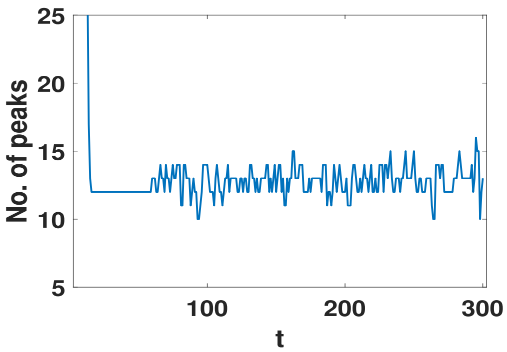

(a)

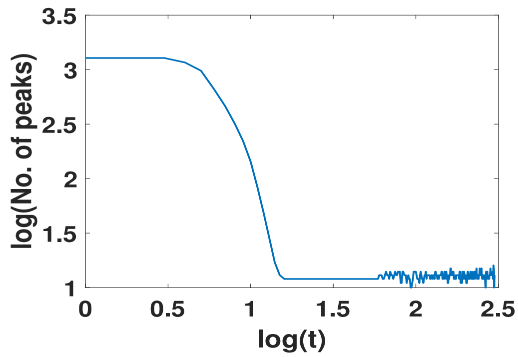

(b)

Figure 2.13: Number of peaks on the front against the time for the nonlocal-KS equation (2.3.1) when $\epsilon = 0.1$ and domain $L = 32\pi$.

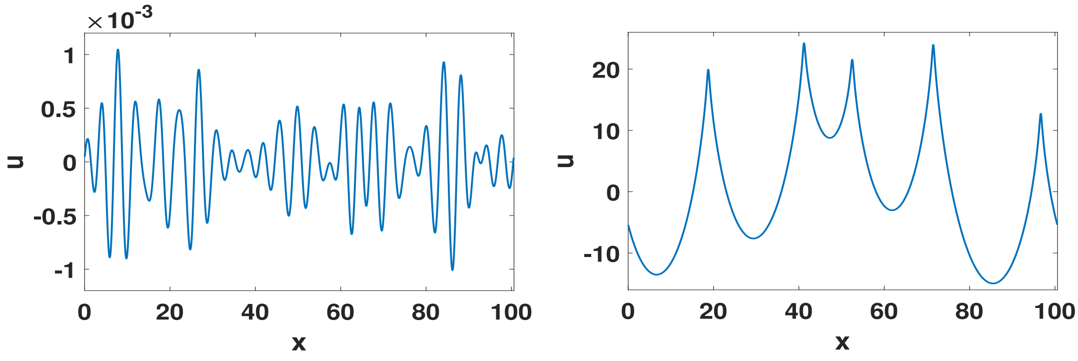

(a) $t = 5$. (b) $t = 20$.

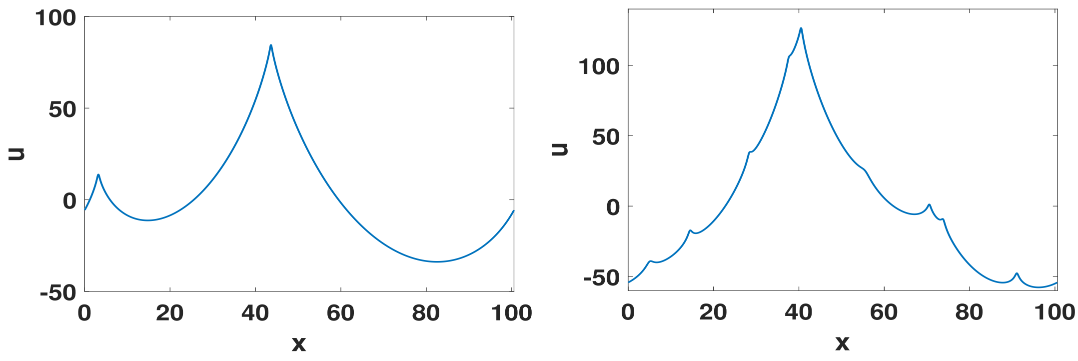

(c) $t = 45$. (d) $t = 95$.

Figure 2.14: Time evolution of a propagating front for the MS equation (2.3.8) when domain $L = 32\pi$.

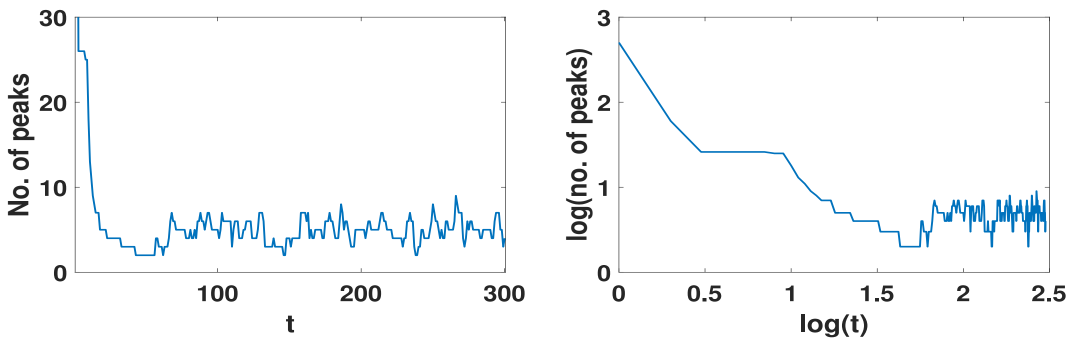

(a) (b)

Figure 2.15: Number of peaks on the front against the time for the MS equation (2.3.8) when domain $L = 32\pi$.

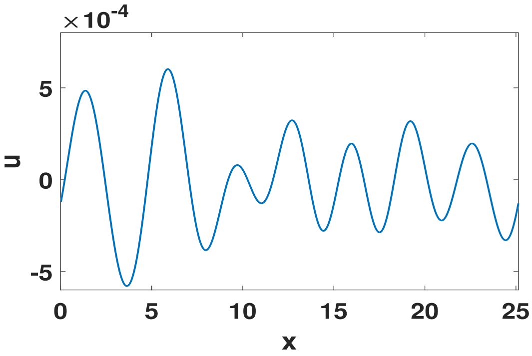

(a) $t = 5$.

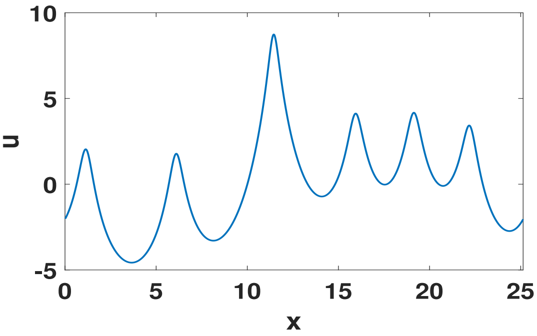

(b) $t = 10$.

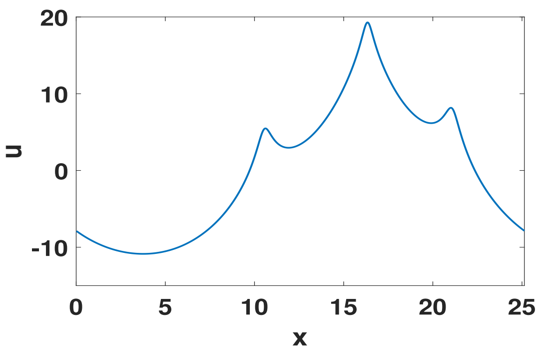

(c) $t = 15$.

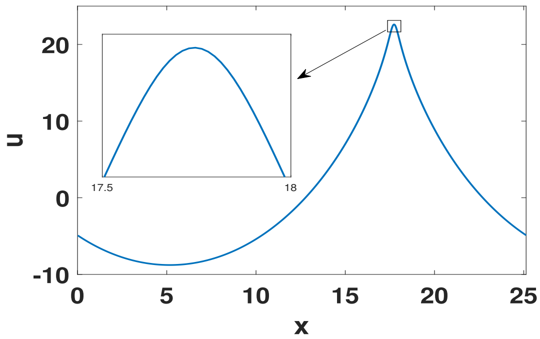

(d) $t = 30$.

Figure 2.16: Time evolution of a propagating front for the MS equation (2.3.8) when domain $L = 8\pi$.

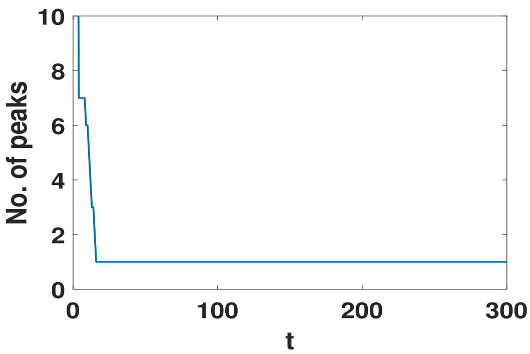

(a)

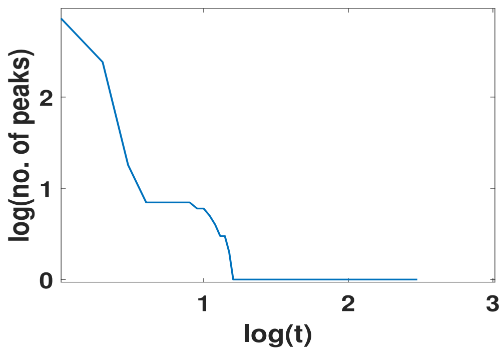

(b)

Figure 2.17: Number of peaks on the front against the time for the MS equation (2.3.8) when domain $L = 8\pi$.

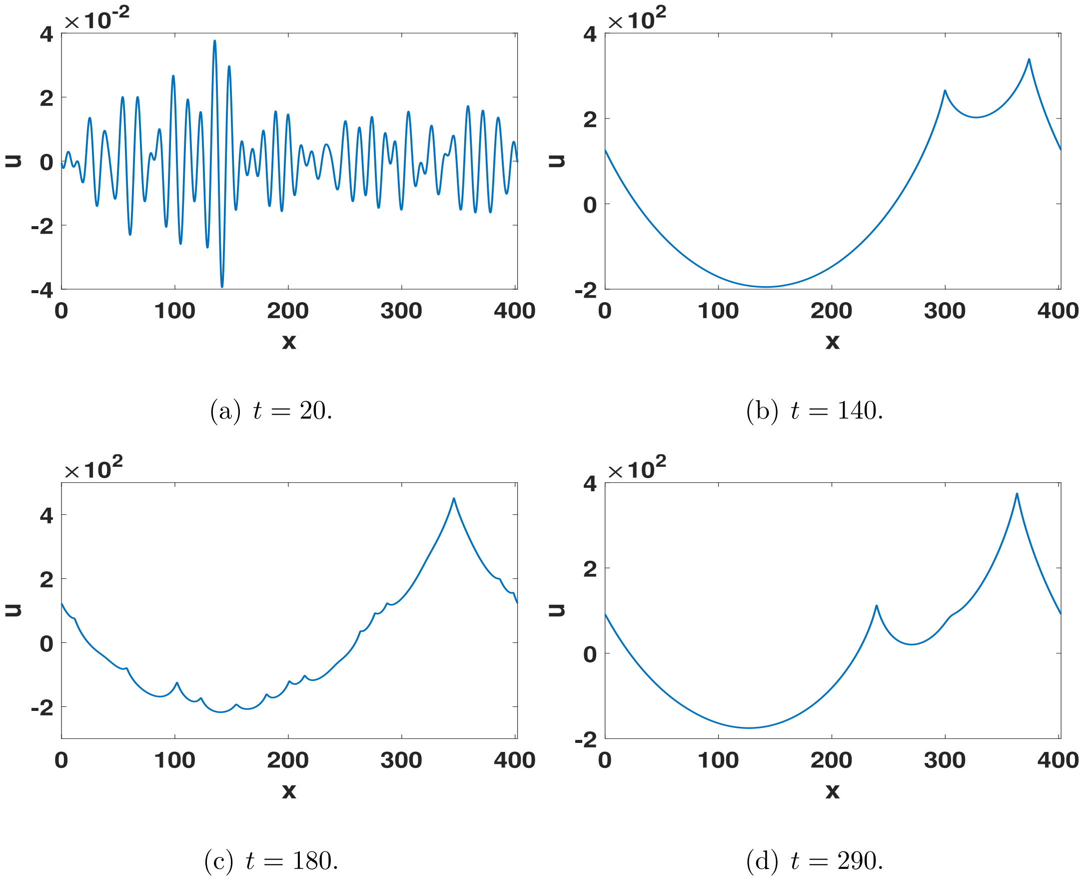

Figure 2.18: Time evolution of a propagating front for the MMS equation (2.3.10) for $\epsilon = 1$ and domain $L = 128\pi$.

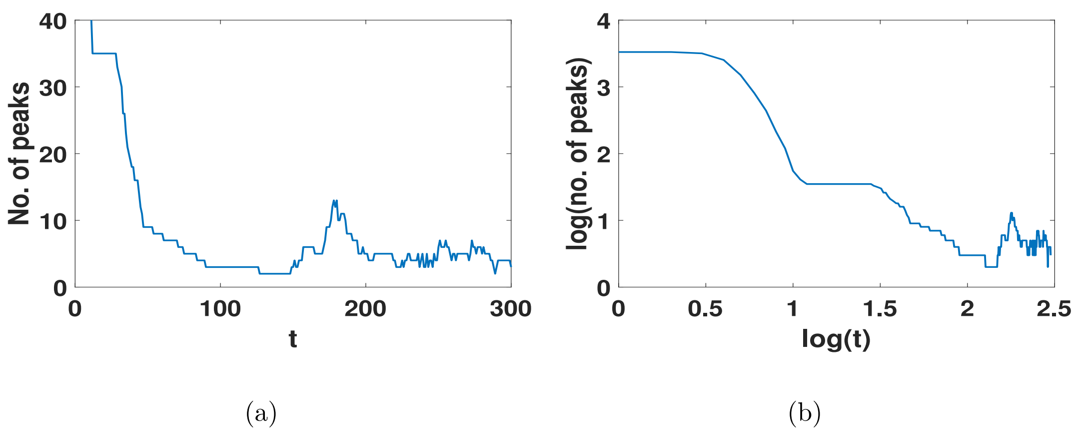

Figure 2.19: Number of peaks on the front against the time for the MMS equation (2.3.10) for $\epsilon = 1$ and domain $L = 128\pi$.

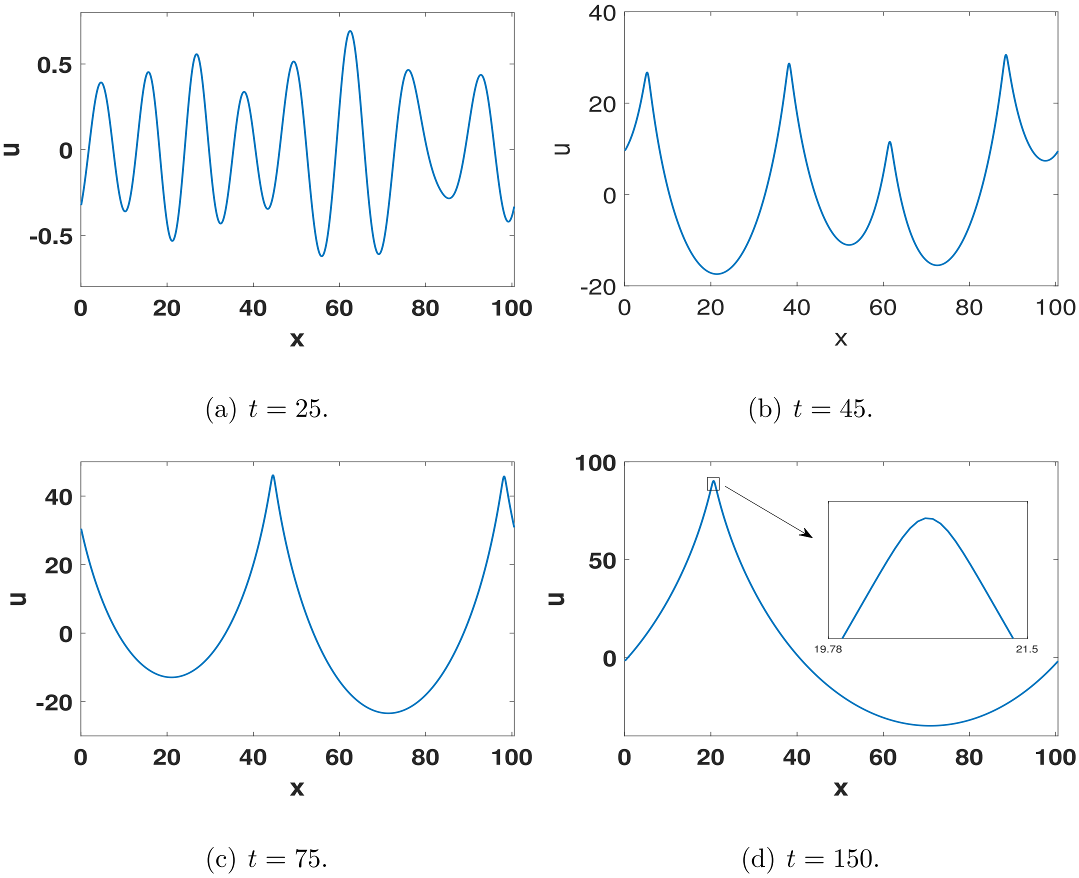

(a) $t = 25$.

(b) $t = 45$.

(c) $t = 75$.

(d) $t = 150$.

Figure 2.20: Time evolution of a propagating front for the MMS equation (2.3.10) for $\epsilon = 1$ and domain $L = 32\pi$.

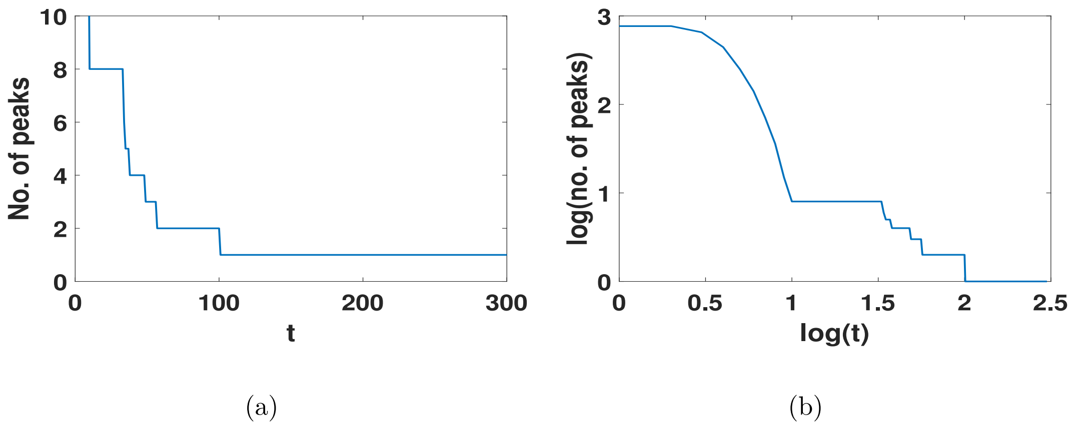

(a)

(b)

Figure 2.21: Number of peaks on the front against the time for the MMS equation (2.3.10) for $\epsilon = 1$ and domain $L = 32\pi$.

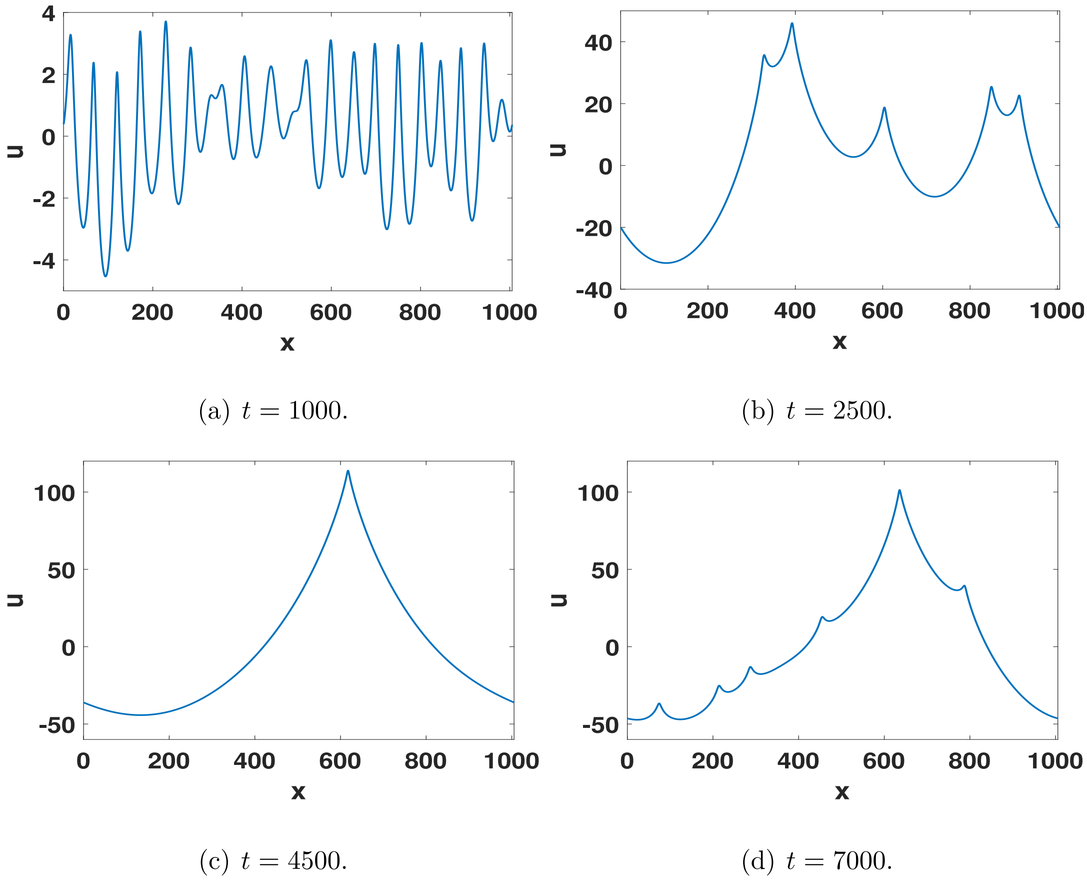

Figure 2.22: Time evolution of a propagating front for the MMS equation (2.3.10) for $\epsilon = 0.1$ and domain $L = 320\pi$.

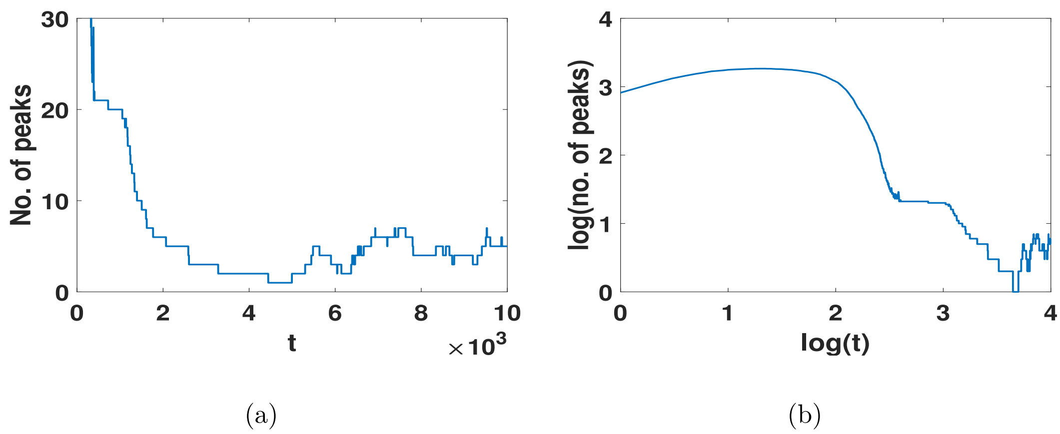

Figure 2.23: Number of peaks on the front against the time for the MMS equation (2.3.10) for $\epsilon = 0.1$ and domain $L = 320\pi$.

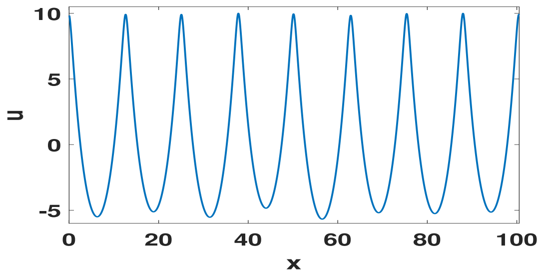

(a) $t = 20$.

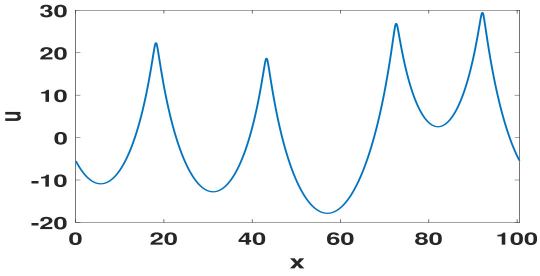

(b) $t = 35$.

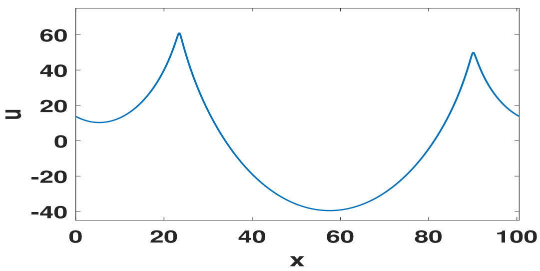

(c) $t = 55$.

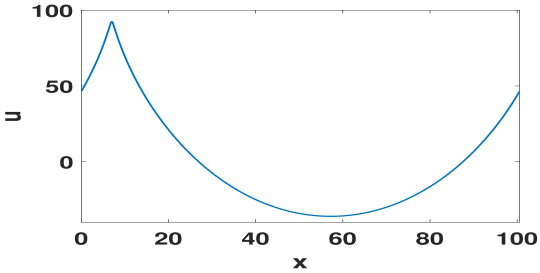

(d) $t = 100$.

Figure 2.24: Time evolution of a propagating front for the MMS equation (2.3.10) for $\epsilon = 1$ and domain $L = 32\pi$. Same as the figure 2.20 with different initial condition, $0.1 \cos(kx) + 10^{-3}r$, where r is a vector containing random numbers between 0 and 1.

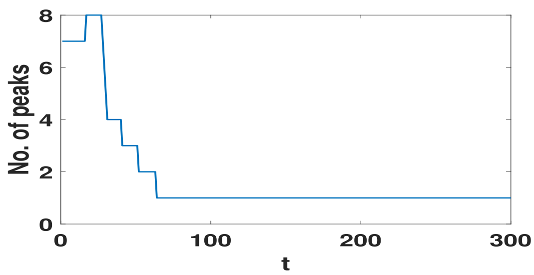

(a)

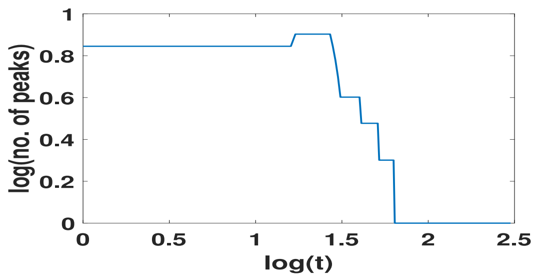

(b)

Figure 2.25: Number of peaks on the front against the time for the MMS equation (2.3.10) for $\epsilon = 1$ and domain $L = 32\pi$. Same as the figure 2.21 with different initial condition, $0.1 \cos(kx) + 10^{-3}r$, where r is a vector containing random numbers between 0 and 1.

2.4.3 Speed of front

In this section, we determine and discuss the speed of front in each case of the three models. The amplitude A, which is the difference between the maximum and minimum point of u at the same time, of the cusp where we have a single cusp in MMS system is obtained. We calculate the speed of front by taking the minimum point in the front in each time, in the other words we find minimum u at each time and calculate the slope. The numerical data shows that the front is propagating along the negative y-axis. Thus, in the nonlocal-KS equation (2.3.1) when $L = 32\pi$ the speed of front propagation is roughly constant $s = -49$ when $\epsilon = 1$, figure 2.26(a). However, the front speed with the same domain and $\epsilon = 0.1$ is about $s = -2.3$, figure 2.26(b). In the MS system (2.3.8) with the same domain as above the speed is almost $s = -10$, figure 2.26(c). In chapter 4 we find the analytical formula for the speed of the front for the MS equation for the stable case. In the MMS equation (2.3.10) the front moves at a speed $s \approx -8.5$ when $\epsilon = 1$ and $L = 128\pi$, figure 2.26(d), and at $s \approx -0.05$ when $\epsilon = 0.1$ and $L = 320\pi$, figure 2.26(e). In general, the speed of the front based on the MMS equation increases with increasing the domain L. Table 2.1 shows the speed of the front with different domains. On the other hand, with the stable steady state solution that has single cusp based on the MMS equation, the speed of the front is constant and proportional to the value of ϵ^2, ($s \approx -5\epsilon^2$) table 2.2. In addition, the amplitude of the cusp A is proportional to ϵ and L by, ($A \approx 1.2\epsilon L$). For instance as we have obtained steady state with one cusp when $\epsilon = 1$ and $L = 32\pi$ the speed is $s \approx -5$, figure 2.26(f), and the amplitude of the cusp is $A \approx 121$, figure 2.20(d).

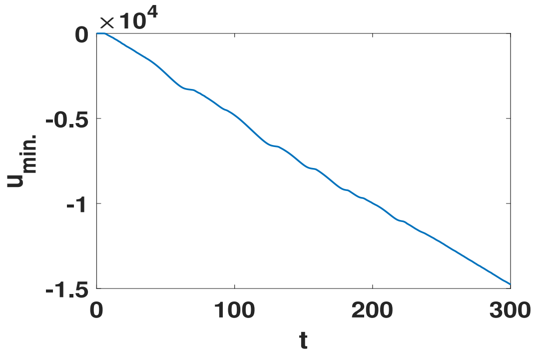

(a) Nonlocal-KS equation (2.3.1) when ϵ=1 and $L = 32\pi$.

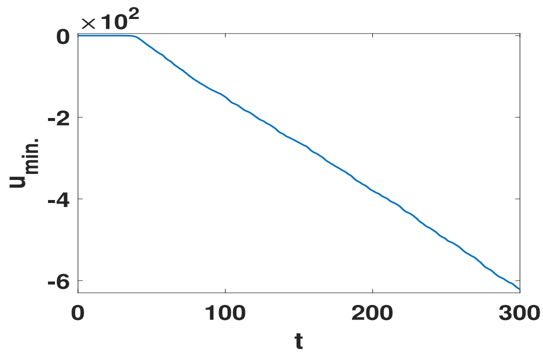

(b) Nonlocal-KS equation (2.3.1) when ϵ=0.1 and $L = 32\pi$.

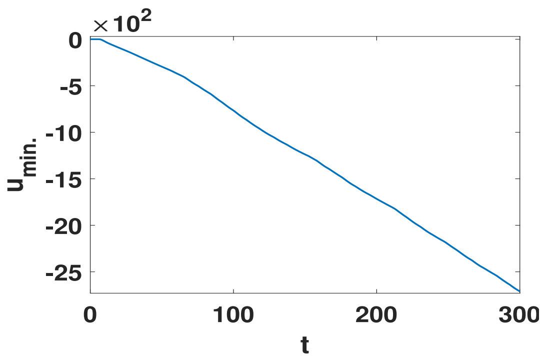

(c) MS equation (2.3.8) when $L = 32\pi$.

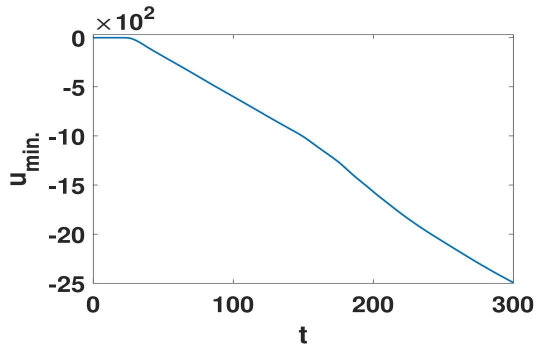

(d) MMS equation (2.3.10) when ϵ=1 and $L = 128\pi$.

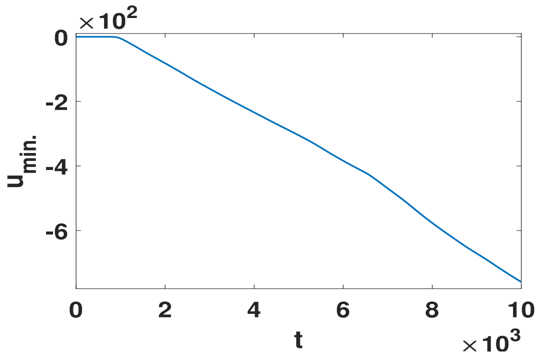

(e) MMS equation (2.3.10) when ϵ=0.1 and $L = 320\pi$.

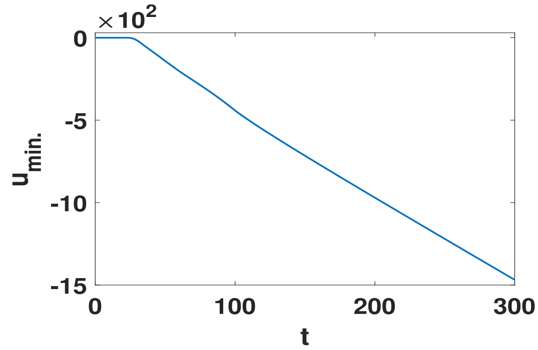

(f) MMS equation (2.3.10) when ϵ=1 and $L = 32\pi$.

Figure 2.26: The location of minimum point of u against time, then by estimating the slope we obtain the speed of front.

$\epsilon = 1$		$\epsilon = 0.1$	
L	s	L	s
200π	-17.25	350π	-0.085
150π	-9.84	300π	-0.083
100π	-7.98	250π	-0.075
50π	-6.12	200π	-0.063
40π	-5.13	150π	-0.057
30π	-4.94	100π	-0.055
20π	-4.91	50π	-0.05
10π	-4.83	25π	-0.046

Table 2.1: The relation between domain L and speed of front s for the MMS equation

	MMS when $L = 32\pi$			MMS when $L = 16\pi$		
ϵ	A	s	$A/(\epsilon L)$	A	s	$A/(\epsilon L)$
1	121	-4.9	1.20	62	-4.9	1.23
0.8	97	-3.16	1.20	49.3	-3.1	1.22
0.5	61	-1.24	1.21	31	-1.22	1.23
0.2	25	-0.2	1.24	12.4	-0.2	1.23
0.1	12.5	-0.05	1.24	6.62	-0.05	1.31

Table 2.2: The relation between amplitude of cusp A and speed of front s with ϵ for the MMS equation.

2.5 Conclusion

In this chapter we have nondimensionalized all three nonlocal-KS (2.2.1), MS (2.2.6) and MMS (2.2.9) systems. Then the dispersion relations of all three models are obtained. We have presented the numerical solution of all three models (2.3.1), (2.3.8) and (2.3.10) by Fourier spectral discretization, while the time discretization is performed by the ETD method.

We have found that the nonlocal-KS model for a large domain when $\epsilon = 1$ is coarsening as time progresses from initial time which eventually one peak in the front dynamic can be seen, but this single-peak seems to be unstable and new cusps appear and merge again. For smaller domain, we have found a heteroclinic cycle and travelling wave solutions. However, for a small domain, the numerical simulations show that the dynamics of the front has stable steady state solution with one cusp. However, when $\epsilon = 0.1$ there is no coarsening and the dynamics of the front stay unstable for a large domain. However there are heteroclinic cycle and travelling wave solutions for a smaller domain, and the front has a stable steady state solution with one cusp for a small domain.

The MS model for the large domain is coarsening until it reaches two cusps, afterwards, the dynamics of the front seems to be unstable and new wrinkles are created on troughs and move toward the large cusps and disappear at the crest. However for a small domain, the dynamics of the front has a stable steady state solution with one cusp.

The dynamics of the front in the MMS model, when $\epsilon = 1$ and $L > L_n$ where

$L_n \approxeq 44\pi$, has a clear coarsening until it reaches a few large cusps, which seems to be unstable and forms new peaks that move toward the large cusps and disappear at the top. However, in the same case when $L \leq L_n$, we have found a stable steady state shape with single cusp. In the same model even with $\epsilon = 0.1$ the coarsening behaviour process was observed. However, as time progresses there are two different behaviours of the dynamics, first one when $L > L_n$ where $L_n \approxeq 164\pi$ the dynamics of the front seems to be unstable after reaching single large cusp and new cusps are created on the trough and move toward the large cusp and disappear at the crest. The second behaviour when $L \leq L_n$ the dynamics become stable stationary with one cusp.

In addition, we have calculated the speed of the front which is roughly constant in each case except when we have a steady state solution with one cusp in MMS system, it seems to be exactly constant and proportional to the value of ϵ^2. Also, we have found the amplitude of the cusp in the MMS equation when we have one cusp which is proportional to ϵ and L.

Although the dynamics of the front for all three models shows similar behaviour, there are a number of important differences among them. First, the stable steady state with one cusp for the MMS equation has the smoothest cusp among them for the same domain. However, the dynamics of one cusp for the nonlocal-KS equation is sharper and for the MS one has the sharpest cusp. Second, in the same state, the nonlocal-KS equation has the largest amplitude dynamics of the front among them while the MMS equation has the smallest. Third, the nonlocal-KS equation has the travelling wave and heteroclinic cycle solutions while there are no such solutions for the MS and MMS equations. Finally, the MMS equation forms a stable coherent structure front for a larger domain than the others, while the nonlocal-KS equation forms a stable coherent structure front for a smaller domain than the others.

Chapter 3

Approximate analytical solution of nonlocal front equations by using Fourier series

3.1 Introduction

In chapter 2 of this work we exhibited the numerical solutions of the nonlocal-KS (2.3.1), MS (2.3.8) and MMS (2.3.10) systems. This chapter provides approximate analytical solutions of all three above nonlocal front systems by expanding the dependent variable $u(x,t)$ as a Fourier series and relating the coefficients. We also present numerical results to confirm that both solutions agree. The outline of this chapter is as follows; In section 3.2 we aim to find the approximate analytical solutions of all three above equations by using three and four modes truncated Fourier series. The approximate analytical solution of all three equations by using general modes of Fourier series is provided in section 3.3. However in section 3.4 we use the complex Fourier series to present the approximate analytical solutions, and section 3.5 is the chapter summary.

3.2 Approximate analytical solutions by using three and four modes Fourier series

We have obtained different types of solutions numerically in chapter 2. In this chapter, we seek for the approximate analytical solution for those cases that have a stationary solution with one cusp, for example figure 2.20(d), by Fourier series expansion. This kind of solution is symmetric wave about the vertical axis, so the Fourier series expansion can be written as

$$u(x,t) = \sum_{n=0}^{\infty} a_n(t)\cos(nkx), \tag{3.2.1}$$

where the wavenumber $k = \frac{2\pi}{L}$ and L is the domain length.

3.2.1 Nonlocal-KS equation

We truncate (3.2.1) by three modes and substitute it in the nonlocal-KS equation (2.3.1) when $\epsilon = 1$, and equating the coefficients of $\cos(nkx)$ gives three ordinary differential equations (ODEs)

$$\frac{da_0}{dt} = \frac{-1}{4}k^2 a_1^2 - k^2 a_2^2, \tag{3.2.2}$$

$$\frac{da_1}{dt} = -k^4 a_1 + k^2 a_1 - k^2 a_1 a_2 + \pi|k|a_1, \tag{3.2.3}$$

$$\frac{da_2}{dt} = -16k^4 a_2 + 4k^2 a_2 + \frac{1}{4}k^2 a_1^2 + 2\pi|k|a_2. \tag{3.2.4}$$

Note that in this case, we will have several particular values of k so we label them k_1 to k_4 where $k_1 < k_2 < k_3 < k_4$. The last two equations (3.2.3) and (3.2.4) do not include a_0 so we can consider them as a separate system of two equations. From these two equations we can obtain the equilibrium points which are

$$a_2 = \frac{-k^4 + k^2 + \pi|k|}{k^2}, \tag{3.2.5}$$

and

$$a_1 = \pm\sqrt{\frac{8(8k^4 - 2k^2 - \pi|k|)(-k^4 + k^2 + \pi|k|)}{k^4}}. \tag{3.2.6}$$

Since $8k^4 - 2k^2 - \pi|k| \geq 0$ when $k \geq k_3$ where $k_3 \approx 0.8454$ and $-k^4 + k^2 + \pi|k| \geq 0$ when $k \leq k_4$ where $k_4 \approx 1.6906$ otherwise they are negative, so the product of both amounts in numerator under the square root is greater than or equal to zero (a_1 has real solution) when $k \in [k_3, k_4]$, see figure 3.1(a). Figure 3.1(b) shows the value of a_2 in the same interval, which is usually smaller than a_1.

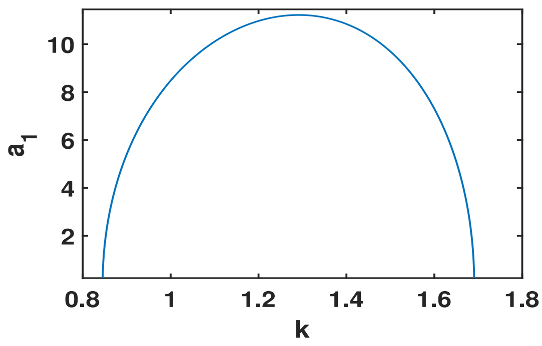

(a) The first Fourier series coefficient a_1 against k.

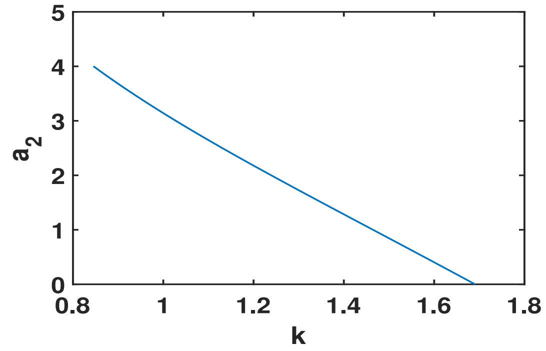

(b) The second Fourier series coefficient a_2 against k.

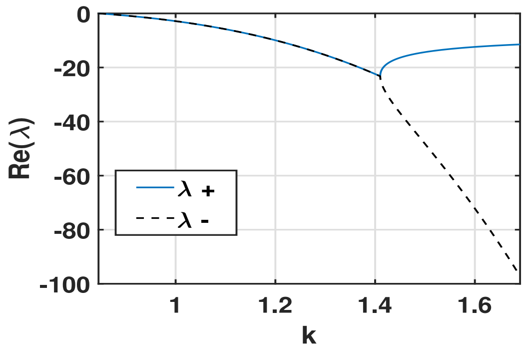

(c) The real part eigenvalues of Jacobian matrix.

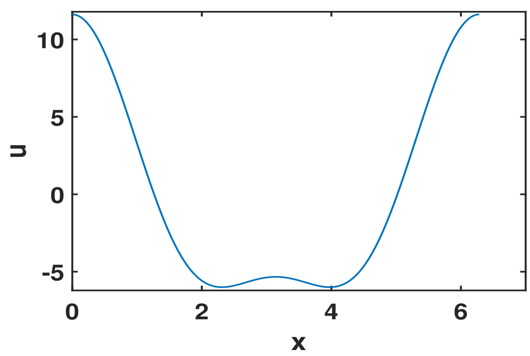

(d) The value of $u = a_1 \cos(kx) + a_2 \cos(2kx)$ when $k = 1$.

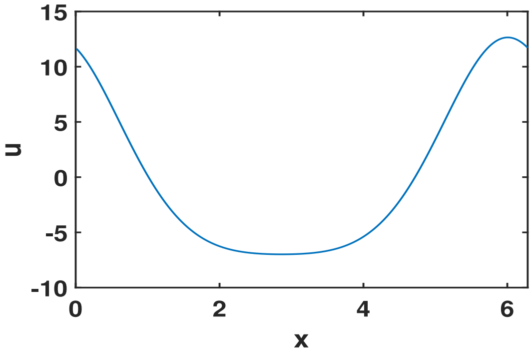

(e) The numerical solution of u against x when $k = 1$.

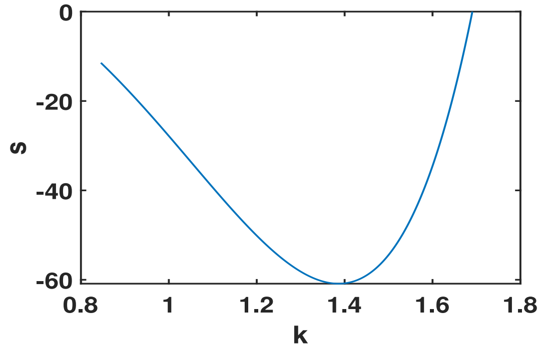

(f) The speed of the front s obtained from a_0.

Figure 3.1: The value of Fourier series coefficients, eigenvalues and the analytical and numerical value of u when we have truncated it by three modes a_0, a_1 and a_2, for the nonlocal-KS equation when $\epsilon = 1$.

To find the stability of the system we find the Jacobian matrix

$$J = \begin{bmatrix} 0 & -a_1k^2 \\ \frac{1}{2}a_1k^2 & -16k^4+4k^2+2\pi|k| \end{bmatrix}.$$

So the eigenvalues of the Jacobian matrix are

$$\lambda = -8k^4+2k^2+\pi k \pm \sqrt{\frac{-1}{2}a_1^2k^4+(-8k^4+2k^2+\pi|k|)^2}, \tag{3.2.7}$$

when $k \in [k_3, k_4]$ the values of λ are complex with negative real parts or negative real values. Figure 3.1(c) shows the eigenvalues λ when the solid and dashed lines represent λ with $+$ and $-$ signs respectively. Then the solution is stable when a_1 has real values.

At this point it is important to realize that, $u = a_0 + a_1\cos(kx) + a_2\cos(2kx)$, figure 3.1(d), is close to the numerical simulation at the same domain, figure 3.1(e), when there is a single wave ($k = 1$) in the domain box ($L = 2\pi$). However the first ODE (3.2.2) gives $a_0 = st$ where s is considered as the speed of front, figure 3.1(f), because $\frac{da_0}{dt}$ is constant. Moreover, the speed is almost -27.8 when $k = 1$ is close to the speed that is found in numerical simulation which is -30 in the same case. The amplitude of the wave in the analytical solution is $A = 17.6$ which is also close to the wave amplitude in the numerical one, $A = 20$.

Similarly, when (3.2.1) is truncated by four terms and substituted in the same model (2.3.1), we obtain a system of four ordinary differential equations

$$\frac{da_0}{dt} = \frac{-1}{4}k^2a_1^2 - k^2a_2^2 - \frac{9}{4}k^2a_3^2 \tag{3.2.8}$$

$$\frac{da_1}{dt} = -k^4a_1 + k^2a_1 - k^2a_1a_2 - 3k^2a_2a_3 + \pi|k|a_1 \tag{3.2.9}$$

$$\frac{da_2}{dt} = -16k^4 a_2 + 4k^2 a_2 + \frac{1}{4}k^2 a_1^2 - \frac{3}{2}k^2 a_1 a_3 + 2\pi|k|a_2 \tag{3.2.10}$$

$$\frac{da_3}{dt} = -81k^4 a_3 + 9k^2 a_3 + k^2 a_1 a_2 + 3\pi|k|a_3. \tag{3.2.11}$$

Again from the last three equations, we find the equilibrium points and they can be determined explicitly as follows

$$a_2 = \frac{Ck^2 a_1^2}{4BC + 6k^4 a_1^2}, \tag{3.2.12}$$

$$a_3 = \frac{k^4 a_1^3}{4BC + 6k^4 a_1^2}, \tag{3.2.13}$$

and

$$(36Ak^8 - 9Ck^8)a_1^4 + (12ABCk^4 - BC^2k^4)a_1^2 + AB^2C^2 = 0, \tag{3.2.14}$$

where $A = -k^4 + k^2 + \pi|k|$, $B = 16k^4 - 4k^2 - 2\pi|k|$ and $C = 81k^4 - 9k^2 - 3\pi|k|$. However, $A = 0$, $B = 0$ and $C = 0$ when $k = k_4$, k_3 and k_1 respectively where $k_1 \approx 0.5635$. Then a_1^2 has two real solutions when $k \in (k_1, k_2)$ where $k_2 \approx 0.7168$, one real solution when $k \in (k_2, k_4]$ and no real solution when $k = k_2$ where a_1 goes to infinity, because the coefficient of a_1^4, which is $36Ak^8 - 9Ck^8$ becomes zero, figure 3.2(a). One of the solutions is shown as a dashed line in figure 3.2 when there are two real solutions. The value of a_2 tends to $\frac{C}{6k^2}$ when a_1 goes to infinity ($k = k_2$), in addition, a_2 is negative when k is in (k_2, k_3) because a_1 is small. Furthermore, when $k \in [k_3, k_4]$ we can realize that a_2 is usually smaller than a_1, figure 3.2(b). Besides, the figure 3.2(c) shows that a_3 is smaller than a_1 and a_2 while $k \in [k_3, k_4]$ and it goes to infinity, $a_3 = \frac{a_1}{6}$, whereas a_1 does. Due to all of these results, we have deduced that the components of Fourier series get smaller as the mode number n increases. So for this range of k the Fourier series should give an accurate approximation of the full system.

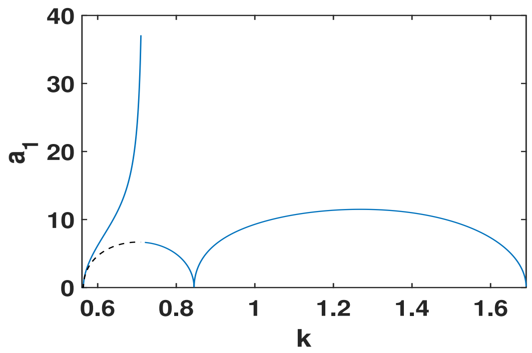

(a) The first Fourier series coefficient a_1 against k.

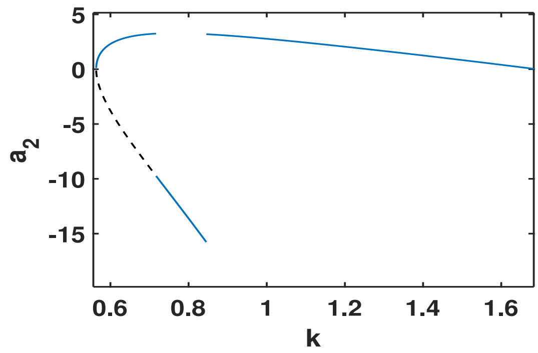

(b) The second Fourier series coefficient a_2 against k.

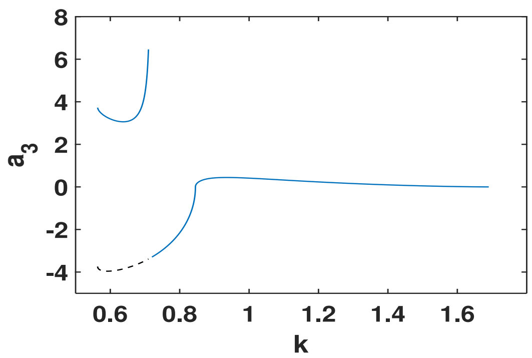

(c) The third Fourier series coefficient a_3 against k.

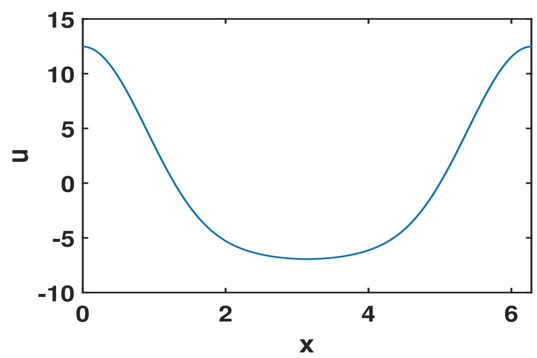

(d) The value of $u = a_1 \cos(kx) + a_2 \cos(2kx) + a_3 \cos(3kx)$ when $k = 1$.

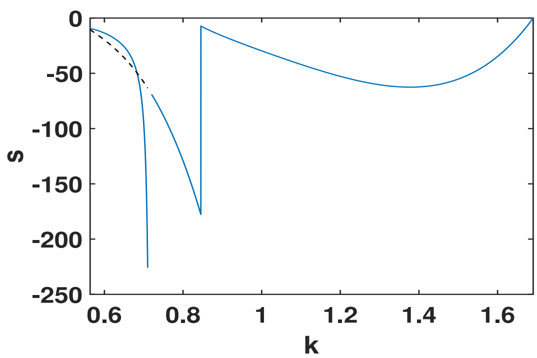

(e) The speed of the front s obtained from a_0.

Figure 3.2: The values of Fourier series coefficients and the value of u when there is one wave in the whole domain, when we have truncated it by four modes for the nonlocal-KS equation when $\epsilon = 1$. The dashed lines indicate a different solution for the same k.

Also in this case the Jacobian matrix can be written as

$$J = \begin{bmatrix} A - a_2k^2 & D & -3a_2k^2 \\ E & -B & -\frac{3}{2}a_1k^2 \\ a_2k^2 & a_1k^2 & -C \end{bmatrix},$$

where $D = -a_1k^2 - 3a_3k^2$ and $E = \frac{1}{2}a_1k^2 - \frac{3}{2}a_3k^2$. Thus, the eigenvalues of the Jacobian matrix are one positive real and two complex with negative real parts when $k \in [k_1, k_3)\backslash\{k_2\}$, one negative real and two complex with negative real parts or three negative real value where $k \in [k_3, k_4]$. We conclude that the system is unstable when $k \in [k_1, k_3)\backslash\{k_2\}$ and it is stable when $k \in [k_3, k_4]$.

On the other hand, $u = a_0 + a_1 \cos(kx) + a_2 \cos(2kx) + a_3 \cos(3kx)$, figure 3.2(d), gives good agreement with numerical simulation when $k = 1$, figure 3.1(e). By the same way as before, the right hand side of the first ODE (3.2.8) is clear from a_0, so $a_0 = st$ where s is the speed of the front and is equal to -29.6 when k=1 which is very close to speed of numerical simulation, $s = -30$, in the same situation, figure 3.2(e).

There are a few differences between the solution that has been found by truncated Fourier series with three modes and four modes. Firstly, we have found the unstable solutions with the four modes truncated in addition to the stable solution which also has been found in three modes truncated. Secondly, the dynamic of the front which is found by four modes truncated Fourier series is more agreed with the numerical simulation than which is found by three modes truncated.

3.2.2 MS equation

The MS equation (2.3.8) is also solved by Fourier series. We truncate (3.2.1) by three modes and substitute in (2.3.8). By balancing all terms, we obtain three ODEs similar to the previous model in section 3.2.1, except they are clear from the terms that include k^4 because the fourth derivative is extracted from the MS equation. Then the nonlinear terms are the same as the previous model, just the linear terms are different. In this case, we can write the equilibrium points as

$$a_2 = \frac{-k^2 + \pi|k|}{k^2}, \tag{3.2.15}$$

and

$$a_1 = \pm\frac{\sqrt{-16k^2 + 24\pi|k| - 8\pi^2}}{k} = \pm\frac{\sqrt{-8(2|k| - \pi)(|k| - \pi)}}{k}, \tag{3.2.16}$$

then a_1 has real solution when $k \in [\frac{\pi}{2}, \pi]$, the same goes for a_2.

Subsequently to know the stability, the Jacobian matrix is again similar to the previous model just without the k^4 term. Thus the eigenvalues of the matrix are as follows

$$\lambda = -2k^2 + \pi|k| \pm \sqrt{12k^4 - 16\pi k^2|k| + 5\pi^2 k^2}, \tag{3.2.17}$$

so the eigenvalues are, zero and a negative real when $k = \pi/2$ or π, and two complex with negative real parts or two negative real values when $k \in (\frac{\pi}{2}, \pi)$. This means that the solutions are stable for all values of k when we have real equilibrium points. The speed and the amplitude of wavefront in this case are -3.2 and 3 respectively, while in the numerical simulation they are -4.5 and 4.

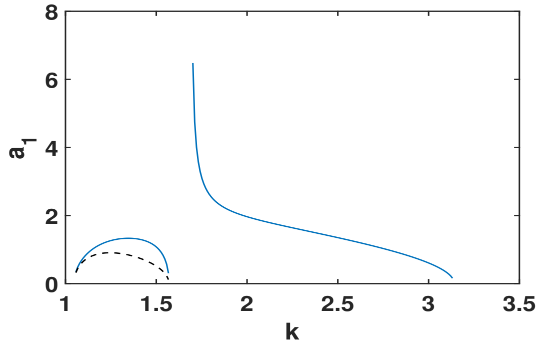

(a) The first Fourier series coefficient a_1 against k.

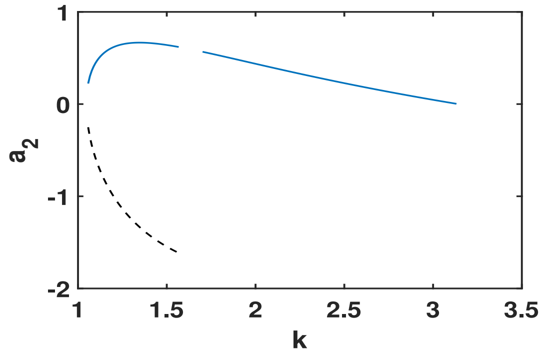

(b) The second Fourier series coefficient a_2 against k.

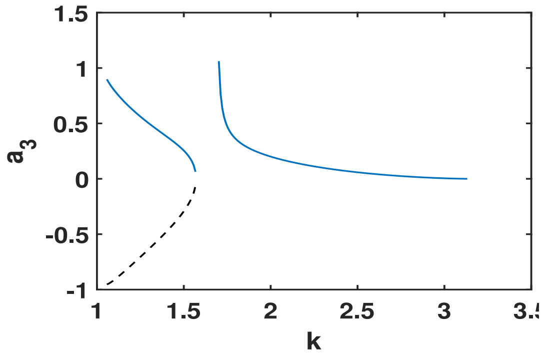

(c) The third Fourier series coefficient a_3 against k.

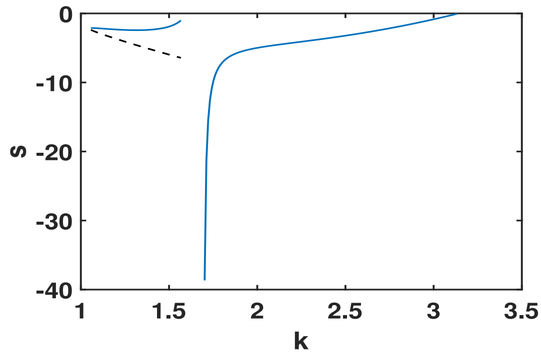

(d) The speed of the front s obtained from a_0.

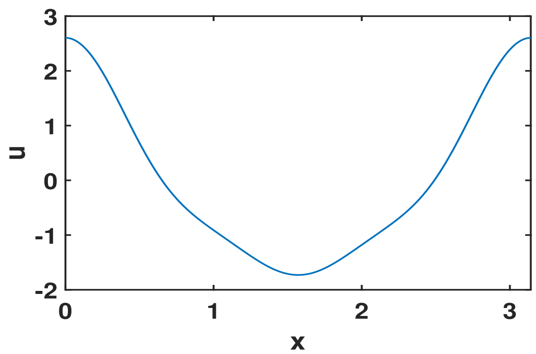

(e) The value of $u = a_1 \cos(kx) + a_2 \cos(2kx) + a_3 \cos(3kx)$ when $k = 2$.

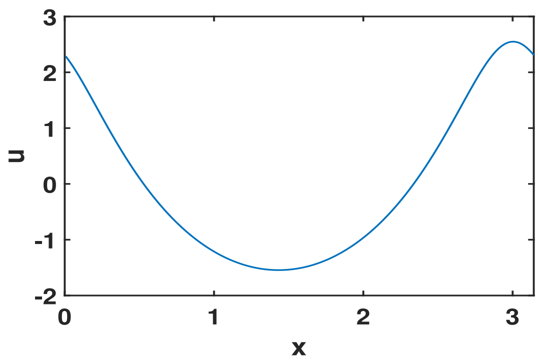

(f) The numerical value of u when $k = 2$.

Figure 3.3: The values of Fourier series coefficients, the value of u when there is one wave in the whole domain numerically and analytically when we have truncated it by four modes for the MS equation. The dashed lines indicate a different solution for the same k.

On the other hand, when we truncate (3.2.1) by four modes and substitute in the MS equation, the result gives a system of four ODEs similar to the previous model of four modes truncated with removing the k^4 term. Similarly the equilibrium points are the same with $A = -k^2 + \pi|k|, B = 4k^2 - 2\pi|k|$ and $C = 9k^2 - 3\pi|k|$. Therefore, a_1 has two real solutions when $k \in (\frac{\pi}{3}, \frac{\pi}{2})$ (one of them is shown as dashed line), one real solution when $k \in (\frac{7\pi}{13}, \pi)$ and is zero when $k = \frac{\pi}{2}$ or π, a_1 goes to infinity when $k = \frac{7\pi}{13}$, figure 3.3(a). Then a_2 has real solutions when $k \in (\frac{\pi}{3}, \frac{\pi}{2}] \cup [\frac{7\pi}{13}, \pi]$ and goes to $\frac{C}{6k^2}$ when a_1 goes to infinity, figure 3.3(b). The value of a_3 goes to infinity when a_1 does and it has solution when a_1 does, figure 3.3(c). From the values of a_1, a_2 and a_3 we have realized that the Fourier coefficients get smaller as number of modes n increase.

For stability in this case, the Jacobian matrix is analogous to the previous model. Then the eigenvalues are two complex with negative real parts and one positive real when $k \in (\frac{\pi}{3}, \frac{\pi}{2}]$ for both solutions, two complex with negative real parts and one negative real when $k \in (\frac{7\pi}{13}, \pi]$. Thus the solution is stable when $k \in (\frac{7\pi}{13}, \pi]$ otherwise it is unstable.

The speed of front when $k = 2$, figure 3.3(d), is -4.9 and the amplitude of the wave is 4.3 which are very close to numerical simulation which are -4.5 and 4 respectively. In addition, the value of $u = a_0 + a_1 \cos(kx) + a_2 \cos(2kx) + a_3 \cos(3kx)$, figure 3.3(e), gives a good approximation to numerical simulation when k=2, figure 3.3(f).

3.2.3 MMS equation

After we have solved equations (2.3.1) and (2.3.8), it is easy to find the approximate solution of the MMS equation (2.3.10). We choose $\epsilon = 1$. Then in the same way for three modes Fourier series, we have three ODEs same as the MS equation status except for the last term of both second and third ODEs which are $\pi|k|e^{-|k|}a_1$ and $2\pi|k|e^{-2|k|}a_2$ respectively. Then the equilibrium points are

$$a_2 = \frac{-k^2 + \pi|k|e^{-|k|}}{k^2}, \tag{3.2.18}$$

and

$$a_1 = \pm\frac{\sqrt{-16k^2 + 16\pi|k|e^{-|k|} + 8\pi|k|e^{-2|k|} - 8\pi^2 e^{-3|k|}}}{k} = \pm\frac{\sqrt{(-16|k| + 8\pi e^{-2|k|})(|k| - \pi e^{-|k|})}}{k}, \tag{3.2.19}$$

so the value of a_1 is real when $k \in [k_2, k_4]$ where $k_2 \approx 0.5369$ and $k_4 \approx 1.0736$.

The Jacobian matrix and its eigenvalues can be written as follows

$$J = \begin{bmatrix} 0 & -a_1 k^2 \\ \frac{1}{2}a_1 k^2 & -4k^2 + 2\pi|k|e^{-2|k|} \end{bmatrix},$$

$$\lambda^2 + (4k^2 - 2\pi|k|e^{-2|k|})\lambda + \frac{1}{2}a_1^2 k^4 = 0, \tag{3.2.20}$$

then the solution is stable when $k \in [k_2, k_4]$. In addition, we have observed that the speed of front and the amplitude of the wave are $s = -0.5134$ and $A = 2.8$ which are close to numerical simulations $s = -0.543$ and $A = 2.9$, also the value of $u = a_0 + a_1 \cos(kx) + a_2 \cos(2kx)$ is close to the numerical one.

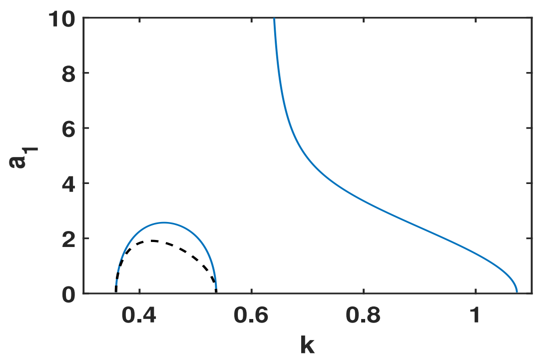

(a) The first Fourier series coefficient a_1 against k.

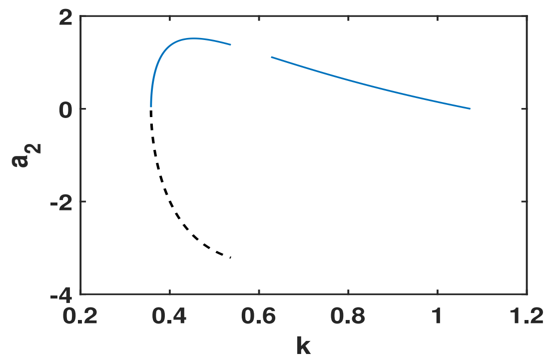

(b) The second Fourier series coefficient a_2 against k.

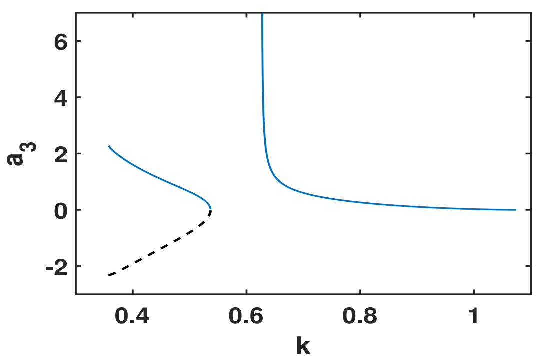

(c) The third Fourier series coefficient a_3 against k.

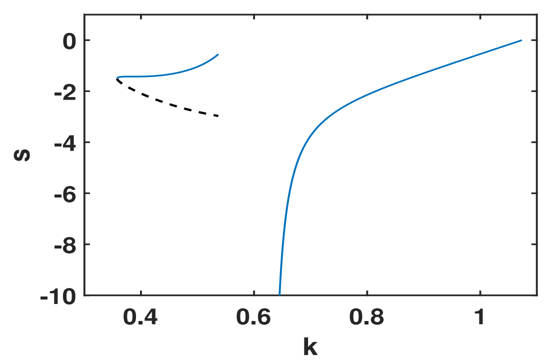

(d) The speed of the front s obtained from a_0.

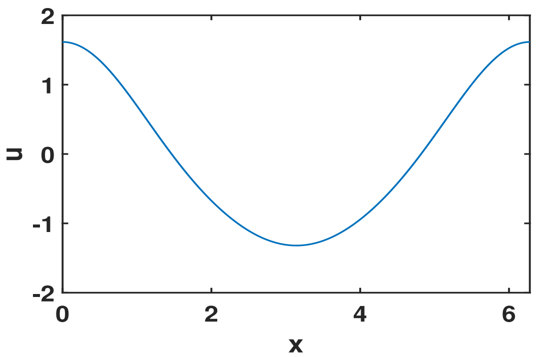

(e) The value of $u = a_1 \cos(kx) + a_2 \cos(2kx) + a_3 \cos(3kx)$ when $k = 1$.

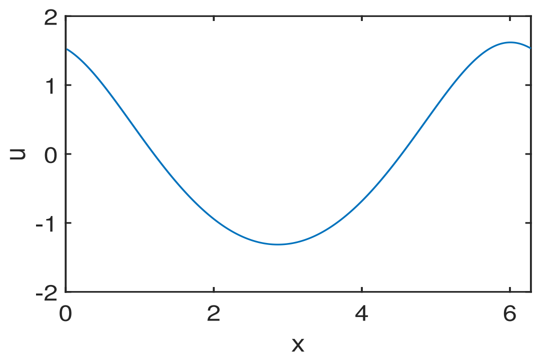

(f) The numerical value of u when $k = 1$.

Figure 3.4: The values of Fourier series coefficients, the value of u when there is one wave in the whole domain along x numerically and analytically when we have truncated it by four modes for the MMS equation when ϵ=1. The dashed lines indicate a different solution for the same k.

In the case of four modes the MMS equation gives four ODEs also same as previous model except the last terms of the last three ODEs which are $\pi|k|e^{-|k|}a_1$, $2\pi|k|e^{-2|k|}a_2$ and $3\pi|k|e^{-3|k|}a_3$ respectively. Moreover, the equilibrium points are the same with $A = -k^2 + \pi|k|e^{-|k|}$, $B = 4k^2 - 2\pi|k|e^{-2|k|}$ and $C = 9k^2 - 3\pi|k|e^{-3|k|}$.

The eigenvalues of the Jacobian matrix indicate that the solution is unstable when $k \in [k_1, k_2)$ where $k_1 \approx 0.3579$ and stable when $k \in (k_3, k_4]$ where $k_3 \approx 0.6270$. However figure 3.4(a) shows that, when $k \in [k_2, k_3)$ a_1 has no real solution and goes to infinity when $k = k_3$, also a_3 goes to infinity with the same k value, figure 3.4(c) and a_2 approaches to $\frac{C}{6k^2}$, figure 3.4(b). In this case the speed of front $s = -0.5422$, the amplitude of wave $A = 2.9$ and the value of $u = a_0 + a_1 \cos(kx) + a_2 \cos(2kx) + a_3 \cos(3kx)$, figure 3.4(e) corresponds better with numerical simulation, figure 3.4(f), than the three modes truncated solution.

3.3 Approximate analytical solutions by using general form of Fourier series

In the last section 3.2 we focus on seeking the analytical solution of the nonlocal front equations by truncated Fourier series to three and four modes. Although we have not solved it analytically, in this section we study the general form of the Fourier series for the solution of all three equations (2.3.1), (2.3.8) and (2.3.10) which is written in equation (3.2.1). We mean by the general form that the arbitrary constant N is used instead of the number of modes. We still use the cosine Fourier series expansion to find the solution of the nonlocal front equations. This means that only solutions with a reflection symmetry can be obtained. We truncate (3.2.1) for N terms and substitute in the nonlocal-KS (2.3.1), MS (2.3.8) and MMS (2.3.10) equations. Then all linear terms in the front equations can be written as

$$\frac{du}{dt} = \sum_{n=0}^{N} \frac{da_n}{dt} \cos(nkx)$$

$$\frac{d^2u}{dx^2} = -\sum_{n=1}^{N} n^2k^2a_n \cos(nkx)$$

$$\frac{d^4u}{dx^4} = \sum_{n=1}^{N} n^4k^4a_n \cos(nkx)$$

$$\int_{-\infty}^{\infty} \frac{-\sum_{n=1}^{N} nka_n \sin(nkx^*)}{x-x^*}dx^* = -\sum_{n=1}^{N} n\pi|k|a_n \cos(nkx)$$

$$\int_{-\infty}^{\infty} \frac{-(x-x^*)\sum_{n=1}^{N} nka_n \sin(nkx^*)}{1+(x-x^*)}dx^* = -\sum_{n=1}^{N} n\pi|k|a_n e^{-n|k|} \cos(nkx).$$

However, the nonlinear term can be written as

$$\Big(\frac{du}{dx}\Big)^2 = \Big(\sum_{n=1}^{N} nka_n \sin(nkx)\Big)^2 = \sum_{i=1}^{N}\sum_{j=1}^{N} ija_ia_jk^2 \sin(ikx)\sin(jkx),$$

which can be written in terms of cosine as

$$\Big(\frac{du}{dx}\Big)^2 = \sum_{i=1}^{N}\sum_{j=1}^{N} ija_ia_jk^2\frac{1}{2}\Big(\cos((i-j)kx) - \cos((i+j)kx)\Big).$$

So the coefficients of $\cos(mkx)$ for the nonlinear term are

$$-\sum_{j=1}^{m} \frac{1}{2}(m-j)ja_{m-j}a_jk^2, \qquad \text{when} \quad m = i+j$$

and

$$\sum_{j=1}^{N-m} (m+j)ja_{m+j}a_jk^2, \qquad \text{when} \quad m = i-j.$$

Then after comparing all terms of the nonlocal-KS, MS and MMS equations gives a general system of ODEs

$$\frac{da_0}{dt} = \frac{-1}{4}\sum_{j=0}^{N} j^2k^2a_n^2, \tag{3.3.1}$$

and

$$\frac{da_m}{dt} = Aa_m - \frac{1}{2}\Big(\sum_{j=1}^{m}\frac{j(j-m)}{2}k^2 a_j a_{m-j} + \sum_{j=1}^{N-m} j(j+m)k^2 a_j a_{m+j}\Big), \quad (3.3.2)$$

where A is $-m^4k^4 + m^2k^2 + \epsilon m\pi|k|$, $-m^2k^2 + m\pi|k|$ and $-m^2k^2 + \epsilon m\pi|k|e^{-m|k|}$ respectively and N is the number of truncated modes.

We use the MATLAB function "fsolve" to solve the nonlinear system (3.3.2), for $N = 100$ and find the equilibrium points. There are particular values of k where the solution is bifurcated from zero and we expect the values of them from the growth rate. Thus we choose an initial guess near each of these points and consider the new point of the solution as an initial condition for the next point and so on. Furthermore, the small step size of $k = 0.001$ is used and a small tolerance of 10^{-10}. Thus we obtain several non-zero solutions when $k \in [0, \pi]$ for each equation.

To find the stability of all three systems (2.3.1), (2.3.8) and (2.3.10), we can obtain the general form of the Jacobian matrix from (3.3.2) which can be written as

$$J = \begin{cases} B - i^2k^2 a_{2i}, & i = j \\ \frac{-j(j-i)}{2}k^2 a_{|j-i|} - \frac{j(j+i)}{2}k^2 a_{j+i}, & i \neq j. \end{cases}$$

where B is $-i^4k^4 + i^2k^2 + \epsilon i\pi k$, $-i^2k^2 + i\pi k$ and $-i^2k^2 + \epsilon i\pi k e^{-i|k|}$ respectively. Then when $N = 100$ we use the MATLAB command "eig" to find the eigenvalues of the Jacobian matrix.

Figure 3.5 shows the non-zero solution and stability of ODEs (3.3.2) for the nonlocal-

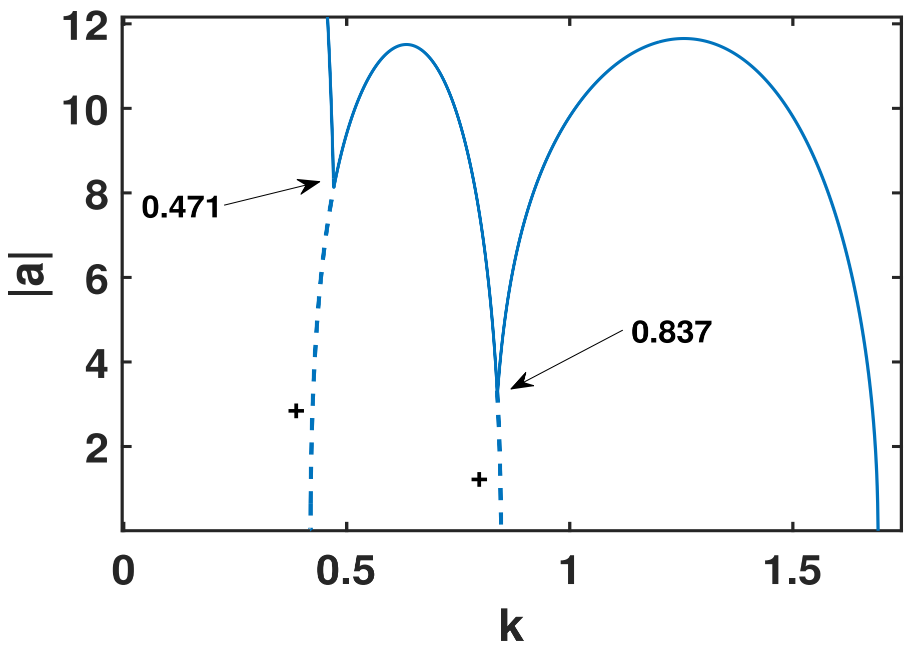

Figure 3.5: Bifurcation diagram for the nonlocal-KS system (2.3.1) when $\epsilon = 1$. Stable branches are shown as solid lines and unstable branches are shown as dashed line. The number of $(+)$ signs indicates the number of positive eigenvalues.

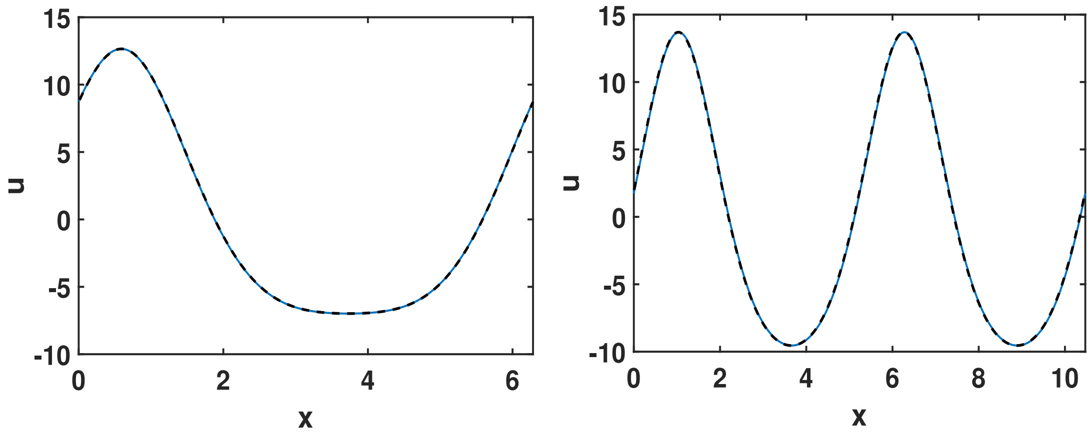

(a) When ϵ=1 and $k = 1$.

(b) When ϵ=1 and $k = 0.6$.

Figure 3.6: Comparison between Fourier series solution (solid line) for a truncated nonlocal-KS system (2.3.1) to 100 terms with numerical (dashed line).

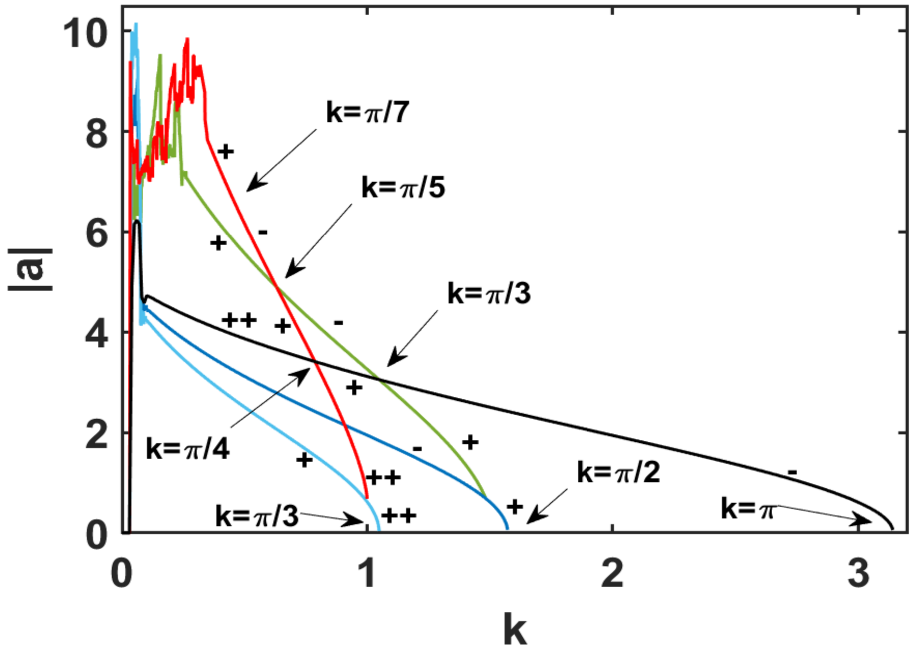

Figure 3.7: Bifurcation diagrams for the MS equation (2.3.8). The number of (+) signs indicates the number of positive eigenvalues.

KS equation (2.3.1) when $\epsilon = 1$, which is unstable with one positive eigenvalue (dashed line) and stable in solid line. Note that $|a|$ is the norm of coefficients of the Fourier series. In addition, when the solution is stable we compare it with numerical solution and it gives a good agreement, for example when $k = 1$ see figure 3.6. Furthermore, when $\epsilon = 1$ and $k > 0.837$ the solution of nonlocal-KS equation contains one wave, figure 3.6(a). However when $k < 0.837$ or for the other wave in figure 3.5 the solution of the nonlocal-KS equation contains two waves figure 3.6(b). Note that we have obtained the same results for the value of $\epsilon = 0.1$.

Now we seek the solution of (3.3.2) for the MS equation (2.3.8). In this case, due to bifurcation points that we have, sometimes the solution switches from one solution to another one in crossing points, but we solve this problem by choosing other initial guesses. The bifurcation diagram, figure 3.7, illustrates the stable and

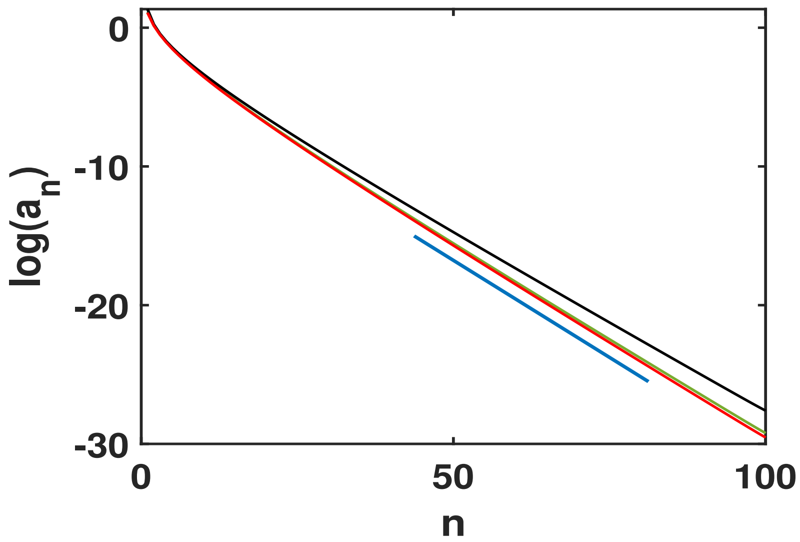

Figure 3.8: The amplitude of a_ns for all three solutions in figure 3.7 of the MS equation (2.3.8) when $k = 0.8$. Each color represents the same color in the figure 3.7. The straight blue line is a line with slope roughly -0.3.

unstable solutions. The $-$ is used as an indicator for stable branches while the number of $+$ signs indicates the number of positive eigenvalues for that solution. We get a transcritical bifurcation when k is $\frac{\pi}{3}$ and $\frac{\pi}{5}$. We will investigate these bifurcation points in chapter 4. The convergence of Fourier series indicates that we have a good approximation to the solution whereas the amplitude of the a_n decays with slope roughly -0.3 when n goes to infinity, which means a_n is proportional to $\exp(-0.3 * n)$ for large n, figure 3.8.

Figures 3.9(a), 3.9(b) and 3.9(c), show that all solutions agree when we choose different values of N, $N = 100$ and $N = 120$, except for small k solutions are not accurate. This is because there are many branches of solutions when k is small, so it jumps between solutions. Even when we change the step size the solution keeps jumping from a solution to another. The stable solution gives a good approximation

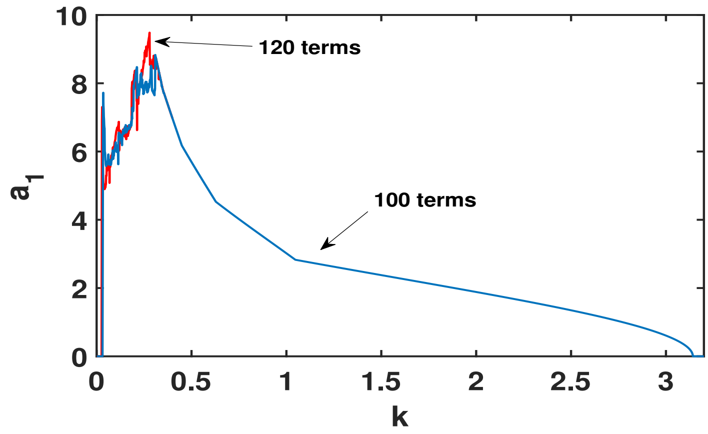

(a) Black solution.

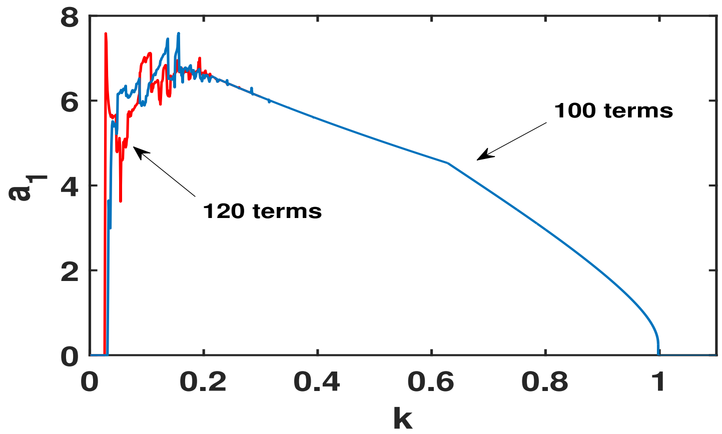

(b) Red solution.

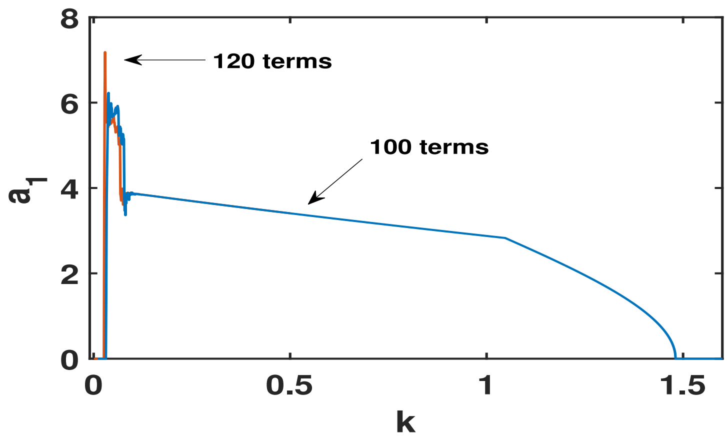

(c) Green solution.

Figure 3.9: Same as the figure 3.7 but one time truncated by 100 terms and another time by 120.

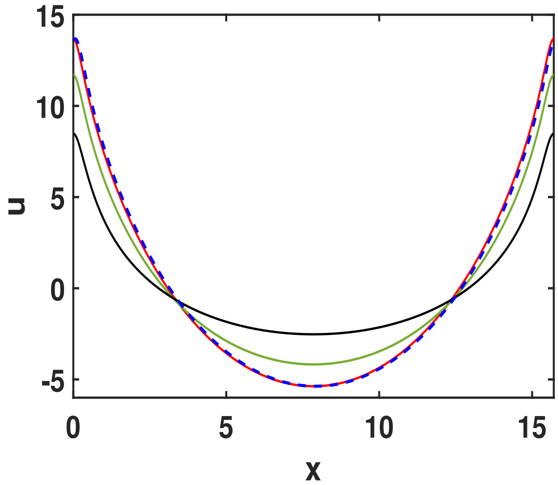

(a) When k=0.4.

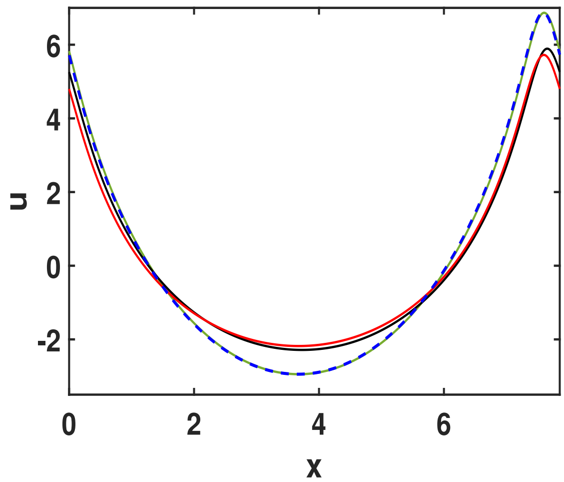

(b) When k=0.8.

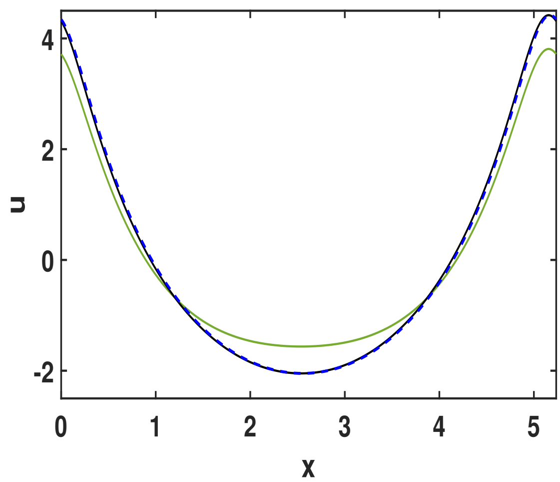

(c) When k=1.2.

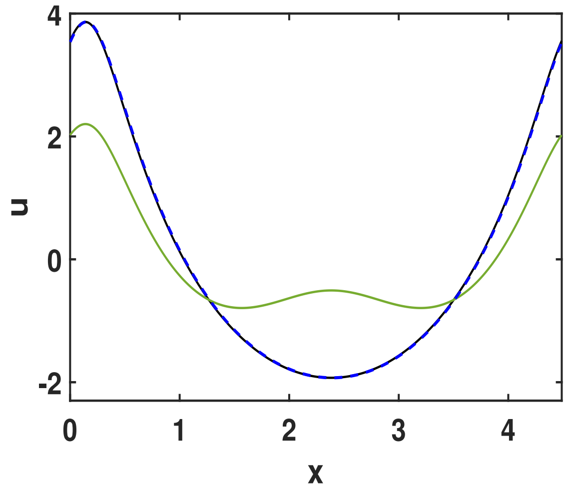

(d) When k=1.4.

Figure 3.10: Comparison between Fourier series solution (solid line) for a truncated MS system (2.3.8) to 100 terms with numerical (dashed line). Each colored line represents the solution of the same color branch in the figure 3.7.

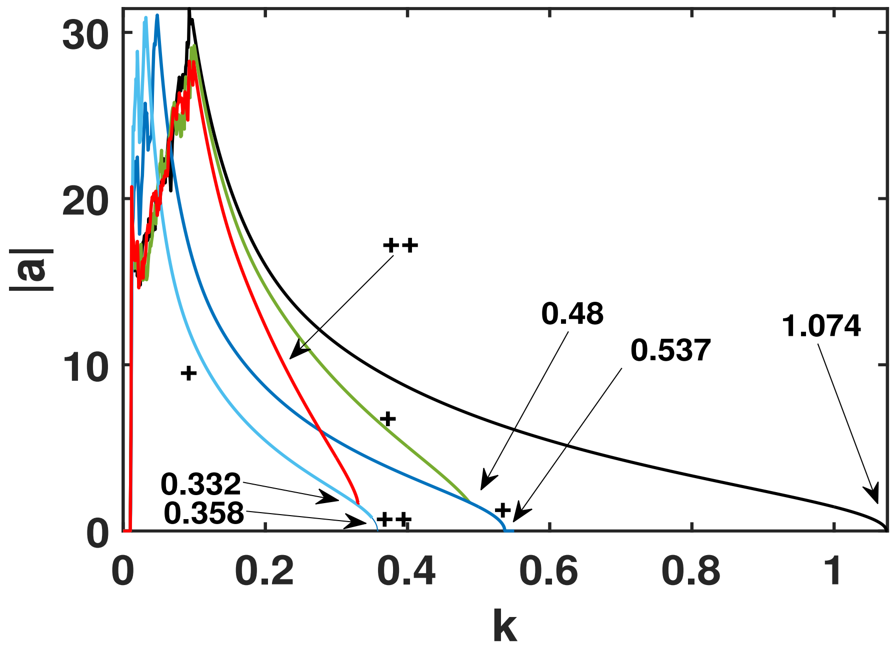

Figure 3.11: Bifurcation diagram for the MMS system (2.3.10) when $\epsilon = 1$. The number of (+) signs indicates the number of positive eigenvalues.

to numerical simulation otherwise it does not give close solution to numerical one for example, figure 3.10(a), when $k = 0.4$ we compare all solutions with numerical and it shows that the stable solution (red solid line) is very close to numerical one (blue dashed line) but unstable solutions do not agree with the numerical one. Similarly when $k = 0.8$, $k = 1.2$ and $k = 1.4$ figure 3.10(b), 3.10(c) and 3.10(d) respectively.

The solution of ODEs (3.3.2) for MMS equation is shown in figure 3.11. In this figure, we can recognize that the solution of the MMS equation is different from the MS solution because there are no crossing points. The bifurcation diagram shows that the black branch is stable for $k > 0.1$ and the dark blue branch is stable with $0.048 < k < 0.48$ otherwise all branches are unstable. We put + on the unstable branches as a sign of the number of positive eigenvalues. All solutions for small k give fluctuated solutions because there are many branches of solutions then the branch that we are finding is jumping from one solution to another. Furthermore, the Fourier series solution of the MMS equation which is corresponding to the black branch gives a very good approximation to the numerical solution.

3.4 Approximate analytical solutions by using complex Fourier series

So far in this chapter, the real Fourier series is used to solve the nonlocal equations. However, this is not the most convenient way to find the travelling wave solution. In this section the complex Fourier series is used to solve all three nonlocal systems (2.3.1), (2.3.8) and (2.3.10) with different values of ϵ. The formula for the complex Fourier series can be written as

$$u = \sum_{n=-\infty}^{\infty} a_n(t)\phi_n(x), \tag{3.4.1}$$

where $\phi_n(x) = e^{inkx}$, k is wavenumber, $a_n(t)$ are complex valued coefficients and $a_n^* = a_{-n}$ because u should be real where $*$ denotes the complex conjugate. By substituting (3.4.1) in the nonlocal-KS equation (2.3.1), we get a system of ODEs

$$a_n^{'} = A_n a_n + \frac{1}{2}\sum_{m=-\infty}^{\infty} m(n-m)a_m a_{n-m}. \tag{3.4.2}$$

This system of ODEs is suitable to be used for all types of equations that have the same nonlinear term as the ones in nonlocal-KS equation and different linear term. Thus we can consider the above system of ODEs as a general model system for all three nonlocal systems (2.3.1), (2.3.8) and (2.3.10) where $A_n = n^2(1-n^2k^2) + \frac{n\epsilon\pi}{|k|}$, $A_n = -n^2 + \frac{n\pi}{|k|}$ and $A_n = -n^2 + \frac{n\epsilon\pi e^{-n|k|}}{|k|}$ respectively.

For our future convenience, we display the general system of ODEs obtained by truncating at $N = 4$

$$a_0^{'} = -|a_1|^2 - 4|a_2|^2 - 9|a_3|^2 - 16|a_4|^2 \tag{3.4.3}$$

$$a_1^{'} = A_1 a_1 - 2a_1^* a_2 - 6a_2^* a_3 - 12a_3^* a_4 \tag{3.4.4}$$

$$a_2^{'} = A_2 a_2 + \frac{1}{2}a_1^2 - 3a_1^* a_3 - 8a_2^* a_4 \tag{3.4.5}$$

$$a_3^{'} = A_3 a_3 + 2a_1 a_2 - 4a_1^* a_4 \tag{3.4.6}$$

$$a_4^{'} = A_4 a_4 + 2a_2^2 + 3a_1 a_3. \tag{3.4.7}$$

We reduce the above ODE system by center-unstable manifold by considering $a_1, a_2 = O(\delta)$ and $a_3, a_4 = O(\delta^2)$ where $\delta \ll 1$ and $a_l = h_l(a_1, a_1^*, a_2, a_2^*)$ where $(l = 3, 4, 5, ...)$. We only need to compute the terms of two of these function $(l = 3, 4)$. Due to the fact that we want a reduced approximation of the above system and truncated to third order, we can write a_3 as a Taylor series approximation to this manifold which is truncated to second order and includes just an $a_1 a_2$ term

$$a_3 = h_3 = c_1 a_1 a_2 + O(\delta^3), \tag{3.4.8}$$

then from (3.4.6) and (3.4.8) we can write $a_3^{'}$ as

$$a_3^{'} = A_3 c_1 a_1 a_2 + 2a_1 a_2 + O(\delta^3). \tag{3.4.9}$$

On the other hand, we can write $a_3^{'}$ from (3.4.8) as

$$a_3^{'} = \frac{\partial h_3}{\partial a_1} a_1^{'} + \frac{\partial h_3}{\partial a_1^*} (a_1^*)^{'} + \frac{\partial h_3}{\partial a_2} a_2^{'} + \frac{\partial h_3}{\partial a_2^*} (a_2^*)^{'}, \tag{3.4.10}$$

then we get

$$a_3^{'} = A_1 c_1 a_1 a_2 + A_2 c_1 a_1 a_2 + O(\delta^3). \tag{3.4.11}$$

Consequently, by comparing (3.4.9) and (3.4.11) we get the value of c_1 which is

$$c_1 = \frac{2}{A_1 + A_2 - A_3}.$$

Following the same method, when we compute a_4 by Taylor series which is truncated by second-order and includes just an a_2^2 term

$$a_4 = h_4 = c_2 a_2^2 + O(\delta^3), \tag{3.4.12}$$

then if we substitute (3.4.12) in (3.4.7), $a_4^{'}$ is

$$a_4^{'} = A_4 c_2 a_2^2 + 2a_2^2 + O(\delta^3). \tag{3.4.13}$$

Like $a_3^{'}$ we can get the value of $a_4^{'}$ from (3.4.12)

$$a_4^{'} = \frac{\partial h_4}{\partial a_1} a_1^{'} + \frac{\partial h_4}{\partial a_1^*}(a_1^*)^{'} + \frac{\partial h_4}{\partial a_2} a_2^{'} + \frac{\partial h_4}{\partial a_2^*}(a_2^*)^{'}, \tag{3.4.14}$$

then after simplification, we get

$$a_4^{'} = 2A_2 c_2 a_2^2 + O(\delta^3). \tag{3.4.15}$$

Thus from (3.4.13) and (3.4.15) we get the value of c_2 which is

$$c_2 = \frac{-2}{A_4 - 2A_2}.$$

Finally, we substitute the value of h_3 and h_4 of (3.4.8) and (3.4.12) into equations (3.4.4) and (3.4.5) to obtain the reduced system

$$a_1^{'} = A_1 a_1 - 2a_1^* a_2 - 6c_1 a_1 a_2 a_2^* + O(\delta^4) \tag{3.4.16}$$

$$a_2^{'} = A_2 a_2 + \frac{1}{2} a_1^2 - 3a_1^* a_1 a_2 - 8c_2 a_2^* a_2^2 + O(\delta^4). \tag{3.4.17}$$

For solving this reduced system we write it in polar form by letting $a_1 = r_1 e^{i\theta_1}$ and $a_2 = r_2 e^{i\theta_2}$. Thus we can write $a_1^{'}$ and $a_2^{'}$ as

$$a_1^{'} = r_1^{'} e^{i\theta_1} + ir_1\theta_1^{'} e^{i\theta_1} \tag{3.4.18}$$

$$a_2^{'} = r_2^{'} e^{i\theta_2} + ir_2\theta_2^{'} e^{i\theta_2}. \tag{3.4.19}$$

However to write $a_1^{'}$ and $a_2^{'}$ from the above-reduced system by polar form, we substitute the value of a_1, a_2 and their complex conjugates into the reduced system. Then we get

$$a_1^{'} = A_1 r_1 e^{i\theta_1} - 2r_1 r_2 e^{-i\theta_1} e^{i\theta_2} - 6c_1 r_1 r_2^2 e^{i\theta_1} \tag{3.4.20}$$

$$a_2^{'} = A_2 r_2 e^{i\theta_2} + \frac{1}{2} r_1^2 e^{2i\theta_1} - 3c_1 r_1^2 r_2 e^{i\theta_2} - 8c_2 r_2^3 e^{i\theta_2}, \tag{3.4.21}$$

where the terms omitted are of $O(\delta^4)$. As a result by comparing (3.4.18) and (3.4.19) with (3.4.20) and (3.4.21) respectively, and separating real and complex values. We get the system of ODEs

$$r_1^{'} = A_1 r_1 - 6c_1 r_1 r_2^2 - 2r_1 r_2 \cos(\phi) \tag{3.4.22}$$

$$\theta_1^{'} = -2r_2 \sin(\phi) \tag{3.4.23}$$

$$r_2^{'} = A_2 r_2 - 3c_1 r_1^2 r_2 - 8c_2 r_2^3 + \frac{1}{2} r_1^2 \cos(\phi) \tag{3.4.24}$$

$$\theta_2^{'} = -\frac{r_1^2}{2r_2} \sin(\phi) \tag{3.4.25}$$

$$\phi^{'} = \left(-\frac{r_1^2}{2r_2} + 4r_2\right) \sin(\phi), \tag{3.4.26}$$

where $\phi = \theta_2 - 2\theta_1$.

Hence we have a reduced system of three equations (3.4.22), (3.4.24) and (3.4.26) instead of two complex equations (four real equations). This three equations system is solved by finding fixed points. Then we get three different solutions.

For the first solution, from equation (3.4.26) we get $\sin(\phi) = 0$ which leads to $\phi = 0$ or $\phi = \pi$. If $\phi = 0$ then we can write r_1 as

$$r_1^2 = \frac{A_2 r_2 - 8c_2 r_2^3}{3c_1 r_2 - \frac{1}{2}}, \tag{3.4.27}$$

where r_2 can be written as

$$r_2^2 + \frac{r_2}{3c_1} - \frac{A_1}{6c_1} = 0. \quad (3.4.28)$$

However in the case $\phi = \pi$, r_1 and r_2 can be written as follows

$$r_1^2 = \frac{A_2 r_2 - 8c_2 r_2^3}{3c_1 r_2 + \frac{1}{2}} \quad (3.4.29)$$

$$r_2^2 - \frac{r_2}{3c_1} - \frac{A_1}{6c_1} = 0. \quad (3.4.30)$$

The above solution is a steady state solution which has two cases when $\phi = 0$ and $\phi = \pi$ and we referred it as 1-mode steady state solution.

The second solution can be presented when $-\frac{r_1^2}{2r_2} + 4r_2 = 0$ ($\sin\phi$ is not 0). As a result $r_1^2 = 8r_2^2$. After getting r_1 as a function of r_2 and doing some simple calculation on equations (3.4.22) and (3.4.24), we get the value of r_2 and ϕ which are shown below

$$r_2^2 = \frac{2A_1 + A_2}{36c_1 + 8c_2} \quad (3.4.31)$$

$$\phi = \cos^{-1}\left(\frac{A_1 - 6c_1 r_2^2}{2r_2}\right). \quad (3.4.32)$$

In this case ϕ is constant, so θ_1' and θ_2' are constants. Thus we can write θ_1 and θ_2 as a function of ct where c is constant. Then this case is noticed as a travelling wave solution.

Besides these two solutions, there is still one case left in which $r_1 = 0$. We consider this case as the third solution. However, when $r_1 = 0$ then from equation (3.4.25), θ_2 is undefined which means ϕ is undefined too. For this reason, we cannot solve the third solution by the polar form system. Thus we should go back to our reduced system. We suppose $a_m = x_m + iy_m$ where $(m = 1, 2)$ and by separating real and imaginary parts we get a system of four ODEs. Solving the four ODEs system and mentioning $a_1 = 0$ leads to $x_1 = y_1 = 0$. By supposing $y_2 = 0$ we get $x_2^2 = \frac{A_2}{8c_2}$. This solution is also a steady state solution and referred as 2-mode steady state.

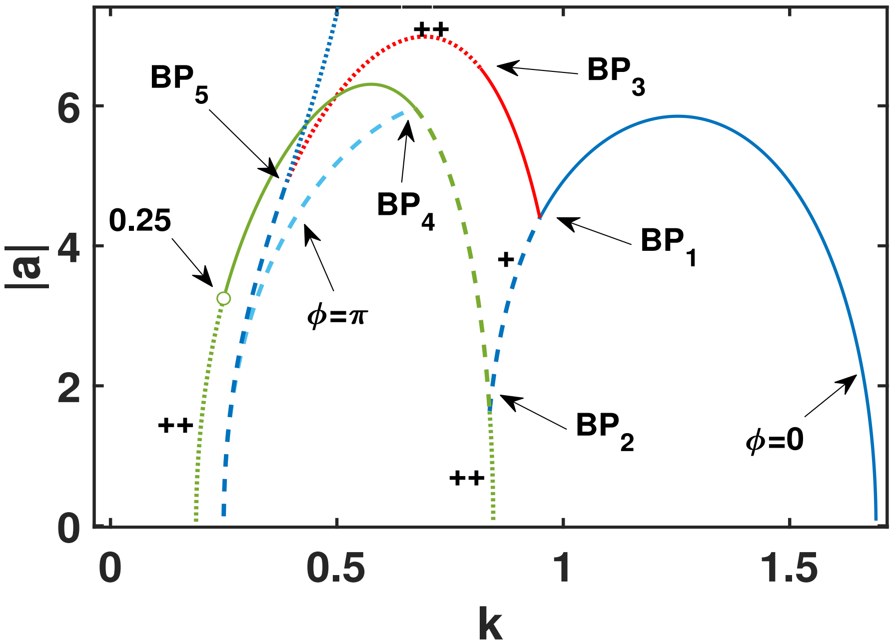

Figure 3.12: Bifurcation diagram for the reduced system of nonlocal-KS system (2.3.1) when $\epsilon = 1$. Stable branches are shown in solid line, dash lines are indicated as the solution that has one positive eigenvalue and dotted lines that has two positive eigenvalues. $BP_1 \approx 0.9482$, $BP_2 \approx 0.8373$, $BP_3 \approx 0.8171$, $BP_4 \approx 0.6722$, $BP_5 \approx 0.3888$. The number of (+) signs indicates the number of positive eigenvalues.

In figure 3.12 we show the bifurcation diagram for the reduced system of the nonlocal-KS equation when $\epsilon = 1$. Note that for $\epsilon = 0$ (which means KS-equation) and $\epsilon = 0.1$ the system gives the same solutions.

The 1-mode steady state solution when $\phi = 0$, which is shown in dark blue line, is born at k_1 where $k_1 \approx 1.6906$ when $A_1 = 0$. This solution is stable until bifurcation point BP1. It loses stability at the same point and bifurcates to two branches. One of them is travelling wave solution and the second one is the extension of the 1-mode steady state solution which is unstable before joins to 2-mode steady state solution at BP2.

On the other hand there is another 1-mode steady state branch when $\phi = 0$ which begins as unstable at k_3 where $k_3 \approx 0.25$ when c_1 goes to infinity. This branch bifurcates to unstable travelling wave at BP5 and goes to infinity as an unstable solution with two positive eigenvalues. The last branch goes to infinity as a result of $3A_1 - A_2 + A_3$ goes to zero which comes from the denominator for the value of r_1^2 tend to zero.

In addition, there is a 1-mode steady state solution when $\phi = \pi$ (light blue) which is unstable with one positive eigenvalue and begin at the same point k_3 and ends when it joins 2-mode steady state solution at BP4.

The second solution which is the travelling wave (red line) is born at BP1 as a stable and subsequently loses stability through a Hopf bifurcation BP3 and continue until joins the 1-mode steady state solution at BP5. This travelling wave solution agrees very well with the numerical simulation where we have found the travelling wave solution in chapter 2 for almost the same period of k $(0.81 < k < 0.94)$, figure 2.8

The third solution which is the 2-mode steady state (Green line) is born as unstable branch, with two positive eigenvalues, at k_2 where $k_2 \approx 0.8453$ when $A_2 = 0$. This branch bifurcates to two branches at BP2; One of them is 1-mode steady state and the second one is 2-mode unstable steady state with one positive eigenvalue. Therefore it gains stability at BP4 and disappears at k_4 where $k_4 \approx 0.189$ when c_2 tends to infinity. This branch loses stability at the point $k = 0.25$ when there is no solution in that point because c_1 goes to infinity, and changes the behaviour of the solution to unstable with two positive eigenvalues as a result of truncation.

Note that we investigate the approximate solution by complex Fourier series for the MS and MMS systems. There is no travelling wave solution for both the MS and MMS solution because the value of $\left(\frac{A_1 - 6c_1 r_2^2}{2r_2}\right)$ from the equation (3.4.32) is always greater than one so there is no cosine inverse of it. In this section, we did not mention the solutions of the MS and MMS equations because we obtained the same solution that we have found in section 3.3.

3.5 Conclusion

To summarize the whole chapter, we have found an approximate analytical solution of all three front equations (2.3.1), (2.3.8) and (2.3.10) by truncated Fourier series. Firstly, we have truncated the real Fourier series with three modes and secondly, with four modes. Then substitute it in the front models gives a system of ODEs. We have solved the system and found the stability, speed of the front, the amplitude of wave and shape of the wave for all three models. We have shown that the results are very close to the numerical simulations. Furthermore, it is observed that for certain values of wavenumber k precisely when the solution is stable, the components of the Fourier series get smaller as the mode number increase, then Fourier series should give an accurate approximation.

For more confirmation, we have found the general form of the ODE system which means we truncated it with N terms. Then we have solved it by 'fsolve' when $N = 100$. We have obtained the bifurcation diagrams of all three equations and compare the solutions with the numerical solution in chapter 2. The stable solutions fit very well with the numerical ones. Furthermore, we have found that the bifurcation points of the MS equation are $\frac{\pi}{3}$, $\frac{\pi}{5}$, $\frac{\pi}{7}$ and so on. We will investigate these bifurcation points in chapter 4.

In the last section, we have found the approximate analytical solution of the nonlocal-KS equation by the truncated complex Fourier series. As a result, we have found the travelling wave solution in a range of k values. This solution agrees with the numerical results found in chapter 2.

Chapter 4

Analytical solution of the MS equation

4.1 Introduction

In the previous chapter we have noticed that the bifurcation diagram of the MS equation, figure 4.1, has bifurcation points at $k = \frac{\pi}{3}, \frac{\pi}{4}, \frac{\pi}{5}$, and so on. Thus might be possible to find a simple analytical solution formula of the MS equation. Thus in this chapter we try to find the analytical solution of the MS equation. In dimensionless form the MS equation is

$$\frac{\partial u(x,t)}{\partial t} = \int_{-\infty}^{\infty} \frac{\frac{\partial u(x^*,t)}{\partial x^*}}{x - x^*} dx^* - \frac{1}{2}\Big(\frac{\partial u(x,t)}{\partial x}\Big)^2 + \frac{\partial^2 u(x,t)}{\partial x^2}. \tag{4.1.1}$$

The Cole-Hopf transformation is used to find the analytical solution of the Burger's equation [26], which is a nonlinear equation and contains the diffusion term. The MS equation is similar to the Burger's with an extra nonlocal term. Thus, we also use the Cole-Hopf transformation method to find the exact analytical solution of the MS equation.

The Cole-Hopf transformation is $u(x,t) = -2\log(f(x)) + st$ where s is the speed of the front. We add the term st to the Cole-Hopf transformation because we are looking for a stationary solution with constant speed. Then we substitute it in the MS equation (4.1.1) which gives

$$s = -2\Big(\frac{f_{xx}f - f_x^2}{f^2}\Big) - \frac{1}{2}\Big(\frac{4f_x^2}{f^2}\Big) + I, \tag{4.1.2}$$

where I is the nonlocal term, $\int_{-\infty}^{\infty} \frac{-2\frac{f_{x^*}}{f}}{x-x^*} dx^*$.

Thus after some simple algebra we can write (4.1.2) as

$$s = -2\Big(\frac{f_{xx}}{f}\Big) + I. \tag{4.1.3}$$

Thual et al. in 1985 [73], found the analytical solution of the derivative form of the MS equation by using a method called pole decomposition. They determined

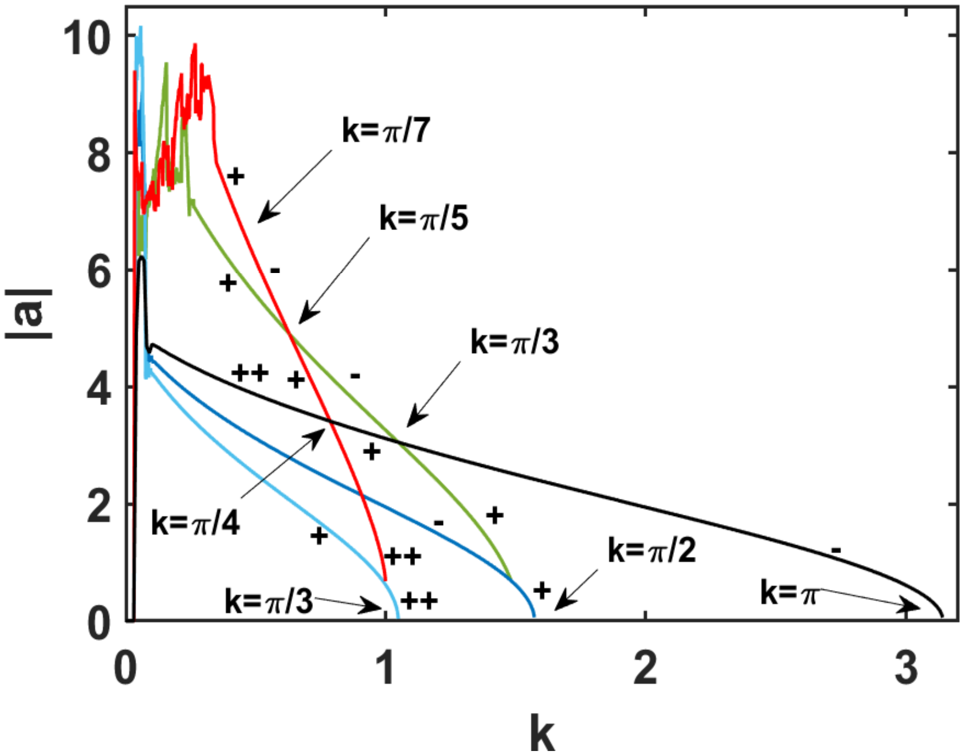

Figure 4.1: Bifurcation diagrams for the MS equation (4.1.1), + indicates number of positive eigenvalues. (This is the same as figure 3.7, repeated here since it will be referred to frequently in this chapter).

one analytical solution of the MS equation in the infinite domain and one analytical solution for the periodic case. We find more than one analytical solution of the MS equation in both infinite and periodic domain. We use different scaling, from them, of the MS equation. They fix the domain size and have a parameter in the equation but we vary the domain size and have no parameter.

The bifurcation diagram of the MS equation motivates us to seek a family of solutions of the MS equation. Although the diagram is for a periodic domain, we expect an infinite number of solutions of the MS equation in the infinite case as well as the periodic one. This is because the infinite case is like the periodic case when the domain $L \to \infty$ (small wavenumber k).

We divide this chapter into three sections to describe more details, which are arranged as follows. In the first section we seek the solution of the MS equation in the infinite case, because the infinite case formula is easier than the periodic formula. In the second section the solution of MS equation in the periodic case is found. A brief conclusion of both cases is given in the last section.

4.2 Infinite case

The Thual et al. solution of the MS equation in the infinite case in our notation and scaling is equivalent to

$$u(x) = -2\log(x^2 + a^2) + st. \tag{4.2.1}$$

Now to find the value of a, we should find $\left(\frac{-2f_{xx}}{f}\right)$ and I then substitute them in (4.1.3). In this case f is equal to $x^2 + a^2$, hence $\frac{-2f_{xx}}{f} = \frac{-4}{x^2+a^2}$.

The nonlocal term I is

$$I = \int_{-\infty}^{\infty} \frac{u_{x^*}}{x - x^*} dx^* = \int_{-\infty}^{\infty} \frac{-2(2x^*)}{({x^*}^2 + a^2)(x - x^*)} dx^*.$$

We use contour integration method to solve this integration

$$I = 4\int_{-\infty}^{\infty} \frac{x^*}{({x^*}^2 + a^2)(x^* - x)} dx^*, \tag{4.2.2}$$

$$= 4\int_{-\infty}^{\infty} \frac{x^*}{(x^* - ia)(x^* + ia)(x^* - x)} dx^*.$$

Now, we have to draw a closed contour to use the residue theorem, so we can use an upper half complex plane, figure 4.2, as a big semicircle contour that have a length πR. The integration along this semicircle vanishes when $R \to \infty$, according to

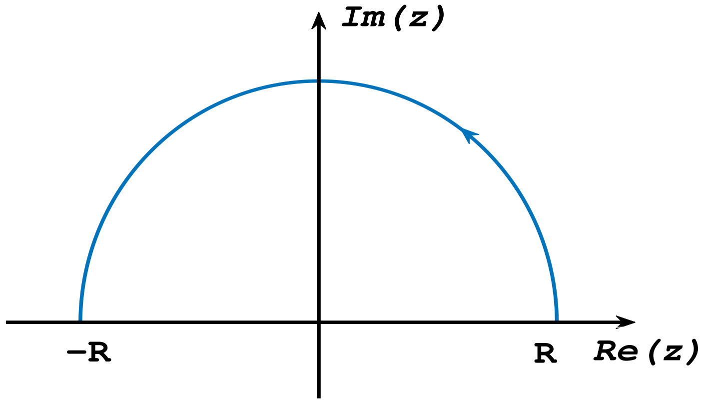

Figure 4.2: The contour used in the integration.

Jordan's Lemma. Hence I is equal to the integral around the closed contour. There is one pole ($x^* = ia$) in the upper half plane, one pole ($x^* = -ia$) not in the upper half plane and one pole ($x^* = x$) on the real axis. Then by the residue theorem and Cauchy principal value we have

$$
\begin{aligned}
I &= 4\Big[2\pi i\Big(\frac{ia}{2ia(ia-x)} + \frac{x}{2(x^2+a^2)}\Big)\Big],\\
&= 4\pi i\Big[\frac{1}{ia-x} * \frac{-ia-x}{-ia-x} + \frac{x}{x^2+a^2}\Big],\\
&= 4\pi i\Big[\frac{-ia-x}{x^2+a^2} + \frac{x}{x^2+a^2}\Big].\\
&= \frac{4\pi a}{x^2+a^2}.
\end{aligned}
$$

Substituting $-2\Big(\frac{f_{xx}}{f}\Big)$ and I in (4.1.3) gives

$$\frac{4\pi a}{x^2+a^2} - \frac{4}{x^2+a^2} = s,$$

by equating the coefficients of x^2 we get

$$a^2 = \frac{1}{\pi^2} \qquad \text{and} \qquad s = 0.$$

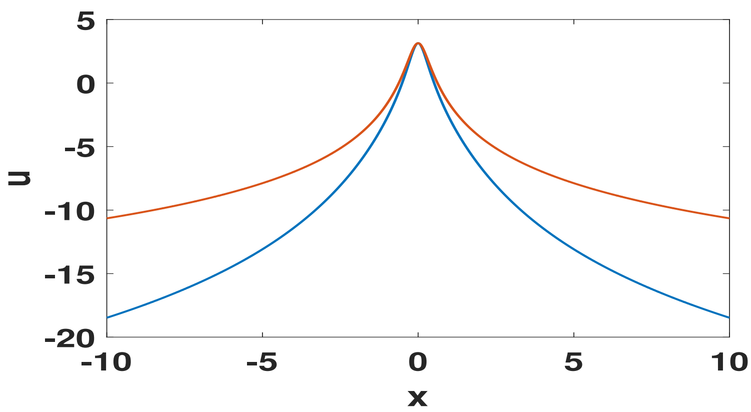

Figure 4.3: The comparison between first (red solid line) and second (blue solid line) solutions of the MS equation in the infinite domain.

Then the solution of the MS equation for infinite domain, figure 4.3, is

$$u(x) = -2\log(x^2 + \frac{1}{\pi^2}). \tag{4.2.3}$$

We call this solution the first solution of the MS equation in the infinite domain.

Furthermore from the bifurcation diagram, figure 4.1, we expect many solutions for small k. Thus we try the second solution in the form

$$u(x) = -2\log(x^2 + a^2) - 2\log(x^2 + b^2) + st, \tag{4.2.4}$$

which is equivalent to

$$u(x) = -2\log(a^2b^2 + (a^2 + b^2)x^2 + x^4) + st, \tag{4.2.5}$$

therefore

$$u_{x^*} = \frac{-4x^*}{(x^{*2} + a^2)} + \frac{-4x^*}{(x^{*2} + b^2)}.$$

Substituting u_{x^*} in the nonlocal term we get

$$I = \int_{-\infty}^{\infty} \frac{\frac{-4x^*}{x^{*2}+a^2} + \frac{-4x^*}{x^{*2}+b^2}}{x - x^*} dx^*.$$

We can write I as an addition of two similar integrations to the first case (4.2.2)

$$I = 4\int_{-\infty}^{\infty} \frac{x^*}{(x^{*2}+a^2)(x^*-x)}dx^* + 4\int_{-\infty}^{\infty} \frac{x^*}{(x^{*2}+b^2)(x^*-x)}dx^*.$$

By the same way as we solved (4.2.2), we solve these two integrations, giving

$$I = \frac{4\pi a}{x^2+a^2} + \frac{4\pi b}{x^2+b^2}.$$

Also we can write (4.2.4) as

$$u(x) = -2\log((x^2+a^2)(x^2+b^2)) + st,$$

then $f = (x^2+a^2)(x^2+b^2)$ so $f_{xx} = 12x^2+2a^2+2b^2$. If both $\frac{-2f_{xx}}{f}$ and I are substituted in (4.1.3), gives

$$\frac{-2(12x^2+2a^2+2b^2)}{(x^2+a^2)(x^2+b^2)} + \frac{4\pi a}{x^2+a^2} + \frac{4\pi b}{x^2+b^2} = s.$$

After some simple algebra and equating the coefficients of x^4, x^2 and the coefficients free of x we get three equations

$$s = 0$$

$$4\pi ab(a+b) - 4(a^2+b^2) = 0$$

$$4\pi(a+b) = 24,$$

and the last two equations lead to

$$a^2+b^2 = \frac{27}{\pi^2} \qquad \textit{and} \qquad a^2b^2 = \frac{81}{4\pi^4}.$$

Then the second solution of the MS equation, figure 4.3, is

$$u(x) = -2\log\left(\frac{81}{4\pi^4} + \frac{27}{\pi^2}x^2 + x^4\right). \tag{4.2.6}$$

By the same token it is noticed that the third solution of the MS equation is

$$u(x) = -2\log(x^2+a^2) - 2\log(x^2+b^2) - 2\log(x^2+c^2) + st, \tag{4.2.7}$$

which is equivalent to

$$u(x) = -2\log\left(a^2b^2c^2 + (a^2b^2 + b^2c^2 + a^2c^2)x^2 + (a^2 + b^2 + c^2)x^4 + x^6\right) + st.$$

Using the same method that we have used for both first and second solutions, we can obtain I and $\frac{-2f_{xx}}{f}$ and substitute them in (4.1.3). As a result we get four equations which are

$$s = 0 \tag{4.2.8}$$

$$4\pi(ab^2c^2 + ba^2c^2 + ca^2b^2) - 4(a^2b^2 + b^2c^2 + a^2c^2) = 0 \tag{4.2.9}$$

$$4\pi(a(b^2 + c^2) + b(a^2 + c^2) + c(a^2 + b^2)) - 24(a^2 + b^2 + c^2) = 0 \tag{4.2.10}$$

$$4\pi(a + b + c) - 60 = 0. \tag{4.2.11}$$

These four equations are too complicated to solve them analytically and find values of a, b and c. We find the values of them numerically which are $a = \frac{0.8187}{\pi}$, $b = \frac{4.254}{\pi}$ and $c = \frac{9.927}{\pi}$.

It appears that we have a family of solutions of the MS equation in the infinite domain. The general n-th solution can be written as

$$u(x) = -2\log\left(c_0 + c_1x^2 + c_2x^4 + c_3x^6 + ... + c_nx^{2n}\right) + st, \tag{4.2.12}$$

where $n = 1, 2, 3, ...$, c_n is constant and $s = 0$ always in the infinite case.

Note that the magnitude of the second derivative at zero of the second solution (4.2.6), $|u_{xx}| = \frac{16}{3}\pi^2$, is greater than the magnitude of the second derivative at zero of the first solution (4.2.3), $|u_{xx}| = 4\pi^2$. This means that the second solution has sharper cusp than the first solution, figure 4.3. In addition the figure shows that the second solution has bigger amplitude than the first one. For large x, n-th solution (4.2.12) of the MS equation is approximately $-2\log(x^{2n}) = -4n\log(x)$ and $u_x \approx \frac{-4n}{x}$, so as n increases the solutions get steeper. It would probably be true to say that the more terms in the solution the sharper the cusp and the bigger the amplitude of the front.

Finally from the general n-th solution (4.2.12) of the MS equation, the first derivative

$$u_x = \frac{-2(2c_1x + 4c_2x^3 + 6c_3x^5 + ... + 2nc_nx^{2n-1})}{(c_0 + c_1x^2 + c_2x^4 + c_3x^6 + ... + c_nx^{2n})},$$

then as $x \to \pm\infty$, $u_x \to 0$. That means all solutions of the MS equation in the infinite case must be unstable, because the solution $u = constant$ is unstable.

4.3 Periodic case

In this section, the solution of the MS equation in the periodic case is discussed. In the infinite case the kernel function is $g(x - x^*) = \frac{1}{x-x^*}$. If we have $u = e^{ikx}$, then the nonlocal term should be

$$\int_{-\infty}^{\infty} \frac{u_{x^*}}{x - x^*} dx^* = \pi|k|e^{ikx}.$$

However the kernel function should be periodic for the periodic case, hence to obtain the kernel function we can write the nonlocal term as

$$\int_0^L h(x - x^*) ike^{ikx^*} dx^* = \pi|k|e^{ikx}, \tag{4.3.1}$$

where $h(x - x^*)$ is the periodic kernel function and $L = \frac{2\pi}{k}$ is the periodic domain.

Letting $y = x - x^*$ then (4.3.1) becomes

$$\int_0^L h(y)(ik)e^{-iky}dy = \pi|k|. \tag{4.3.2}$$

Integration by parts is used to solve this integration by letting $u' = ike^{-iky}$ which leads to $du' = k^2e^{-iky}$ and $dv' = h(y)dy$ which implies that $v' = H(y)$. Due to the periodicity the first term of the integration by parts goes to zero. Thus we can write (4.3.2) as

$$-k^2\int_0^L H(y)e^{-iky}dy = \pi|k|. \tag{4.3.3}$$

Now if $H(y)$ has a Fourier series

$$H(y) = \sum_{n=-\infty}^{\infty} a_n e^{iky} = \sum_{n=-\infty}^{\infty} a_n e^{\frac{2in\pi y}{L}},$$

then

$$a_n = \frac{1}{L}\int_0^L H(y)e^{\frac{-2in\pi y}{L}}dy. \tag{4.3.4}$$

Subsequently from (4.3.4), equation (4.3.3) can be written as $-k^2La_n = \pi|k|$, where k is corresponding to $\frac{2n\pi}{L}$, thus

$$a_n = \begin{cases} \frac{-1}{2n} & k > 0 \\ \frac{1}{2n} & k < 0 \end{cases} \tag{4.3.5}$$

With these coefficients, the Fourier series of $H(y)$ becomes

$$H(y) = -\cos\left(\frac{2\pi y}{L}\right) - \frac{\cos\left(\frac{4\pi y}{L}\right)}{2} - \frac{\cos\left(\frac{6\pi y}{L}\right)}{3} + ... \tag{4.3.6}$$

Now to find $H(y)$ we use the formula (1.441 4) of Gradshteyn and Ryzhik's book [27] which is

$$\sum_{n=1}^{\infty}(-1)^{n-1}\frac{\cos(nx)}{n} = \ln\left(2\cos(\frac{x}{2})\right), \tag{4.3.7}$$

after substituting $x = \frac{2\pi y}{L} - \pi$ in the formula (4.3.7), gives

$$-\cos\left(\frac{2\pi y}{L}\right) - \frac{\cos\left(\frac{4\pi y}{L}\right)}{2} - \frac{\cos\left(\frac{6\pi y}{L}\right)}{3} + ... = \ln\left(2\cos\left(\frac{\pi y}{L} - \frac{\pi}{2}\right)\right). \tag{4.3.8}$$

Thus from (4.3.6) and (4.3.8)

$$H(y) = \ln\left(2\cos(\frac{\pi y}{L} - \frac{\pi}{2})\right).$$

By differentiating it with respect to y and putting $y = x - x^*$, we get the kernel function of the periodic case which is

$$h(x - x^*) = \frac{\pi}{L}\cot\left(\frac{\pi}{L}(x - x^*)\right). \tag{4.3.9}$$

In addition when $L \to \infty$, the periodic kernel function $h(x - x^*) \to \frac{1}{x - x^*}$, matching with the kernel in the infinite case.

The Thual et al. solution for the periodic case in our notation and scaling is

$$u = -2\log(1 + a\cos(kx)) + st. \tag{4.3.10}$$

By the same method as we used in the infinite case we seek a solution in the form of (4.3.10), so we should find $\frac{-2f_{xx}}{f}$ and I then substitute in (4.1.3) to determine the vale of a. In this case $f = 1 + a\cos(kx)$, then $\frac{-2f_{xx}}{f} = \frac{2ak^2\cos(kx)}{1 + a\cos(kx)}$.

The nonlocal term I is

$$I = \int_0^L \frac{-2(-ak)\sin(kx^*)}{1 + a\cos(kx^*)}\frac{\pi}{L}\cot\left(\frac{\pi}{L}(x - x^*)\right)dx^*$$

Then applying the Euler formula, putting $L = \frac{2\pi}{k}$ and after some algebra we get

$$I = -k^2\int_0^{\frac{2\pi}{k}} \frac{(e^{2ikx^*} - 1)(e^{ikx^*} + e^{ikx})}{e^{ikx^*}(e^{ikx^*} - e^{ikx})(e^{2ikx^*} + \frac{2}{a}e^{ikx^*} + 1)}dx^*. \tag{4.3.11}$$

We obtain I by contour integration and Cauchy principal value. By substituting $z = e^{ikx^*} \Rightarrow dx^* = \frac{dz}{ikz}$, I becomes

$$I = \frac{-k}{i} \oint_c \frac{(z^2-1)(z+e^{ikx})}{z(z-e^{ikx})(z^2+\frac{2}{a}z+1)} dz, \tag{4.3.12}$$

where c is the circle $|z| = 1$. There are four simple poles in the integral which are $z = 0$, e^{ikx}, $\frac{-1+\sqrt{1-a^2}}{a}$ and $z = \frac{-1-\sqrt{1-a^2}}{a}$. Only 0, e^{ikx} and $\frac{-1+\sqrt{1-a^2}}{a}$ are inside the contour c. Then using the residue theorem, Cauchy principal value and after some algebra the result of the nonlocal term I is

$$I = -2\pi k\Big(1 - \frac{\sqrt{1-a^2}}{1+a\cos(kx)}\Big). \tag{4.3.13}$$

Consequently by substituting $(\frac{-2f_{xx}}{f})$ and I in (4.1.3) and equating the coefficients of $\cos(kx)$ and the coefficients free of $\cos(kx)$ we get two equations

$$-2\pi k + 2\pi k\sqrt{1-a^2} = s \tag{4.3.14}$$

$$-2\pi ka + 2k^2 a = as. \tag{4.3.15}$$

These two equations give

$$s = 2k(k-\pi) \quad \text{and} \quad a = \pm\sqrt{1 - \frac{k^2}{\pi^2}}.$$

Then, by using these values of s and a in (4.3.10), the solution of the MS equation for the periodic case, corresponding to the black solution in the bifurcation diagram, figure 4.1, is

$$u = -2\log\Big(1 \pm \sqrt{1-\frac{k^2}{\pi^2}}\cos(kx)\Big) + 2k(k-\pi)t. \tag{4.3.16}$$

This solution, shown in figure 4.4 for the case $k = 1$, exists if $k < \pi$ $(L > 2)$.

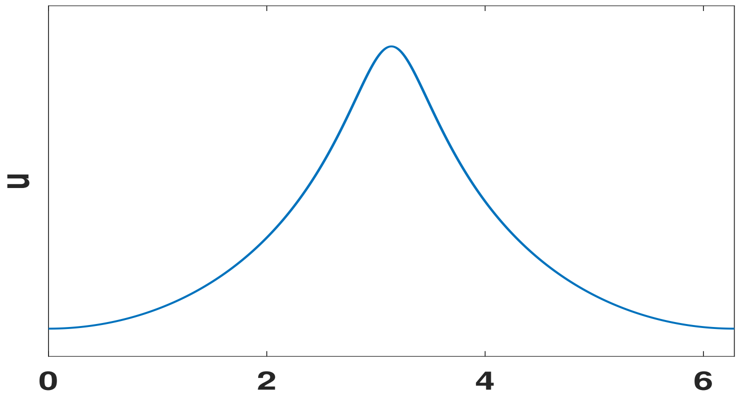

Figure 4.4: The solution of the MS equation, corresponding to the black branch in the bifurcation diagram, figure 4.1, in the periodic domain (4.3.16) when $k = 1$.

Furthermore it is noticed from the numerical solution of the MS equation that the solution shown as the black curve has period $\frac{2\pi}{k}$ and the log of the solution has 1 and $\cos(kx)$ terms. However the dark blue curve has period $\frac{\pi}{k}$ and the solution of it has two copies of the black curve solution which means the solution of the dark blue curve has 1 and $\cos(2kx)$ terms. Whereas the green curve solution has period $\frac{2\pi}{k}$ and it branches from the dark blue solution. Thus we expect that the green solution should include 1, $\cos(kx)$ and $\cos(2kx)$ terms. Hence the expected solution of the green branch will be

$$u = -2\log(1 + A_1\cos(kx) + A_2\cos(2kx)) + st. \tag{4.3.17}$$

Alternatively this equation can be written as

$$u = -2\log\left(1 + \frac{2(a+b)}{2+ab}\cos(kx) + \frac{ab}{2+ab}\cos(2kx)\right) + st, \tag{4.3.18}$$

which is equivalent to

$$u = -2\log\Big((1 + a\cos(kx))(1 + b\cos(kx))\Big) + st. \tag{4.3.19}$$

By the same idea we have used in the infinite case, we can rewrite (4.3.19) as the summation of two logarithms which are similar to the first solution of the periodic case

$$u = -2\log\Big(1 + a\cos(kx)\Big) - 2\log\Big(1 + b\cos(kx)\Big) + st. \tag{4.3.20}$$

In this case it is easy to rely on the first solution and find the value of I, because u is a summation of two logarithms similar to the logarithm in the first solution. Thus we can write I as

$$I = -2\pi k\Big(1 - \frac{\sqrt{1-a^2}}{1 + a\cos(kx)}\Big) - 2\pi k\Big(1 - \frac{\sqrt{1-b^2}}{1 + b\cos(kx)}\Big). \tag{4.3.21}$$

Furthermore from (4.3.18), $f = 1 + \frac{2(a+b)}{2+ab}\cos(kx) + \frac{ab}{2+ab}\cos(2kx)$. Thus

$$\frac{-2f_{xx}}{f} = \frac{2k^2(a+b)\cos(kx) + 4k^2 ab\cos(2kx)}{\frac{2+ab}{2} + (a+b)\cos(kx) + \frac{ab}{2}\cos(2kx)}. \tag{4.3.22}$$

With substituting (4.3.21) and (4.3.22) in (4.1.3) and equating coefficients give three equations which are

$$4k(2k - \pi) = s \tag{4.3.23}$$

$$\sqrt{1-a^2} + \sqrt{1-b^2} = \frac{2k}{\pi}(2 + ab) \tag{4.3.24}$$

$$b\sqrt{1-a^2} + a\sqrt{1-b^2} = \frac{3k}{\pi}(a + b). \tag{4.3.25}$$

Now we want to find $\frac{2(a+b)}{2+ab}$ and $\frac{ab}{2+ab}$ for (4.3.18), let $p = \frac{k}{\pi}$ in the last two equations and solve them for $\sqrt{1-a^2}$ and $\sqrt{1-b^2}$, then they give

$$\sqrt{1-a^2} = \frac{p(a + 2a^2b - 3b)}{a - b} \tag{4.3.26}$$

$$\sqrt{1-b^2} = \frac{p(b + ab^2 - 3a)}{b - a}. \tag{4.3.27}$$

We find p from (4.3.26) and substitute it in (4.3.27). Then by squaring the equation that is found, we get

$$(b^2 - a^2)(9a^2 + 9b^2 - 8a^2b^2 - 2ab - 8) = 0.$$

Then from the last equation we have

$$b = \pm a, \tag{4.3.28}$$

we will explain this case later, or

$$9a^2 + 9b^2 - 8a^2b^2 - 2ab - 8 = 0, \tag{4.3.29}$$

Suppose that $\alpha = ab$ and $\beta = a + b$ then (4.3.29) leads to

$$9\beta^2 = 8\alpha^2 + 20\alpha + 8. \tag{4.3.30}$$

Therefore by subtracting the square of (4.3.27) from the square of (4.3.26) and replacing α and β instead of ab and $a + b$ respectively, we get

$$p^2 = \frac{\beta^2 - 4\alpha}{4(1-\alpha)(2+\alpha)}. \tag{4.3.31}$$

Solving equation (4.3.30) for β^2 and substituting it in (4.3.31), leads to

$$p^2 = \frac{2(1-\alpha)}{9(2+\alpha)}. \tag{4.3.32}$$

Putting back the value of $p = \frac{k}{\pi}$, $\alpha = ab$ in (4.3.32) gives

$$\frac{ab}{2+ab} = \frac{1}{3} - \frac{3k^2}{\pi^2}. \tag{4.3.33}$$

Now consider

$$\frac{9(a+b)^2}{(2+ab)^2} = \frac{9\beta^2}{(2+\alpha)^2}, \tag{4.3.34}$$

from the equation (4.3.30), (4.3.34) leads to

$$\frac{9(a+b)^2}{(2+ab)^2} = \frac{8\alpha^2 + 20\alpha + 8}{(2+\alpha)^2}. \tag{4.3.35}$$

Also solving (4.3.32) for α gives

$$\alpha = \frac{2(1-9p^2)}{2+9p^2}. \tag{4.3.36}$$

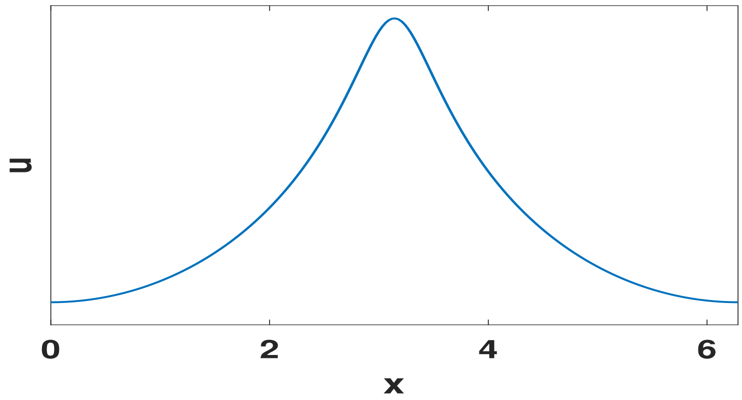

Figure 4.5: The solution of the MS equation, corresponding to the green branch in the bifurcation diagram, figure 4.1, in the periodic domain (4.3.39) when $k = 1$.

Then from (4.3.36) we can write (4.3.35) as

$$\frac{9(a+b)^2}{(2+ab)^2} = \frac{72(2-9p^2)/(2+9p^2)}{36/(2+9p^2)}. \tag{4.3.37}$$

After some algebra (4.3.37) leads to

$$\frac{2(a+b)}{2+ab} = \pm\sqrt{\frac{16}{9} - \frac{8k^2}{\pi^2}}. \tag{4.3.38}$$

Finally, by using equations (4.3.23), (4.3.33) and (4.3.38) in (4.3.18), we can say that the solution of the MS equation in the periodic case, figure 4.5, which is corresponding to the green solution in the bifurcation diagram, figure 4.1, is

$$u = -2\log\left(1 \pm \sqrt{\frac{16}{9} - \frac{8k^2}{\pi^2}}\cos(kx) + \left(\frac{1}{3} - \frac{3k^2}{\pi^2}\right)\cos(2kx)\right) + 4k(2k-\pi)t. \tag{4.3.39}$$

The comparison between both solutions of the MS equation (4.3.16) and (4.3.39), which are corresponding to black and green curves in bifurcation diagram respectively, is shown in the figure 4.6. It is noticed in the first figure 4.6(a) that the solution (4.3.16) has sharper cusp and bigger amplitude than the solution (4.3.39). However in the second figure 4.6(b) is exhibited that the solution (4.3.39) has sharper cusp

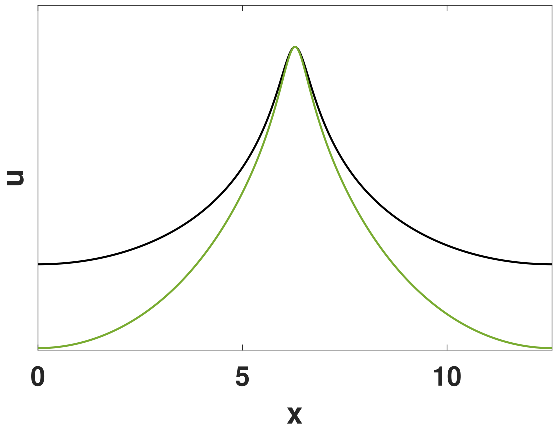

(a) When $k = 0.5$.

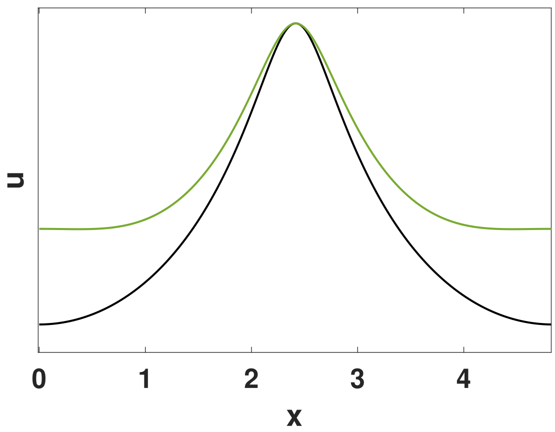

(b) When $k = 1.3$.

Figure 4.6: The comparison between (4.3.16), black solid line, and (4.3.39), green solid line, solutions of the MS equation in the periodic domain.

and bigger amplitude than the solution (4.3.16). Hence it suggests that when $k > \frac{\pi}{3}$ the solution which corresponds to the black curve in the bifurcation diagram has bigger amplitude and sharper cusp than the solution that corresponds to the green curve, while it is vice versa when $k < \frac{\pi}{3}$.

Moreover when we substitute $\frac{\pi}{3}$ in both solutions (4.3.16) and (4.3.39), they both give the same result which is

$$u = -2\log\left(1 + \frac{2\sqrt{2}}{3}\cos\left(\frac{\pi}{3}x\right)\right) - \frac{4\pi^2}{9}t,$$

which means it agrees with the bifurcation diagram, because $k = \frac{\pi}{3}$ is the transcritical bifurcation between both black and green solutions.

Let us go back to the equation (4.3.28) when $b = \pm a$. If $b = -a$ then it satisfies the equation (4.3.25) and the equation (4.3.24) gives

$$2\sqrt{1-a^2} = \frac{2k}{\pi}(2-a^2).$$

Again we have to find $\frac{2(a+b)}{2+ab}$ and $\frac{ab}{2+ab}$ and substitute them in (4.3.18). The first one is zero when $b = -a$ and the second one is $\frac{-a^2}{2-a^2}$. The last equation can be written

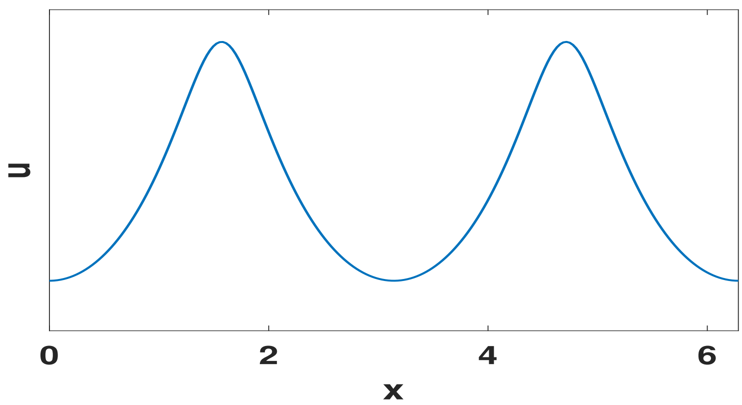

Figure 4.7: The solution (4.3.41) of the MS equation in the periodic domain that corresponds to the dark blue curve in figure 4.1.

as

$$\frac{1-a^2}{(2-a^2)^2} = \frac{k^2}{\pi^2},$$

it follows

$$\frac{4(1-a^2)}{4(2-a^2)^2} + \frac{a^4}{4(2-a^2)^2} - \frac{a^4}{4(2-a^2)^2} = \frac{k^2}{\pi^2}.$$

After some algebra we get

$$\frac{a^2}{2-a^2} = \pm\sqrt{1-\frac{4k^2}{\pi^2}}. \tag{4.3.40}$$

With (4.3.40) and (4.3.23), (4.3.18) gives

$$u = -2\log\left(1 \pm \sqrt{1-\frac{4k^2}{\pi^2}}\cos(2kx)\right) + 4k(2k-\pi)t. \tag{4.3.41}$$

This solution, figure 4.7, corresponds to the dark blue curve solution in the bifurcation diagram. It is same as the solution (4.3.16), which corresponds to black branch, with the period $\frac{L}{2}$.

However if $b = a$ equations (4.3.24) and (4.3.25) give

$$\sqrt{1-a^2} = \frac{k}{\pi}(2+a^2) \tag{4.3.42}$$

$$\sqrt{1-a^2} = \frac{3k}{\pi}. \tag{4.3.43}$$

Substituting (4.3.43) in (4.3.42) leads to

$$\frac{3k}{\pi} = \frac{k}{\pi}(2+a^2),$$

which gives $a = \pm 1$ and then if we put the value of a in any of two equations (4.3.42) or (4.3.43) implies to $k = 0$ which gives us the trivial solution, $u = constant$.

Now we have found both solutions (4.3.39) and (4.3.41) which correspond to the green and dark blue branches in the bifurcation diagram respectively. However there is a bifurcation point between these two solutions, we can find it by equating these two solutions. By equating (4.3.39) and (4.3.41) we get

$$\sqrt{\frac{16}{9} - \frac{8k^2}{\pi^2}} = 0,$$

this leads to $k = \frac{\sqrt{2}\pi}{3}$ which is pitchfork bifurcation point between the green and dark blue branches in the bifurcation diagram, figure 4.1. This also confirms that the green curve only exists for $k \leq \frac{\sqrt{2}\pi}{3}$.

Referring to the bifurcation diagram, we expect the solution corresponding to the red curve to include 1, $\cos(kx)$, $\cos(2kx)$ and $\cos(3kx)$ terms. This is because the red curve branches from the light blue curve and the latter, which has $\frac{2\pi}{3k}$ period, is three copies of the black branch solution. Then the solution is expected as

$$u = -2\log\Big(1 + A_1\cos(kx) + A_2\cos(2kx) + A_3\cos(3kx)\Big) + st, \tag{4.3.44}$$

which is equivalent to

$$u = -2\log\Big((1+a\cos(kx))(1+b\cos(kx))(1+c\cos(kx))\Big) + st. \tag{4.3.45}$$

Following the same method as for the last solution, this solution can be written as a summation of three logarithms and we can get the nonlocal term I. From (4.3.45), $f = (1 + a\cos(kx))(1 + b\cos(kx))(1 + c\cos(kx))$. Then by obtaining $\frac{-2f_{xx}}{f}$ and I and substituting them in (4.1.3) we get four equations

$$6k(3k - \pi) = s$$

$$\sqrt{1-a^2} + \sqrt{1-b^2} + \sqrt{1-c^2} = \frac{k}{\pi}(2(ab + ac + bc) + 9)$$

$$(b + c)\sqrt{1-a^2} + (a + c)\sqrt{1-b^2} + (a + b)\sqrt{1-c^2} = \frac{2k}{\pi}(4(a + b + c) + 3abc)$$

$$bc\sqrt{1-a^2} + ac\sqrt{1-b^2} + ab\sqrt{1-c^2} = \frac{5k}{\pi}(ab + ab + bc).$$

The last three equations are complicated to solve, but at least we know the value of s.

The whole idea suggests that we can find the n-th solution of the MS equation in the periodic case as well which is

$$u = -2\log\Big(1 + A_1\cos(kx) + A_2\cos(2kx) + A_3\cos(3kx) + ... + A_n\cos(nkx)\Big) + st,$$

or alternatively can be written as

$$u = -2\log\Big((1 + a_1\cos(kx))(1 + a_2\cos(kx))(1 + a_3\cos(kx))...(1 + a_n\cos(kx))\Big) + st.$$

In this case $f = a_1a_2...a_n\cos^n(kx) + T$, where T represents all terms that have $\cos(kx)$ with the power less than n. Thus

$$f_{xx} = -n^2k^2a_1a_2...a_n\cos^n(kx) + T.$$

Again by the same idea we can write u as a summation of n logarithms and find I which becomes

$$I = -2\pi k\Big(1 - \frac{\sqrt{1-a_1^2}}{1 + a_1\cos(kx)} + 1 - \frac{\sqrt{1-a_2^2}}{1 + a_2\cos(kx)} + ... + 1 - \frac{\sqrt{1-a_n^2}}{1 + a_n\cos(kx)}\Big)$$

$$= \frac{-2\pi kna_1a_2...a_n\cos^n(kx)+T}{f}.$$

Then after substituting $\frac{-2f_{xx}}{f}$ and I in (4.1.3) gives

$$\frac{2n^2k^2a_1a_2...a_n\cos^n(kx)+T}{f}+\frac{-2\pi kna_1a_2...a_n\cos^n(kx)+T}{f}=s,$$

from the last equation we get n equations, and one of them is

$$s=2nk(nk-\pi),$$

which means we have the formula for the speed of all solutions in the periodic domain.

Finally, note that in the periodic case if $k \to 0$, this means for large L, we can get the same solutions as for infinite case. All solutions are in the form $u=-2\log(f(x))+st$ in the periodic domain. For the solution (4.3.16), f is

$$f=1\pm\sqrt{1-\frac{k^2}{\pi^2}}\cos(kx),$$

which for small k, leads to

$$f=1\pm(1-\frac{k^2}{2\pi^2}+O(k^4))(1-\frac{k^2x^2}{2}+O(k^4)).$$

It follows that

$$f=1\pm(1-\frac{k^2}{2\pi^2}-\frac{k^2x^2}{2})+O(k^4),$$

then f is approximately

$$f=\begin{cases}\frac{1}{2}k^2(x^2+\frac{1}{\pi^2}) & for-case\\ 2-\frac{1}{2}k^2(x^2+\frac{1}{\pi^2}) & for+case\end{cases} \tag{4.3.46}$$

Furthermore $s \to 0$ as $k \to 0$. Then the solution (4.3.16), when $k \to 0$, can be written as

$$u=-2\log(\frac{1}{2}k^2(x^2+\frac{1}{\pi^2})),$$

which is equivalent to the first solution (4.2.3) in the infinite case.

Similarly for the solution (4.3.39), f is

$$f = 1 \pm \sqrt{\frac{16}{9} - \frac{8k^2}{\pi^2}} \cos(kx) + (\frac{1}{3} - \frac{3k^2}{\pi^2}) \cos(2kx),$$

which for small k, leads to

$$\begin{aligned} f = 1 \pm \frac{4}{3}\Big(1 - \frac{9k^2}{4\pi^2} - \frac{81k^4}{32\pi^4} + O(k^6)\Big)\Big(1 - \frac{k^2x^2}{2} + \frac{k^4x^4}{24} + O(k^6)\Big) \\ + \Big(\frac{1}{3} - \frac{3k^2}{\pi^2}\Big)\Big(1 - 2k^2x^2 + \frac{2}{3}k^4x^4 + O(k^6)\Big). \end{aligned} \tag{4.3.47}$$

Thus after some algebra we get

$$f = \begin{cases} \frac{k^4}{6}\Big(\frac{81}{4\pi^4} + \frac{27}{\pi^2}x^2 + x^4\Big) & for - case \\ \frac{8}{3} - \frac{6k^2}{\pi^2} - \frac{27k^4}{8\pi^4} - \Big(\frac{4k^2}{3} - \frac{15k^4}{2\pi^2}\Big)x^2 + \frac{5k^4}{18}x^4 & for + case \end{cases} \tag{4.3.48}$$

Therefore the solution (4.3.39), when $k \to 0$, is

$$u = -2\log\Big(\frac{k^4}{6}\Big(\frac{81}{4\pi^4} + \frac{27}{\pi^2}x^2 + x^4\Big)\Big),$$

that is equivalent to the second solution (4.2.6) in the infinite case.

4.4 Conclusion

This chapter has been concerned with finding a family of analytical solutions of the MS equation (4.1.1). Numerical solution of the MS equation motivated us to look for the analytical solution of it, because the bifurcation diagram, figure 4.1, of the MS equation contains a group of bifurcation points all related to π. This suggests that it might be worth trying to find a simple analytical solution formula for the MS equation.

In the first section in this chapter, we have found a family of infinite number of analytical solutions of the MS equation in the infinite domain. All these solutions are stationary and have similar structure with single peak. In addition all these solutions are unstable. Also we have found that the speed s is always zero in this case. In addition the general formula for the family of analytical solution for the MS equation has been obtained.

The periodic domain case has been studied in the second section. We have got a family of infinite number of solutions for the MS equation. We have explicitly found the first two analytical solutions and the bifurcation points for the MS equation. In addition we have found the general formula for all solutions. Furthermore the formula of the speed for all solutions has been obtained. Finally we have confirmed that in the periodic case when $k \to 0$ the formulas of the solutions are equivalent to the solutions in the infinite case.

Chapter 5

Solutions of all three nonlocal-KS, MS and MMS systems in two dimensions

5.1 Introduction

So far in this work, we have found the numerical solution of all three nonlocal-KS (2.3.1), MS (2.3.8) and MMS (2.3.10) systems in one dimension. Then we have found the analytical solution of the MS equation in one dimension. This motivates us to seek the numerical solution of all three equations and the analytical solution of the MS equation in two dimensions.

The outline of this chapter is as follows; Section 5.2 presents the numerical solution of the MS equation in two dimensions and then discusses the results. In addition, we calculate the speed of the front numerically. Section 5.3 concentrates on finding the analytical solution of the MS equation in two dimensions. In section 5.4 we confirm, by weakly nonlinear analysis, that the behaviour of the front dynamics for the MS equation in one and two dimensions are similar. Section 5.5 displays the numerical solution of the nonlocal-KS and MMS systems in two dimensions. A brief conclusion of the chapter is given in section 5.6.

5.2 Numerical solution of the MS equation in two dimensions

Sivashinsky [69] has written the MS equation in two dimensions, which in our notation and scaling can be written as

$$\frac{\partial u(x,y,t)}{\partial t} = \frac{\partial^2 u}{\partial x^2} + \frac{\partial^2 u}{\partial y^2} - \frac{1}{2}\Big(\big(\frac{\partial u}{\partial x}\big)^2 + \big(\frac{\partial u}{\partial y}\big)^2\Big) + I, \tag{5.2.1}$$

where I is the nonlocal term. To evaluate I we take the two dimensions Fourier transformation of u, then multiply by the magnitude of the wavevector $\pi|\mathbf{k}|$, then take the inverse Fourier transformation. Thus I can be written as

$$I = \frac{1}{4\pi} \int_{-\infty}^{\infty} \int_{-\infty}^{\infty} |\mathbf{k}| e^{i\mathbf{k}.(\mathbf{x}-\mathbf{x}^*)} u(\mathbf{x}^*, t) d\mathbf{k} d\mathbf{x}^*.$$

In the next few sections we describe the method that has been used to solve the MS equation in two dimensions numerically. Moreover, we discuss the front propagation which we get from the numerical simulations. Finally, we find the speed of the front numerically.

5.2.1 Numerical method

As in the one-dimensional numerical solution, section 2.4.1, we consider the two-dimensional MS equation discretized in space using the Fourier spectral and discretized in time with the exponential time differencing (ETD) method with time step size 0.002. We choose this time step size to balance between time and accuracy. In the simulation, we use periodic boundary condition and small random initial condition.

In two dimensions we have two cases about wavenumbers, the first one is when $k_x = k_y$ where k_x and k_y are wavenumbers along the x and y-axis respectively. The second one is when fixing one of them and varying the other. Thus in both cases, for the stable solutions, we have found the same bifurcation diagram as the one-dimensional bifurcation diagram 4.1. This means that we have the same bifurcation points like the one-dimensional case π, $\frac{\pi}{3}$, $\frac{\pi}{5}$, $\frac{\pi}{7}$ and so on. In other words, we have the bifurcation points in the domain size which are 2, 6, 10, 14 and so on. Thus we can classify the solution of the MS equation to some states and take an example of each case.

In the next subsection, we show the results that we have found from the numerical simulations of a band of examples. We have chosen a variety of examples from a small to a large domain.

5.2.2 Numerical results

First, we find the numerical solution of the MS equation in two dimensions that is corresponding to the black curve in the bifurcation diagram 4.1. This means we have L_x and L_y in the interval $[2,6]$ (or k_x and k_y are in the interval $[\frac{\pi}{3},\pi]$) and the solution is stable, where L_x and L_y are the domain size along x and y-axis respectively. We take a specific case as an example when $L_x = L_y = 4$. This numerical experiment in two dimensions shows that the dynamics of the front that arose through initial disturbances has a considerable number of peaks and troughs on the front. The fast decaying of the number of peaks and troughs is observed near the initial time. The peaks and troughs tend to merge and form bigger cells when time progresses. The simulation of the front propagation is shown in a sequence of figures 5.1. The visual observations suggest that the dynamics of the front coarsens quickly from a huge number of peaks, figure 5.2, and troughs, figure 5.3, until it reaches a steady state solution with one peak and one trough figure 5.1(d).

In the one-dimensional numerical simulation, the number of peaks and troughs are the same, while in two dimensions they are different. In the above case when L_x and L_y in the interval $[2,6]$, the number of peaks and troughs are not equal and usually the coarsening in the number of troughs decaying is faster than the number of peaks decaying.

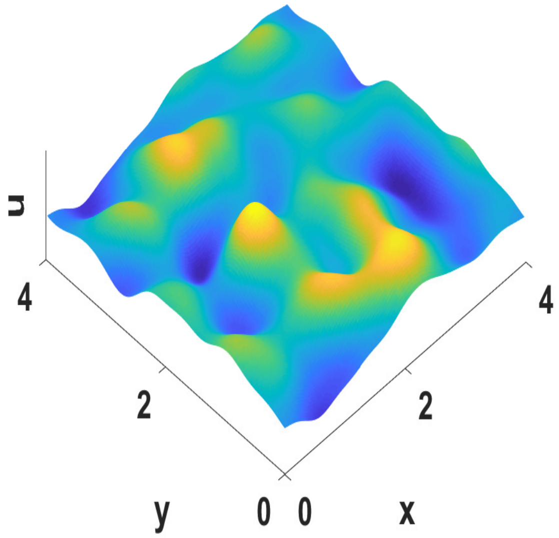

(a) $t = 0.04$.

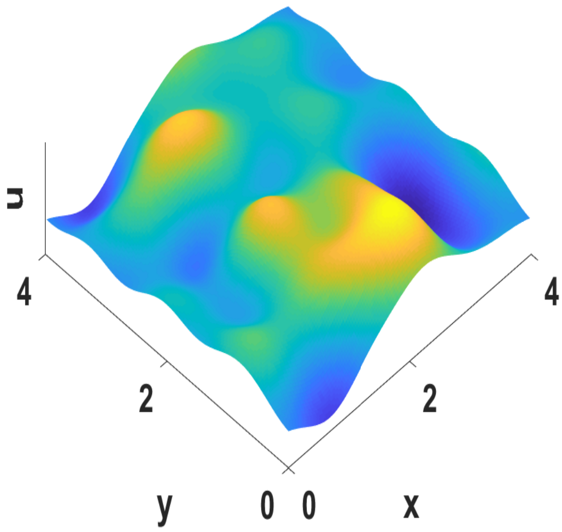

(b) $t = 0.12$.

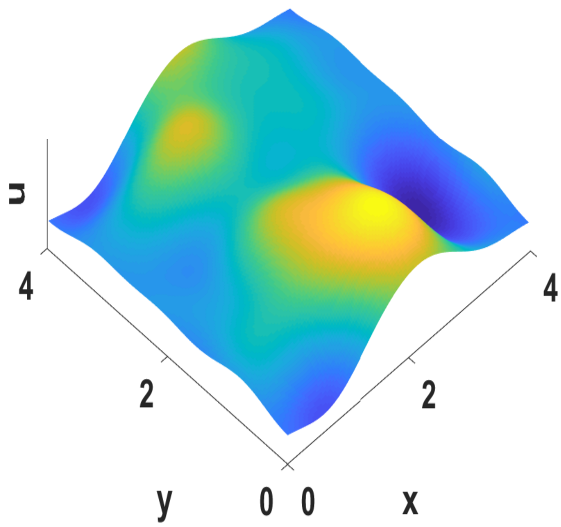

(c) $t = 0.2$.

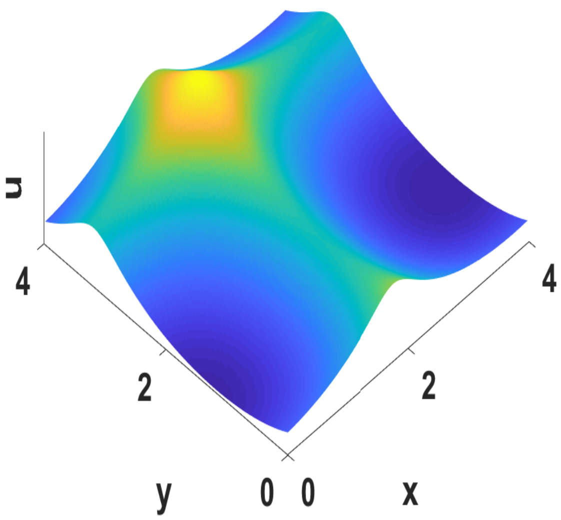

(d) $t = 10$.

Figure 5.1: Snapshots of development of the front dynamics based on the MS equation (5.2.1) when $L_x = L_y = 4$.

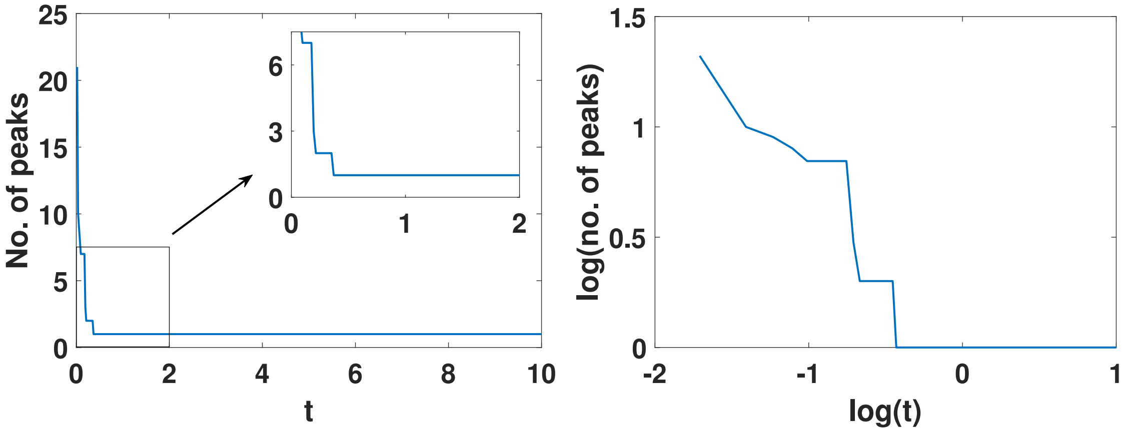

(a) (b)

Figure 5.2: Number of ***peaks*** on the front against the time t for the MS equation (5.2.1) when $L_x = L_y = 4$, (a) and (b) are the same data but (b) has log_{10} scales.

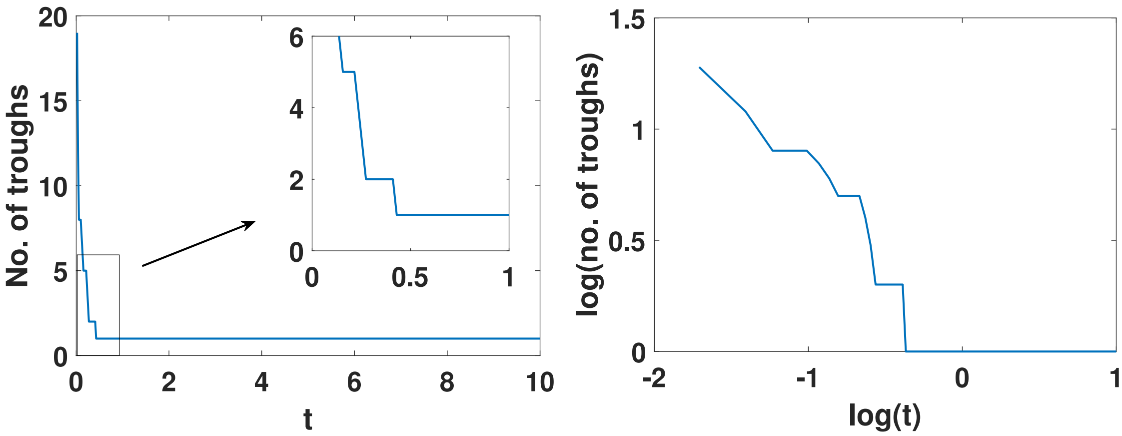

(a) (b)

Figure 5.3: Number of ***troughs*** on the front against the time t for the MS equation (5.2.1) when $L_x = L_y = 4$, (a) and (b) are the same data but (b) has log_{10} scales.

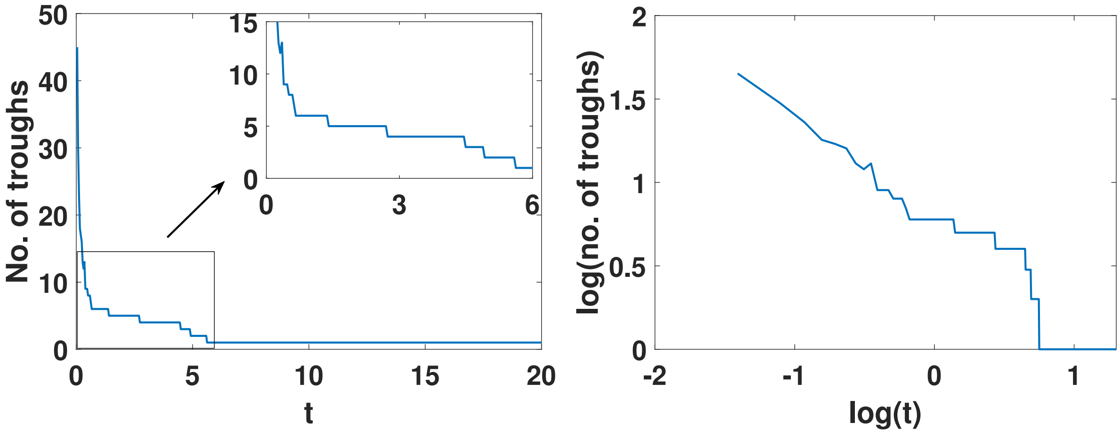

(a) (b)

Figure 5.4: Number of ***troughs*** on the front against the time t for the MS equation (5.2.1) when $L_x = L_y = 8$, (a) and (b) are the same data but (b) has log_{10} scales.

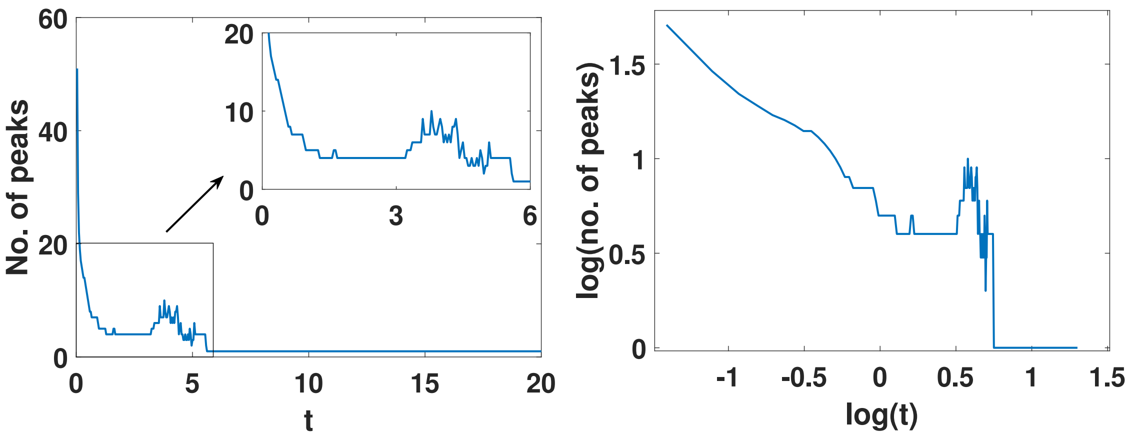

(a) (b)

Figure 5.5: Number of ***peaks*** on the front against the time t for the MS equation (5.2.1) when $L_x = L_y = 8$, (a) and (b) are the same data but (b) has log_{10} scales.

Second, we seek the numerical solution of the MS equation in two dimensions which is corresponding to the stable green solution in the bifurcation diagram when L_x and L_y are in the interval $[6, 10]$. For instance we choose $L_x = L_y = 8$. The front is shown to undergo a continuous reduction in the number of troughs and peaks. The dynamics of the front is coarsening until it reaches a steady state solution with one peak and one trough. The coarsening of reduction in the number of troughs is observed clearly in figure 5.4. However, in the case of reduction in the number of peaks, figure 5.5, a strange intermediate stage is spotted. The strange intermediate stage shows an unexpected increase and decrease in the number of peaks. In other words, when two or more peaks try to merge some extra small peaks are created between them and disappear again at the time of merging. To follow that intermediate stage, we choose a sequence of figures 5.6 that shows this circumstance at different times, which is the number of peaks is 4 when the time $t = 2.5$ therefore when these four peaks try to merge three extra peaks are created between them and becomes 7 peaks at $t = 3.75$ then disappear again and becomes 4 at $t = 5.4$ until it reaches one peak at $t = 6$.

We have taken a band of other examples when L_x and L_y are in the interval $[2, 32]$, it shows the same indications which is the dynamics of the front coarsens until it reaches the steady state solution with one peak and one trough. It should be noted that for the large domain the coarsening after the expected number of peaks, from the linear theory, has fast decay. In other words, the fast decay of the number of peaks and troughs is more clear in the large domain. For example, the numerical simulation of the MS equation in two dimensions in domain size 32 for both directions shows the same process as the previous cases. We expect almost 64 troughs on

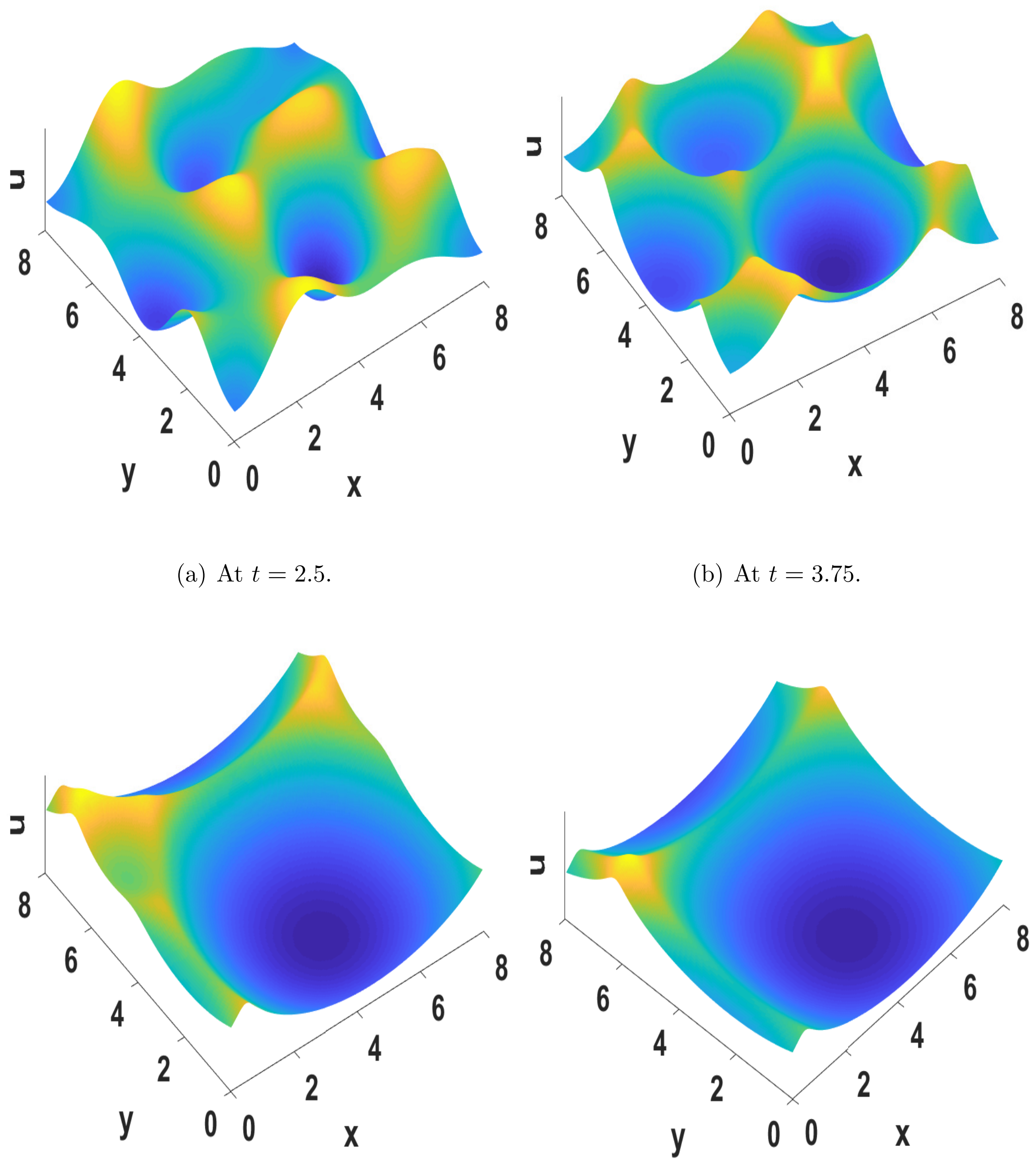

(a) At $t = 2.5$.

(b) At $t = 3.75$.

(c) At $t = 5.4$

(d) At $t = 6$.

Figure 5.6: Snapshots of development of the front dynamics based on the MS equation (5.2.1) when $L_x = L_y = 8$.

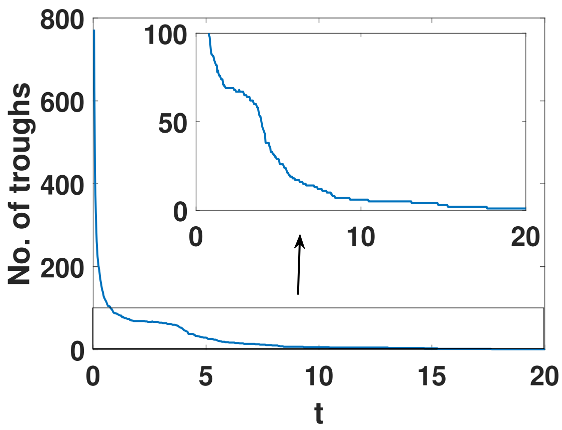

(a)

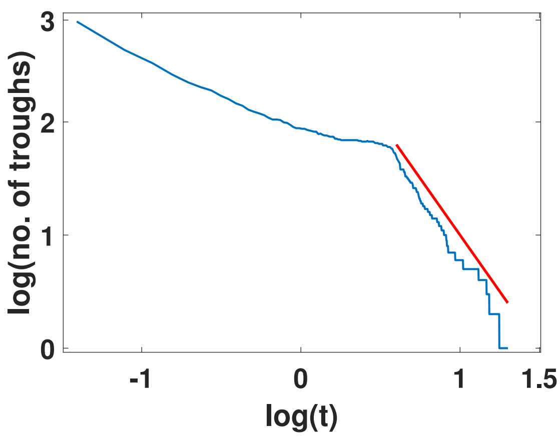

(b)

Figure 5.7: Number of ***troughs*** on the front against the time t for the MS equation (5.2.1) when $L_x = L_y = 32$, (a) and (b) are the same data but (b) has log_{10} scales.

the front due to the linear theory. Thus the dynamics of the front coarsens until it reaches close to that expected number of troughs and stay close to that number for a while. At late times the coarsening exhibits temporal power-law form with slope roughly -2, figure 5.7. Meanwhile, the number of peaks has the same strange phenomenon like the above examples, which is the fluctuation of the number of peaks in the intermediate stage, figure 5.8.

Finally due to the fact that the one-dimensional numerical solution of the MS equation is unstable where the domain size is greater than 32 (or $k < \frac{\pi}{16}$), we take a specific example and find the numerical solution of the MS equation in two dimensions when the domain size L_x and L_y are greater than 32. The sequence of figures 5.9 presents the numerical simulation of the MS equation in two dimensions when the domain size is 40 in both directions. The simulation illustrates the front

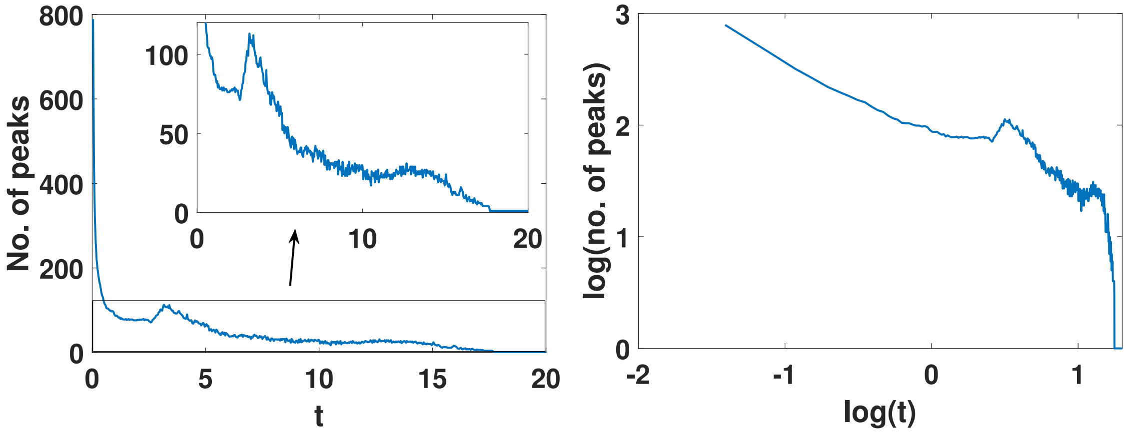

(a) (b)

Figure 5.8: Number of ***peaks*** on the front against the time t for the MS equation (5.2.1) when $L_x = L_y = 32$, (a) and (b) are the same data but (b) has log_{10} scales.

propagation from the initial disturbances then coarsens until it reaches one giant peak and one trough, then the dynamics of the front seems to be unstable and small peaks are appearing on the front and moving toward the giant peak and disappearing. In addition, in this example as the dynamics of the front coarsens the same circumstance which is fluctuations in the number of peaks as the previous case happens in some stages when peaks try to merge.

We have found the numerical solution of the MS equation in two dimensions for many examples when both L_x and L_y or one of them is greater than 32. All these simulations show that the dynamics of the front is unstable. This shows that the dynamics of the front for the MS equation in two dimensions is unstable when the domain size in one or both directions is greater than 32.

Consequently all the results we have found in this chapter motivate us to seek the

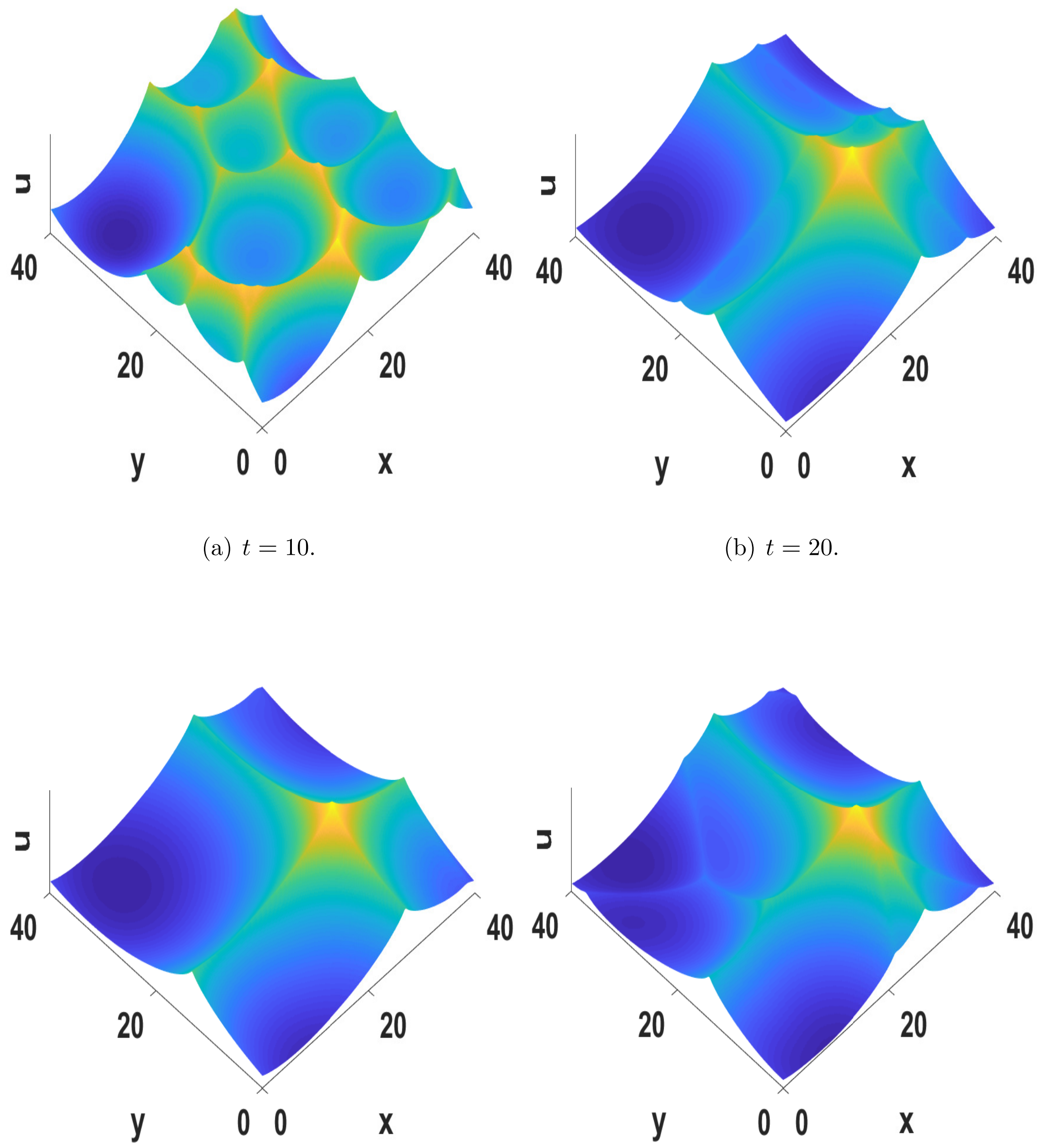

(a) $t = 10$.

(b) $t = 20$.

(c) $t = 25$.

(d) $t = 30$.

Figure 5.9: Snapshots of development of the front dynamics based on the MS equation (5.2.1) when $L_x = L_y = 40$.

analytical solution of the MS equation in two dimensions, which is done in the next section 5.3.

5.2.3 Speed of the front

Now we have solved MS equation in two dimensions numerically in order to determine the speed of the front for different domain sizes. The minimum point of the front is plotted at different times. This allows us to determine the asymptotic speed of the front that is observed after an initial transient.

Figure 5.10 presents the speed of the front in different domain sizes based on the MS equation in two dimensions. It shows that the speed of the front in all examples that have been mentioned above is almost constant. The speed of the front is $s = -9.87$ in the domain size $L_x = L_y = 4$ and $L_x = L_y = 8$, figure 5.10(a) and 5.10(b). However the speed is $s = -10.4$ in the domain size $L_x = L_y = 32$, figure 5.10(c). The speed is $s = -13.4$ when the domain size is 40 in both directions, figure 5.10(d).

5.3 Analytical solution of the MS equation in two dimensions

In this section, we find the analytical solution of the MS equation in two dimensions. We rely on the analytical solution of the MS equation in one dimension and the numerical solution of the MS equation in two dimensions. Here we compare a cross-section of the full numerical solution in two dimensions with the one-dimensional analytical solution of the MS equation.

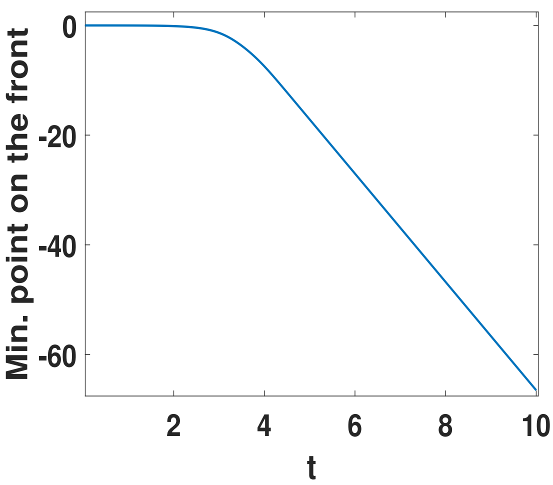

(a) When $L_x = L_y = 4$.

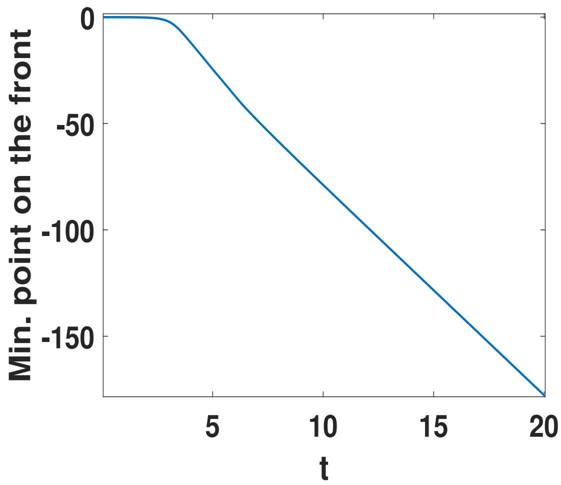

(b) When $L_x = L_y = 8$.

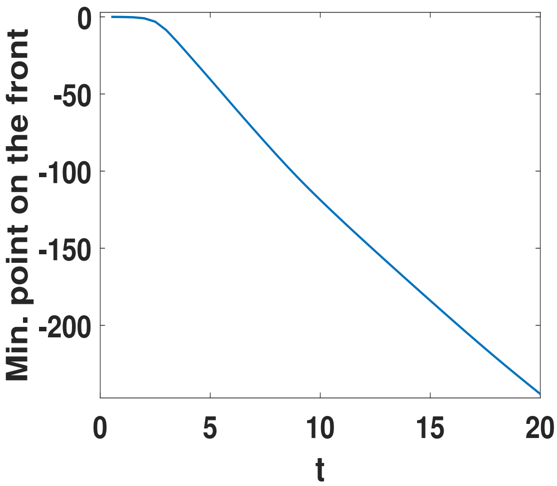

(c) When $L_x = L_y = 32$.

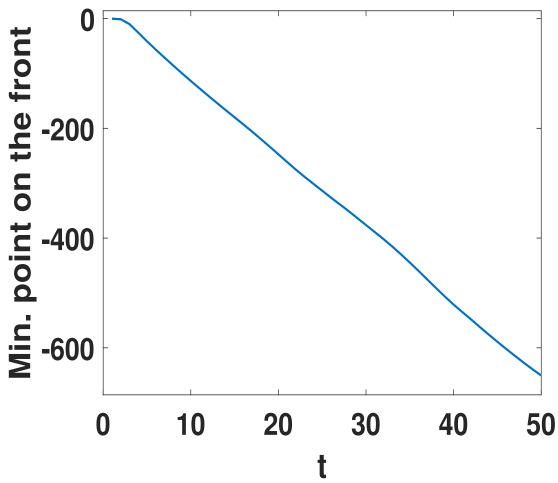

(d) When $L_x = L_y = 40$.

Figure 5.10: The location of the minimum point of the front in each time for the numerical solution of the MS equation in two dimensions.

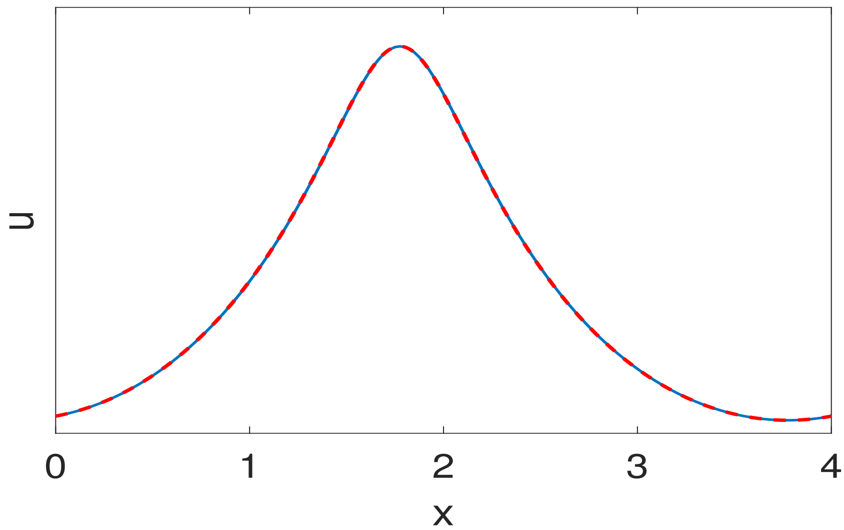

Figure 5.11: The comparison between a cross-section of two-dimensional numerical solution of the MS equation along the ***x-axis***, solid blue line, with the one dimension analytical solution (5.3.1), dashed red line, when $L = L_x = L_y = 4$.

In chapter 4 we have found that the analytical solution of the MS equation in one dimension which is corresponding to the black curve in the bifurcation diagram 4.1, where $\frac{\pi}{3} \leq k \leq \pi$ (or the domain sizes are in the interval [2, 6]), is

$$u(x,t) = -2\log\left(1 \pm \sqrt{1 - \frac{k^2}{\pi^2}}\cos(kx)\right) + 2k(k-\pi)t. \tag{5.3.1}$$

Thus we take a cross-section of the two-dimensional numerical solution, figure 5.1(d), along the x-axis and compare with the one-dimensional analytical solution (5.3.1) where $k = k_x = \frac{\pi}{2}$ $(L = L_x = 4)$, it shows that they fit very well where is difficult to see both curves perfectly, figure 5.11. Similarly for the other dimension if we take a cross-section of the numerical solution in two dimensions along the y-axis and compare it with the analytical solution (5.3.1) where $k = k_y = \frac{\pi}{2}$ they also agree very well, figure 5.12.

In section 5.2.3 we have calculated the speed of the front in the numerical simulation

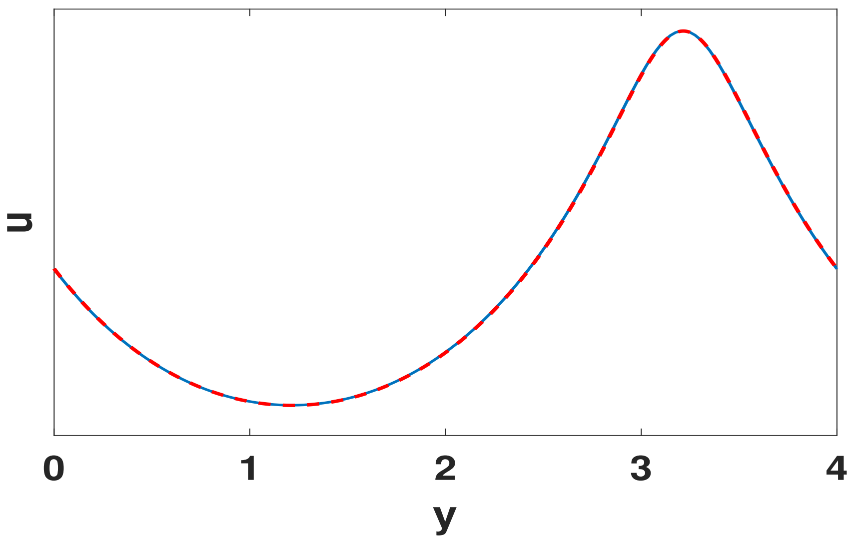

Figure 5.12: The comparison between a cross-section of two-dimensional numerical solution of the MS equation along the ***y-axis***, solid blue line, with the one-dimensional analytical solution (5.3.1), dashed red line, when $L = L_x = L_y = 4$.

for two-dimensional MS equation. For the same example above we find the speed which is $s = -9.87$. This is identical to twice the speed in the analytical solution in one dimension when $k = \frac{\pi}{2}$ $(L = 4)$ which is $s = 2k(k - \pi)$.

We apply the same idea above for a different values of $k_x = k_y$ in the interval $[\frac{\pi}{3}, \pi]$ and we get the same indications. First a cross-section of the numerical solution of the MS equation in two dimensions along each x and y direction is corresponding to the analytical solution in one dimension when $k = k_x$ and $k = k_y$ respectively. Second the speed of the front in two dimensions is equal to twice the front speed of the one-dimensional analytical solution when $k_x = k_y$ which shows that the speed in two dimensions is $s = 2k_x(k_x - \pi) + 2k_y(k_y - \pi)$.

Even when k_x and k_y are not equal we get the same thing for cross-sections. However the speed of the front in two dimensions is equal to sum of two speeds of one-dimensional analytical solutions one of them when $k = k_x$ and the other when $k = k_y$, which means the speed is $s = 2k_x(k_x - \pi) + 2k_y(k_y - \pi)$.

Therefore all the above signals confirm that the analytical solution of the MS equation in two dimensions when k_x and $k_y \in [\frac{\pi}{3}, \pi]$ (L_x and $L_y \in [2, 6]$) is the sum of two one-dimensional analytical solutions. Then it can be written as

$$u(x, y, t) = -2\log\Big(\big(1 + \sqrt{1 - \frac{k_x^2}{\pi^2}}\cos(k_x x)\big)\Big) - 2\log\Big(\big(1 + \sqrt{1 - \frac{k_y^2}{\pi^2}}\cos(k_y y)\big)\Big) + \Big(2k_x(k_x - \pi) + 2k_y(k_y - \pi)\Big)t, \quad (5.3.2)$$

We apply the same technique to the values of k_x and k_y in the interval $[\frac{\pi}{5}, \frac{\pi}{3}]$ (L_x and $L_y \in [6, 10]$) and investigate it carefully, we notice that the cross-section of each dimension of the two-dimensional numerical solution agrees with the one-dimensional analytical solution

$$u(x, t) = -2\log\Big(1 + \sqrt{\frac{16}{9} - \frac{8k^2}{\pi^2}}\cos(kx) + \big(\frac{1}{3} - \frac{3k^2}{\pi^2}\big)\cos(2kx)\Big) + 4k(2k - \pi)t, \quad (5.3.3)$$

and the speed of the front is $s = 4k_x(2k_x - \pi) + 4k_y(2k_y - \pi)$. Thus it shows that the two-dimensional analytical solution of the MS equation when k_x and $k_y \in [\frac{\pi}{5}, \frac{\pi}{3}]$ (L_x and $L_y \in [6, 10]$) is

$$u(x, y, t) = -2\log\Big(\big(1 + \sqrt{\frac{16}{9} - \frac{8k_x^2}{\pi^2}}\cos(k_x x) + \big(\frac{1}{3} - \frac{3k_x^2}{\pi^2}\big)\cos(2k_x x)\big)\Big) - 2\log\Big(\big(1 + \sqrt{\frac{16}{9} - \frac{8k_y^2}{\pi^2}}\cos(k_y y) + \big(\frac{1}{3} - \frac{3k_y^2}{\pi^2}\big)\cos(2k_y y)\big)\Big) + \Big(4k_x(2k_x - \pi) + 4k_y(2k_y - \pi)\Big)t. \quad (5.3.4)$$

In the case of one of the k_x and k_y is in the interval $[\frac{\pi}{3}, \pi]$ and the other is in the interval $[\frac{\pi}{5}, \frac{\pi}{3}]$, for instance k_x is in the first one and k_y is in the second one the analytical solution of the MS equation in two dimensions is

$$u(x,y,t) = -2\log\Big(\Big(1+\sqrt{1-\frac{k_x^2}{\pi^2}}\cos(k_x x)\Big)\Big) - 2\log\Big(\Big(1+\sqrt{\frac{16}{9}-\frac{8k_y^2}{\pi^2}}\cos(k_y y) + \Big(\frac{1}{3}-\frac{3k_y^2}{\pi^2}\Big)\cos(2k_y y)\Big)\Big) + \Big(2k_x(k_x-\pi)+4k_y(2k_y-\pi)\Big)t. \quad (5.3.5)$$

All the above analysis indicate that the front dynamics behaviour based on the MS equation in two dimensions shows very similar behaviour to the one-dimensional front dynamics. Thus we see it is necessary to confirm it by the weakly nonlinear analysis which has been done in the next section.

5.4 Weakly nonlinear analysis

Due to the similarity of the front dynamics behaviour in one and two dimensions cases we have chosen a value of k near to the bifurcation point $k = \pi$ and substitute it in the MS equation to seek the solution of the MS equation. Then we can write u as a perturbation expansion

$$u = \epsilon u_1 + \epsilon^2 u_2 + \epsilon^3 u_3 + O(\epsilon^4), \quad (5.4.1)$$

where u_1, u_2, u_3, ... are O(1). We rescale k and time,

$$k = k_0 + \epsilon^2 k_2, \qquad t = \frac{1}{\epsilon^2}T. \quad (5.4.2)$$

We use two time scales, so we replace $\frac{\partial}{\partial t}$ by $\frac{\partial}{\partial t} + \epsilon^2\frac{\partial}{\partial T}$. Thus by substituting (5.4.1) into the MS equation (5.2.1) and equating the terms with the same order, we get the following

$$\epsilon\frac{\partial u_1}{\partial t}+\epsilon^3\frac{\partial u_1}{\partial T}+\epsilon^2\frac{\partial u_2}{\partial t}+\epsilon^3\frac{\partial u_3}{\partial t}+O(\epsilon^4)=\epsilon\Big(\frac{\partial^2 u_1}{\partial x^2}+\frac{\partial^2 u_1}{\partial y^2}\Big)+\epsilon^2\Big(\frac{\partial^2 u_2}{\partial x^2}+\frac{\partial^2 u_2}{\partial y^2}\Big)$$
$$+\epsilon^3\Big(\frac{\partial^2 u_3}{\partial x^2}+\frac{\partial^2 u_3}{\partial y^2}\Big)-\frac{1}{2}\Big(\big(\epsilon\frac{\partial u_1}{\partial x}+\epsilon^2\frac{\partial u_2}{\partial x}+\epsilon^3\frac{\partial u_3}{\partial x}\big)^2+\big(\epsilon\frac{\partial u_1}{\partial y}+\epsilon^2\frac{\partial u_2}{\partial y}+\epsilon^3\frac{\partial u_3}{\partial y}\big)^2\Big)$$
$$+\epsilon\frac{1}{4\pi}\int_{-\infty}^{\infty}|\mathbf{k}|e^{i\mathbf{k}(\mathbf{x}-\mathbf{x}^*)}\Big(\epsilon u_1(\mathbf{x}^*,t)+\epsilon^2 u_2(\mathbf{x}^*,t)+\epsilon^3 u_3(\mathbf{x}^*,t)\Big)d\mathbf{k}d\mathbf{x}^*. \quad (5.4.3)$$

At $O(\epsilon)$ we have

$$\frac{\partial u_1}{\partial t}=\frac{\partial^2 u_1}{\partial x^2}+\frac{\partial^2 u_1}{\partial y^2}+\frac{1}{4\pi^2}\int_{-\infty}^{\infty}\int_{-\infty}^{\infty}|\mathbf{k}|e^{i\mathbf{k}(\mathbf{x}-\mathbf{x}^*)}u_1(\mathbf{x}^*,t)d\mathbf{k}d\mathbf{x}^*. \quad (5.4.4)$$

We can suggest that the solution of (5.4.4) is

$$u_1=a(T)\cos(kx)+b(T)\cos(ky), \quad (5.4.5)$$

where a and b are functions of T. Substituting this solution in (5.4.4) and equating the terms with the same order leads to

$$0=-ak_0^2\cos(kx)-bk_0^2\cos(ky)+a|k_0|\pi\cos(kx)+b|k_0|\pi\cos(ky).$$

Equating coefficients of $\cos(kx)$ leads to

$$k_0=\pi,$$

that means k_2 should be negative because we have chosen a k as a point near to the bifurcation point π on the bifurcation diagram 4.1 which is less than π. Now at $O(\epsilon^2)$ the equation (5.4.3) becomes

$$\frac{\partial u_2}{\partial t}=\frac{\partial^2 u_2}{\partial x^2}+\frac{\partial^2 u_2}{\partial y^2}-\frac{1}{2}\Big(\big(\frac{\partial u_1}{\partial x}\big)^2+\big(\frac{\partial u_1}{\partial y}\big)^2\Big)$$
$$+\frac{1}{4\pi^2}\int_{-\infty}^{\infty}\int_{-\infty}^{\infty}|\mathbf{k}|e^{i\mathbf{k}(\mathbf{x}-\mathbf{x}^*)}u_2(\mathbf{x}^*,t)d\mathbf{k}d\mathbf{x}^*. \quad (5.4.6)$$

By using the general solution of u_1 this suggests that u_2 has the solution

$$u_2=a_2(T)\cos(2kx)+b_2(T)\cos(2ky)+c_2t, \quad (5.4.7)$$

where c_2 is constant. Then by substituting the general solution of u_1 (5.4.5) and u_2 (5.4.7) in (5.4.6) and equating the terms of the same order we get

$$c_2 = -4a_2\pi^2\cos(2kx) - 4b_2\pi^2\cos(2ky) - \frac{1}{2}\Big(\frac{1}{2}a^2\pi^2 - \frac{1}{2}a^2\pi^2\cos(2kx) + \frac{1}{2}b^2\pi^2 - \frac{1}{2}b^2\pi^2\cos(2ky)\Big) + 2a_2\pi^2\cos(2kx) + 2b_2\pi^2\cos(2ky). \quad (5.4.8)$$

Then by equating the coefficients of $\cos(2kx)$, $\cos(2ky)$ and the coefficients without cosine we get

$$c_2 = -\frac{1}{4}a^2\pi^2 - \frac{1}{4}b^2\pi^2 \quad (5.4.9)$$

$$0 = -4a_2\pi^2 + \frac{1}{4}a^2\pi^2 + 2a_2\pi^2 \quad (5.4.10)$$

$$0 = -4b_2\pi^2 + \frac{1}{4}b^2\pi^2 + 2b_2\pi^2. \quad (5.4.11)$$

The last two equations give

$$a_2 = \frac{a^2}{8}, \qquad b_2 = \frac{b^2}{8}.$$

By using the general solution of u_1 (5.4.5) and u_2 (5.4.7), the equation (5.4.3) at $O(\epsilon^3)$ becomes

$$\frac{\partial u_1}{\partial T} + \frac{\partial u_3}{\partial t} = -2\pi a k_2\cos(kx) - 2\pi b k_2\cos(ky) + \Big(\frac{\partial^2 u_3}{\partial x^2} + \frac{\partial^2 u_3}{\partial y^2}\Big) - \frac{1}{2}\Big(\Big(-\pi a\sin(kx)\Big)\Big(-2\pi a_2\sin(2kx)\Big) + \Big(-\pi b\sin(ky)\Big)\Big(-2\pi b_2\sin(2ky)\Big)\Big) + \pi a k_2\cos(kx) + \pi b k_2\cos(ky) + \frac{1}{4\pi}\int_{-\infty}^{\infty}\int_{-\infty}^{\infty}|\mathbf{k}|e^{i\mathbf{k}(\mathbf{x}-\mathbf{x}^*)}u_3(\mathbf{x}^*,t)d\mathbf{k}d\mathbf{x}^*. \quad (5.4.12)$$

Now we suggest the solution of u_3 is

$$u_3 = a_3(T)\cos(3kx) + b_3(T)\cos(3ky). \quad (5.4.13)$$

Substituting the solution of u_3 (5.4.13) in (5.4.12), we get

$$\frac{\partial a}{\partial T}\cos(kx) + \frac{\partial b}{\partial T}\cos(ky) = -2\pi a k_2 \cos(kx) - 2\pi b k_2 \cos(ky) - 9\pi^2 a_3 \cos(3kx) - 9\pi^2 b_3 \cos(3ky) - 2\pi^2 a a_2\Big(\cos(kx) - \cos(3kx)\Big) - 2\pi^2 b b_2\Big(\cos(ky) - \cos(3ky)\Big) + \pi a k_2 \cos(kx) + \pi b k_2 \cos(ky) + 3\pi^2 a_3 \cos(3kx) + 3\pi^2 b_3 \cos(3ky). \quad (5.4.14)$$

Then by equating the coefficients of $\cos(kx)$ and $\cos(ky)$ we get the following two amplitude differential equations

$$\frac{\partial a}{\partial T} = -\pi k_2 a - \frac{\pi^2}{8} a^3 \quad (5.4.15)$$

$$\frac{\partial b}{\partial T} = -\pi k_2 b - \frac{\pi^2}{8} b^3. \quad (5.4.16)$$

In general amplitude equations for pattern formation systems have ab^2 term in the first amplitude equation (5.4.15) and ba^2 in the second equation (5.4.16), [32]. These two terms are zero in the MS system which means that there is no interaction between both dimensions. Thus it confirms that the dynamics of the front has similar behaviour in one and two dimensions. The last two equations give

$$a^2 = \frac{-8k_2}{\pi} \qquad \text{and} \qquad b^2 = \frac{-8k_2}{\pi},$$

which is also confirming that k_2 is negative.

The system of two equations (5.4.15) and (5.4.16) has four stationary solutions. One of them is stable when both a and b are non-zero and the others are unstable when a, b or both are zero.

In addition, there are more solutions to the MS equation in two dimensions which are the rotated solutions. The first one is the rotated solution by 45 degrees. Thus we can write this solution as $u = \sin(k_x x + k_y y)$, which is shown in the figure 5.13.

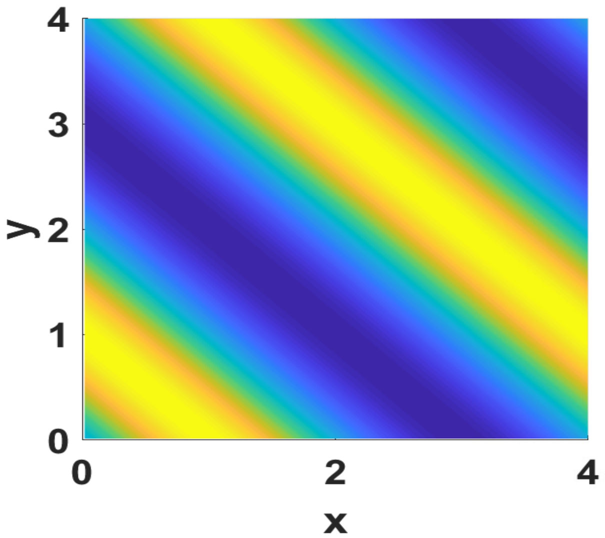

Figure 5.13: The rotation solution of the MS equation in two dimensions by 45 degrees.

The second solution, $u = \sin(k_x x - k_y y)$, is the rotated solution by 135 degrees. Finally the combination of both solutions which is shown in figure 5.14. All these solutions are unstable solutions because when we start the simulation with one of these solutions as an initial condition, the simulation ends with the single peak solution.

Furthermore we have shown in the previous section, from equation (5.3.2), that the speed of front is $s = 2k_x(k_x - \pi) + 2k_y(k_y - \pi)$ where k_x and k_y are in the interval $[\frac{\pi}{3}, \pi]$. Thus where $k = k_x = k_y$ and we rescale k as $k = \pi + \epsilon^2 k_2$, then the speed of the front becomes $s = 4\epsilon^2 \pi k_2 + O(\epsilon^4)$. Moreover the value of c_2, when $a^2 = b^2 = \frac{-8k_2}{\pi}$, from (5.4.9) is

$$c_2 = \frac{-1}{2}\left(\frac{-8k_2}{\pi}\pi^2\right) = 4k_2\pi$$

Now $c_2 T = 4\epsilon^2 k_2 \pi t$ which is equal to st.

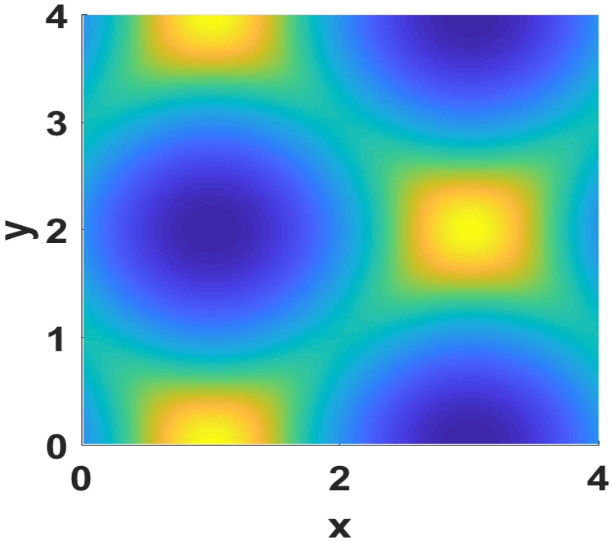

Figure 5.14: The combination of both rotation solutions of the MS equation in two dimensions.

5.5 Numerical solution of the nonlocal-KS and MMS equations in two dimensions

In this section, we present numerical simulations of the nonlocal-KS and MMS equations and illustrate the transition of the dynamics of the front from chaotic random initial condition patterns. The simulations use periodic boundary conditions and employ a Fourier spectral method for the spatial discretization. In addition, we use ETD with time step size 0.002 for time discretization.

5.5.1 The nonlocal-KS equation in two dimensions

The nonlocal-KS equation in two dimensions can be written as

$$\begin{aligned}\frac{\partial u(x,y,t)}{\partial t} = \frac{\partial^4 u}{\partial x^4} + 2\frac{\partial^4 u}{\partial x^2 \partial y^2} + \frac{\partial^4 u}{\partial y^4} - \frac{\partial^2 u}{\partial x^2} - \frac{\partial^2 u}{\partial y^2} \\ - \frac{1}{2}\Big((\frac{\partial u}{\partial x})^2 + (\frac{\partial u}{\partial y})^2 \Big) + \epsilon I, \quad (5.5.1)\end{aligned}$$

where I is a nonlocal term written as a Fourier transformation

$$I = \frac{1}{4\pi}\int_{-\infty}^{\infty} |\mathbf{k}| e^{i\mathbf{k}.(\mathbf{x}-\mathbf{x}^*)} u(\mathbf{x}^*, t) d\mathbf{k} d\mathbf{x}^*.$$

The simulation for the nonlocal-KS equation in a certain time, for $\epsilon = 0.1$, in a domain of size 64 in both dimensions, is shown in figure 5.15. The simulation illustrates the transition from random initial patterns to chaotic dynamics.

In general, the nonlocal-KS equation with small parameter ϵ has the same behaviour as the KS equation for large domain size (when the domain size is roughly greater than 4π in one or both directions). Thus the nonlocal-KS equation with small parameter ϵ and large domain is fully unstable with no coherent structure and has chaotic dynamics. However, it has a stable steady state solution with one peak and one trough for a small domain (when the domain size is roughly less than 3π in both directions). However the travelling wave solution is observed between small and large domain.

Furthermore, the numerical simulation for the nonlocal-KS equation with $\epsilon = 1$ and domain size 64 in both dimensions shows the same chaotic unstable behaviour. Figure 5.16 shows the fluctuation of the number of peaks and troughs on the front which confirm that the dynamics of the front is unstable and has chaotic dynamics. Thus in the case of a larger domain (when the domain size is roughly greater than 4π in one or both directions), the dynamics of the front is still unstable, meanwhile the coarsening phenomenon can be seen in the decreasing of the number of peaks and troughs on the front. For instance figure 5.17 shows the number of peaks and troughs based on the simulation of the nonlocal-KS equation with the domain size 32π in both directions. For a small domain (when the domain size is roughly less

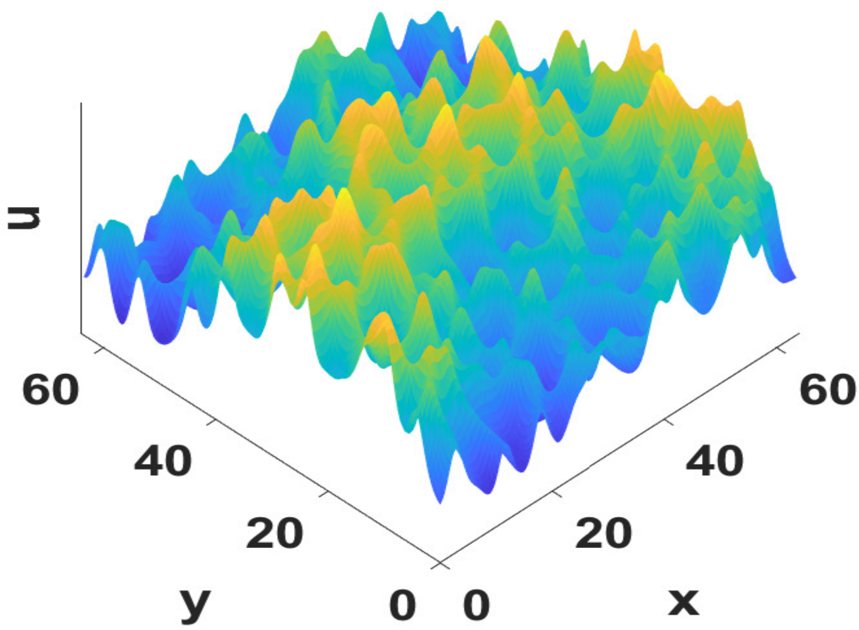

Figure 5.15: The numerical simulation of the nonlocal-KS equation in two dimensions (5.5.1), when $\epsilon = 0.1$ and $L = 64$ in both directions at $t = 100$.

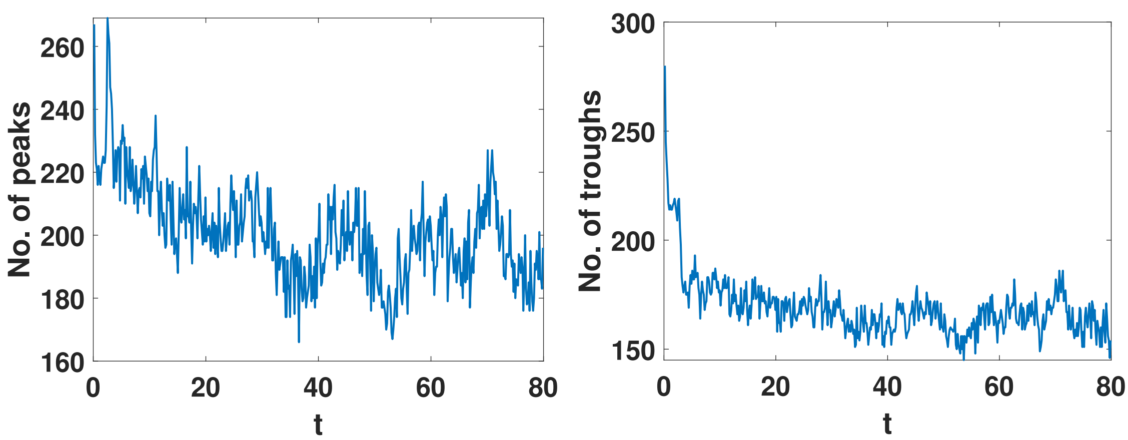

(a) ***Peaks*** (b) ***Troughs***

Figure 5.16: Number of peaks and troughs on the front against the time t for the nonlocal-KS equation (5.5.1) when $\epsilon = 1$ and $L_x = L_y = 64$.

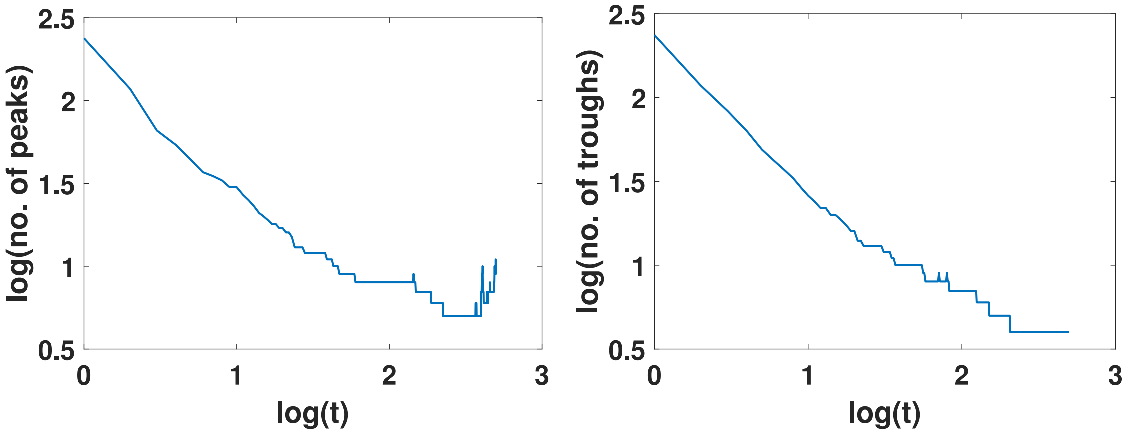

(a) ***Peaks*** (b) ***Troughs***

Figure 5.17: Number of peaks and troughs on the front against the time t, have log_{10} scales, for the nonlocal-KS equation (5.5.1) when $\epsilon = 1$ and $L_x = L_y = 32\pi$.

than 2π in both directions), the numerical simulation shows that the nonlocal-KS equation has a stable steady state solution with one peak and one trough. However the travelling wave solution is found between the small and large domain. Figure 5.18 shows the travelling wave solution for the nonlocal-KS equation when the single cusp travels at a constant speed diagonally.

5.5.2 The MMS equation in two dimensions

The MMS equation in two dimensions can be written as follows

$$\frac{\partial u(x,y,t)}{\partial t} = \frac{\partial^2 u}{\partial x^2} + \frac{\partial^2 u}{\partial y^2} - \frac{1}{2}\Big(\big(\frac{\partial u}{\partial x}\big)^2 + \big(\frac{\partial u}{\partial y}\big)^2\Big) + \epsilon I, \tag{5.5.2}$$

where I is a nonlocal term written as a Fourier transformation

$$I = \frac{1}{4\pi}\int_{-\infty}^{\infty}\int_{-\infty}^{\infty} |\mathbf{k}|e^{-|\mathbf{k}|}e^{i\mathbf{k}.(\mathbf{x}-\mathbf{x}^*)}u(\mathbf{x}^*,t)d\mathbf{k}d\mathbf{x}^*.$$

The numerical simulation of the MMS equation (5.5.2) when $\epsilon = 1$ and $L_x = L_y = 64$, shows that the front dynamics also has similar behaviour to the one-dimensional

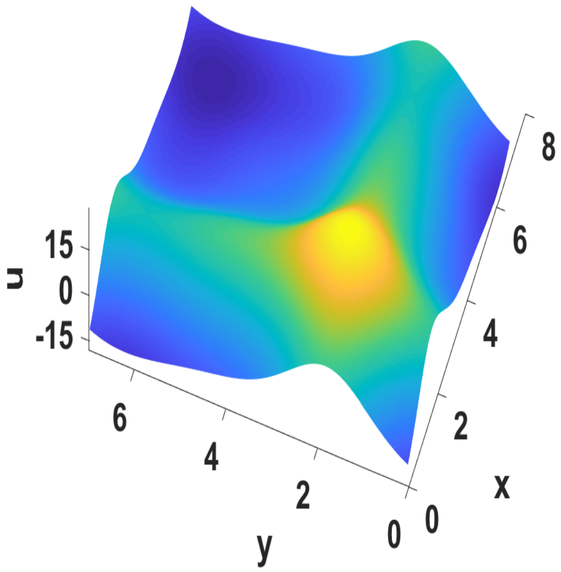

(a) When $t = 48.5$.

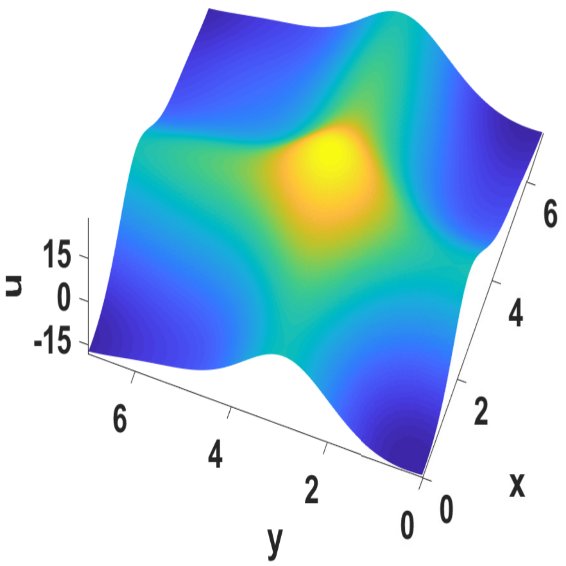

(b) When $t = 49$.

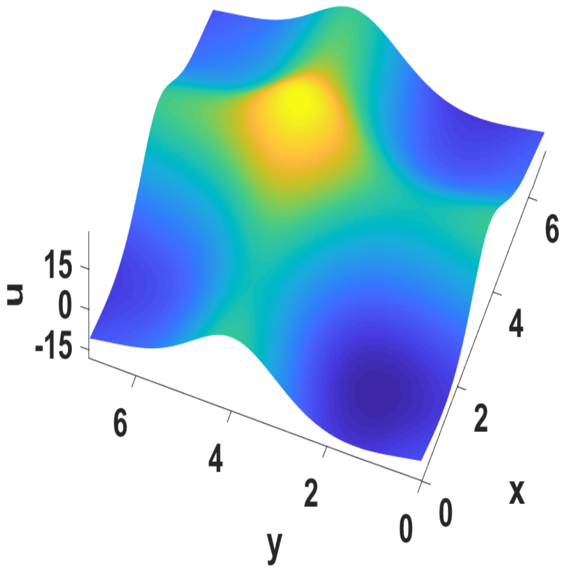

(c) When $t = 49.5$.

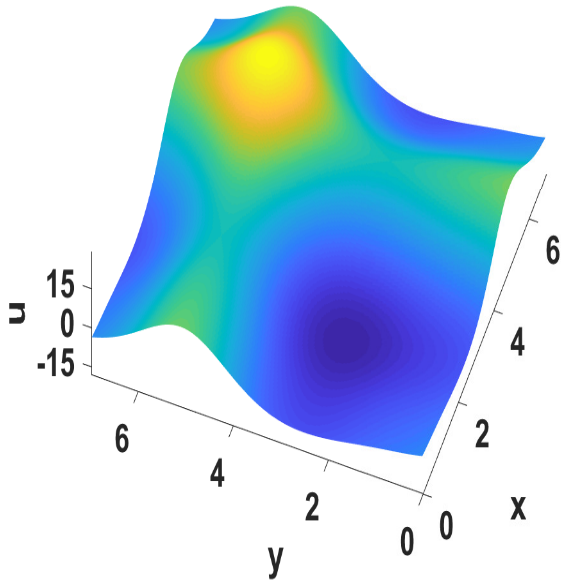

(d) When $t = 50$.

Figure 5.18: Snapshots of the development of the front dynamics for the nonlocal-KS (5.5.1) when $\epsilon = 1$ and $L_x = L_y = 2.2\pi$.

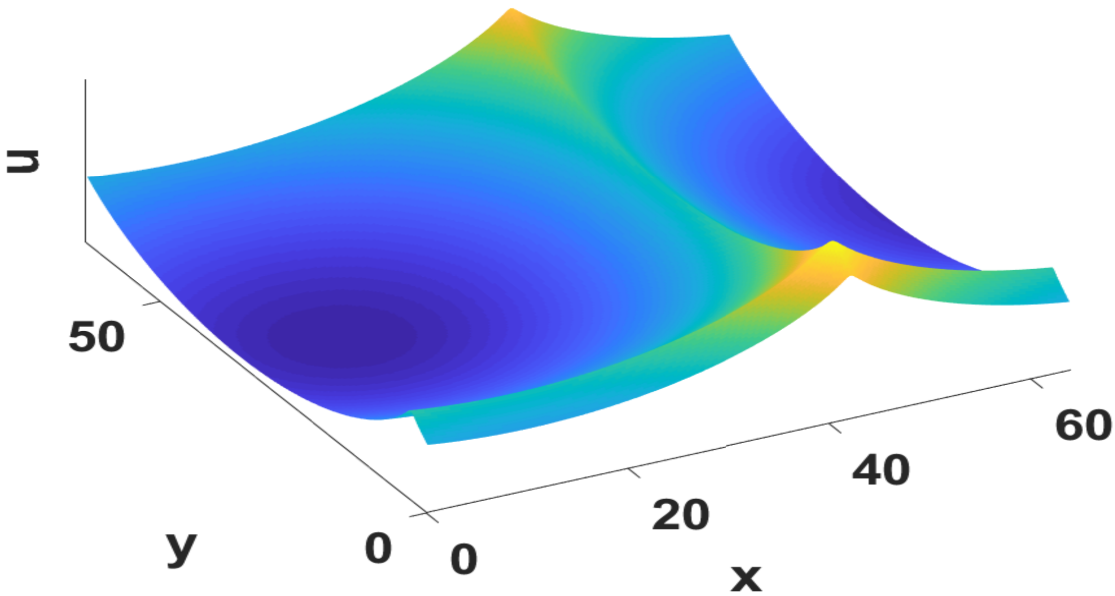

Figure 5.19: The numerical simulation of the MMS equation in two dimensions (5.5.2), when $\epsilon = 1$ and the domain size is 64 in both directions.

simulation. The dynamics of the front in two dimensions evolves from the small random initial condition. It has a huge number of peaks and troughs in the initial stage then starts to decrease until it reaches a stable steady state solution with one peak and one trough, figure 5.19. As the nonlocal-KS equation, here the number of peaks and troughs are not the same. A clear coarsening is spotted with the decreasing in troughs number, figures 5.20. At late times the coarsening shows temporal power-law form with slope roughly -3, figure 5.20(b). Also, the strange intermediate phenomenon is observed in the reduction in the number of peaks, see figure 5.21.

Note that the front dynamics simulation of the MMS equation in two dimensions has the steady state solution with a single peak and single trough when the domain size of both directions are less than L_c where $L_c \approxeq 30\pi$. However, when the domain

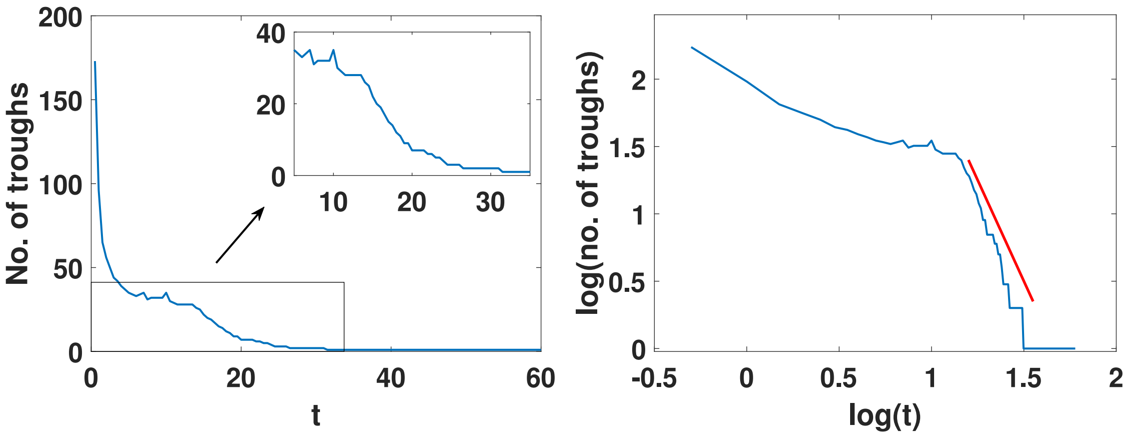

(a) (b)

Figure 5.20: Number of ***troughs*** on the front against the time t for the MMS equation (5.5.2) when $\epsilon = 1$ and $L_x = L_y = 64$, (a) and (b) are the same data but (b) has log_{10} scales.

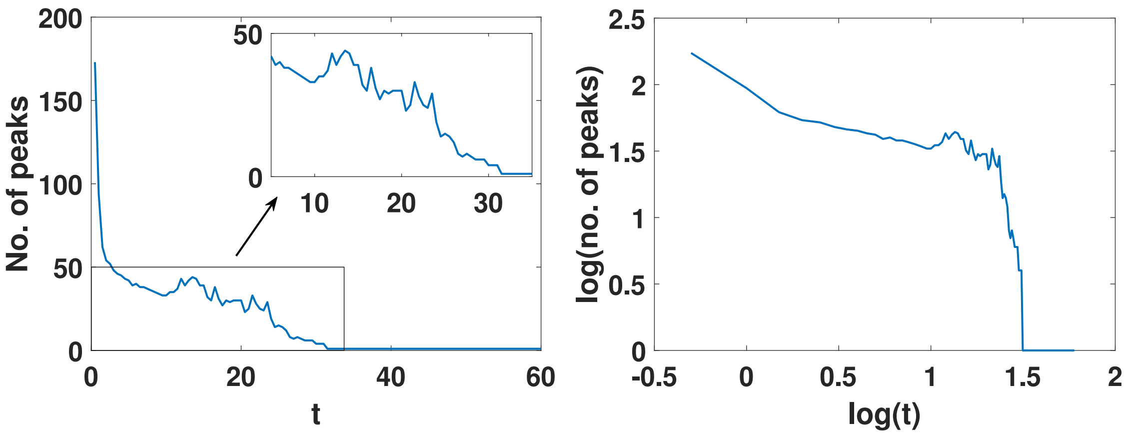

(a) (b)

Figure 5.21: Number of ***peaks*** on the front against the time t for the MMS equation (5.5.2) when $\epsilon = 1$ and $L_x = L_y = 64$, (a) and (b) are the same data but (b) has log_{10} scales.

size of one of the directions or both of them are greater than L_c, the dynamics of the front is coarsening until a single trough appears. This seems to be unstable, with some small troughs appearing and disappearing on the large trough. This is similar to the behaviour of the MS equation shown in figure 5.9.

In the case of small parameter $\epsilon = 0.1$, the simulation has the same behaviour just the difference is the simulation need run for a long time to remove transient features. Thus the dynamics of the front has a stable steady state solution with one peak and one trough when the domain size of both directions are less than L_n where $L_n < 104\pi$, while it is unstable when the domain size of one direction or both greater than L_n.

5.6 Conclusion

In this chapter, we have exhibited full numerical simulations of all three nonlocal-KS (5.5.1), MS (5.2.1) and MMS (5.5.2) systems in two dimensions. In addition, we have found a family of analytical solutions of the MS equation in two dimensions.

Numerically the dynamics of the front transition is illustrated from chaotic random initial patterns. In these simulations, we have used periodic boundary conditions and employ a Fourier spectral method for the spatial discretization. The ETD method is used for time stepping.

In general, the dynamics of the front based on the MS equation in two dimensions changes from a random chaotic initial condition to a steady state solution with one peak and one trough for small domain in both directions. In contrast to the one-dimensional case, the number of peaks and troughs are not equal in two dimensions. We have observed a coarsening in the decreasing of the number of troughs until getting a single trough. In the decreasing of the number of peaks, we noticed a strange phenomenon in the intermediate stage which is the fluctuation of the number of peaks. However, for a large domain, the dynamics of the front becomes unstable.

The numerical simulation shows that the nonlocal-KS equation in two dimensions is fully unstable with no coherent structure for a large domain and small parameter ϵ. Although for large parameter ϵ and a large domain in both directions we can see a coarsening in the reduction of the number of troughs, the system still unstable. The numerical simulations show that the system has a stable steady state solution with one peak and one trough for a small domain in both directions. In addition, the travelling wave solution has been found between small and large domain.

The MMS system almost has the same behaviour as the MS equation which is transforming from chaotic dynamics to the steady state stationery with a single peak and trough for a small domain in both directions. Also, the coarsening is observed in the decreasing of the troughs number and the fluctuation intermediate stage in the number of peaks is noticed. In addition, for a large domain, the dynamics of the front becomes unstable.

Note that in general all numerical simulations in two dimensions show very similar behaviour to the one-dimensional simulation. We have confirmed the similarity by weakly nonlinear analysis for the MS equation. This motivated us to find a family of analytical solutions of the MS equation in two dimensions.

We have compared the analytical solution of the MS equation in one dimension with a cross-section of the numerical solution in two dimensions. This comparison seems to agree very well, that gives us the confirmation that the solution of the MS equation in two dimensions is the sum of two one-dimensional solutions. In addition, we have found the speed of front to be the sum of the speed of two one-dimensional speed.

Chapter 6

Conclusions and further work

6.1 Conclusions

Front propagation and interface motion appear in many scientific subjects, such as invasive species, avalanche, combustion, solidification and many other industrial processes. It is a fundamental problem to understand the characteristics of front propagation such as front instabilities, front speeds, front profiles, and front locations.

This work's objective is to look into, suggest, resolve, and discuss possible models for front instabilities that suit the shapes of fronts observed in applications better than the Kuramoto-Sivashinsky equation. We have specifically dealt with systems which have the growth rate proportional to $|k|$ for small wavenumber k where the front dynamics takes different shapes such as lobe-and-cleft patterns. We have particularly taken into consideration the models that include nonlocal effects. In this work, we have examined three nonlocal equations which are nonlocal Kuramoto-Sivashinsky (5.5.1), Michelson-Sivashinsky (5.2.1) and modified Michelson-Sivashinsky (5.5.2).

In 1977 Sivashinsky [67] derived the nonlocal Kuramoto-Sivashinsky (nonlocal-KS) equation while in the same year Michelson and Sivashinsky [50] derived the Michelson-Sivashinsky (MS) equation. We have modified the MS equation by changing the nonlocal term to obtain the front shape that fits better in applications and referred to it as the modified Michelson-Sivashinsky (MMS) equation.

In chapter 2, we have nondimensionalized all the three models and found the growth rate of them. The nonlocal-KS equation and MMS equation have one parameter ϵ. We have put the parameter in front of the nonlocal term to find the effect of the nonlocal term on the system. The nonlocal-KS, MS and MMS equations have been explored numerically by Fourier spectral discretization and the time discretized by ETD1 method.

The nonlocal-KS equation with small domain for a band of k values has a stable steady state solution with one cusp. Also, there is a travelling wave solution for a band of k values. This agrees very well with the bifurcation diagram 3.12 of the nonlocal-KS equation in chapter 3. Note that in chapter 3, we have found the approximate analytical solution of all three nonlocal front equations by truncated Fourier series. Moreover, we have obtained in the numerical simulation that there is a heteroclinic solution for a band of k values. For larger domain when $\epsilon = 1$, the numerical solutions show that the nonlocal-KS equation shows coarsening from initial disturbances as time progress which finally leads to one peak in the front dynamics. This single peak seems to be unstable and new cusps appear in the trough and move toward the giant cusp. However for a large domain when $\epsilon = 0.1$ there is no coarsening and the dynamics of the front stays unstable and has the same behaviour as the KS equation.

For the MS equation there is no travelling wave solution. The dynamics of the front for the MS equation with small domain has a stable steady state solution with one cusp. These solutions agree very well with the stable solutions that have been found by truncated Fourier series in chapter 3. The numerical simulation shows that the coarsening phenomenon appears in this system. However for the larger domain, the dynamics of the front coarsens until it reaches two cusps and then becomes unstable and new cusps appear on the troughs and move toward crests.

The MMS model for the small domain has a stable steady state solution with one cusp, while for the large domain the dynamics of the front is coarsening until it reaches a few cusps which are unstable, then new cusps appear on troughs and move toward the tops. The interesting point here is that even for a small value of ϵ the dynamics of the front still has the same behaviour. Note that the stable solutions of this system which are found by numerical simulations also agree very well with the stable solution found by truncated Fourier series in chapter 3.

Furthermore, we have found that the speed of front and amplitude of the waves that are found in the numerical simulation in chapter 2 are very close to that found by the truncated Fourier series in chapter 3, particularly for the stable solutions. In chapter 3, we have found the bifurcation diagram for all three models. In the bifurcation diagram of the MS equation, figure 3.7, we have found that the bifurcation points are $\frac{\pi}{3}$, $\frac{\pi}{5}$, $\frac{\pi}{7}$ and so on. This motivated us to seek analytical solutions of the MS equation.

In chapter 4, we have obtained a family number of analytical solutions of the MS equation in the infinite domain. The speed of the front is zero in this case. Moreover, we have found a family number of analytical solutions for the MS equation in the periodic domain. Also, we have obtained the formula of the speed of the front for all these solutions.

After all the work we have done in one dimension, it was important to seek the solution of all three front models in two dimensions. Chapter 5 is concerned with finding the solutions of all three equations in two dimensions numerically and finding the analytical solution of the MS equation in two dimensions. The numerical simulation shows that the dynamics of the front based on the nonlocal-KS equation in two dimensions is fully unstable with no coherent structure for the large domain and a small parameter ϵ. Although for the large domain and large parameter ϵ the solution is unstable, the coarsening phenomenon is observed in the number of peaks and troughs. However for a small domain in both directions, the system has a stable steady state solution with one peak and one trough. The travelling wave solution is obtained between small and large domain.

In general, the dynamics of the front based on the MS equation in two dimensions coarsens from small disturbances, due to the small random initial condition, until it reaches a stable steady state solution with one cusp and one trough for a small domain in both directions. In contrast to the one dimensional case, in two dimensions the number of peaks and troughs are not equal. The coarsening phenomenon is more clear in the number of troughs than the number of peaks. The dynamics of the front is unstable for the large domain.

The numerical simulations in two dimensions show that the MMS equation has almost the same behaviour as the MS equation. The dynamics of the front is coarsening until it reaches a stable steady state solution with one peak and one trough for the small domain in both directions. However, it is unstable for the large domain.

Finally, we have found the analytical solution of the MS equation in two dimensions, which is the sum of the two one-dimensional solutions. Also, the speed of the front in two dimensions is the sum of the speed of the two one-dimensional speeds.

In general, the dynamics of the front for all three models have similar behaviour except for some features. The dynamics of the front which has a steady state solution with one cusp for the nonlocal-KS equation has the sharpest cusp among them while for the MMS equation has the smoothest one for the same domain. In addition, the nonlocal-KS equation has the largest amplitude dynamics of the front among them while the MMS equation has the smallest. Last but not least, the travelling wave and the heteroclinic cycle solutions have been found in the nonlocal-KS equation while there are no such solutions for the MS and MMS equation. Finally, the MMS equation forms a stable coherent structure front for a larger domain than the others, while the MS equation forms a stable coherent structure front for a larger domain than the nonlocal-KS equation.

6.2 Further work

Finally, we suggest a few directions for further work.

- In chapter 3, we have found the solution of the MS and MMS equations by truncated Fourier series. In the bifurcation diagrams 3.7 and 3.11, we have observed fluctuating solutions for small k. We will investigate that they are numerical errors or real solutions.

- In chapter 4, we have obtained the analytical solution of the MS equation for some values of k. We will try to find further analytical solutions of the MS equation for all values of k for small values of k when the solution is stable.

- We will try to find real applications that fit with the shape of the front with each of these nonlocal front models and compare with them.

Bibliography

[1] M. J. Ablowitz and A. Zeppetella. Explicit solutions of Fisher's equation for a special wave speed. *Bulletin of Mathematical Biology*, 41(6):835–840, 1979.

[2] G. Akrivis and Y.-S. Smyrlis. Implicit–explicit BDF methods for the Kuramoto–Sivashinsky equation. *Applied Numerical Mathematics*, 51(2-3):151–169, 2004.

[3] L. J. Allen. *An Introduction to Mathematical Biology*. Pearson/Prentice Hall, 2007.

[4] A.-L. Barabási and H. E. Stanley. *Fractal concepts in surface growth*. Cambridge university press, 1995.

[5] H. Bateman. Some recent researches on the motion of fluids. *Monthly Weather Review*, 43(4):163–170, 1915.

[6] E. Ben-Jacob, H. Brand, G. Dee, L. Kramer, and J. Langer. Pattern propagation in nonlinear dissipative systems. *Physica D: Nonlinear Phenomena*, 14(3):348–364, 1985.

[7] J. Billingham. Dynamics of a strongly nonlocal reaction–diffusion population model. *Nonlinearity*, 17(1):313, 2003.

[8] H. Bockhorn, P. Habisreuther, and M. Hettel. Numerical modelling of technical combustion. In *100 Volumes of 'Notes on Numerical Fluid Mechanics'*, pages 325–340. Springer, 2009.

[9] M. Böckmann and S. C. Müller. Growth rates of the buoyancy-driven instability of an autocatalytic reaction front in a narrow cell. *Physical Review Letters*, 85(12):2506, 2000.

[10] N. F. Britton. Spatial structures and periodic travelling waves in an integro-differential reaction-diffusion population model. *SIAM Journal on Applied Mathematics*, 50(6):1663–1688, 1990.

[11] N. F. Britton et al. *Reaction-diffusion equations and their applications to biology.* Academic Press, 1986.

[12] R. S. Cantrell and C. Cosner. *Spatial ecology via reaction-diffusion equations.* John Wiley & Sons, 2004.

[13] J.-D. Chen. Radial viscous fingering patterns in Hele-Shaw cells. *Experiments in fluids*, 5(6):363–371, 1987.

[14] Z. Chen, G. Huan, and Y. Ma. *Computational methods for multiphase flows in porous media.* SIAM, 2006.

[15] H. Cooper. A hypothesis concerning the dynamic balance of fresh water and salt water in a coastal aquifer. *Journal of Geophysical Research*, 64(4):461–467, 1959.

[16] S. M. Cox and P. C. Matthews. Exponential time differencing for stiff systems. *Journal of Computational Physics*, 176(2):430–455, 2002.

[17] G. Darrieus. Propagation d'un front de flamme. *La Technique Moderne*, 30:18, 1938.

[18] A. De Wit. Fingering of chemical fronts in porous media. *Physical Review Letters*, 87(5):054502, 2001.

[19] G. Dee and J. Langer. Propagating pattern selection. *Physical Review Letters*, 50(6):383, 1983.

[20] F. Elmer. Nonlinear and nonlocal dynamics of spatially extended systems: stationary states, bifurcations and stability. *Physica D: Nonlinear Phenomena*, 30(3):321–342, 1988.

[21] R. M. Engeman, N. Paige Groninger, and D. S. Vice. A general model for predicting brown tree snake capture rates. *Environmetrics: The official journal of the International Environmetrics Society*, 14(3):295–305, 2003.

[22] P. C. Fife. *Mathematical aspects of reacting and diffusing systems*, volume 28. Springer Science & Business Media, 2013.

[23] R. A. Fisher. The wave of advance of advantageous genes. *Annals of eugenics*, 7(4):355–369, 1937.

[24] N. Fogla. Interplay between background turbulence and Darrieus-Landau instability in premixed flames via a model equation, M.S. Thesis at University of Illinois at Urbana-Champaign, 2010.

[25] X. Fu, L. Cueto-Felgueroso, and R. Juanes. Viscous fingering with partially miscible fluids. *Physical Review Fluids*, 2(10):104001, 2017.

[26] A. Gorguis. A comparison between Cole-Hopf transformation and the decomposition method for solving Burgers' equations. *Applied Mathematics and Computation*, 173(1):126–136, 2006.

[27] I. S. Gradshteyn and I. M. Ryzhik. *Table of integrals, series, and products.* Academic press, 2014.

[28] A. Gross, O. Holdenrieder, M. Pautasso, V. Queloz, and T. N. Sieber. Hymenoscyphus pseudoalbidus, the causal agent of european ash dieback. *Molecular Plant Pathology*, 15(1):5–21, 2014.

[29] B. Gustafsson and A. Vasil'ev. *Conformal and potential analysis in Hele-Shaw cells.* Springer Science & Business Media, 2006.

[30] E. Hanert, E. Schumacher, and E. Deleersnijder. Front dynamics in fractional-order epidemic models. *Journal of theoretical biology*, 279(1):9–16, 2011.

[31] C. Härtel, F. Carlsson, and M. Thunblom. Analysis and direct numerical simulation of the flow at a gravity-current head. part 2. the lobe-and-cleft instability. *Journal of Fluid Mechanics*, 418:213–229, 2000.

[32] R. Hoyle. *Pattern formation: an introduction to methods.* Cambridge University Press, 2006.

[33] J. M. Hyman, B. Nicolaenko, and S. Zaleski. Order and complexity in the Kuramoto-Sivashinsky model of weakly turbulent interfaces. *Physica D: Nonlinear Phenomena*, 23(1-3):265–292, 1986.

[34] S. Kalliadasis, J. Yang, and A. De Wit. Fingering instabilities of exothermic reaction-diffusion fronts in porous media. *Physics of fluids*, 16(5):1395–1409, 2004.

[35] E. Khain and L. M. Sander. Dynamics and pattern formation in invasive tumor growth. *Physical Review Letters*, 96(18):188103, 2006.

[36] H. Kobayashi, T. Tamura, K. Maruta, T. Niioka, and F. A. Williams. Burning velocity of turbulent premixed flames in a high-pressure environment. In *Symposium (International) on Combustion*, volume 26, pages 389–396. Elsevier, 1996.

[37] A. Kolmogorov, I. Petrovskii, and N. Piskunov. A study of the equation of diffusion with increase in the quantity of matter, and its application to a biological problem. *Bjul. Moskovskogo Gos. Univ*, 1(7):1–26, 1937.

[38] Y. Kuramoto. Instability and turbulence of wavefronts in reaction-diffusion systems. *Progress of Theoretical Physics*, 63(6):1885–1903, 1980.

[39] Y. Kuramoto and T. Tsuzuki. Persistent propagation of concentration waves in dissipative media far from thermal equilibrium. *Progress of theoretical Physics*, 55(2):356–369, 1976.

[40] Y. Lan and P. Cvitanović. Unstable recurrent patterns in Kuramoto-Sivashinsky dynamics. *Physical Review E*, 78(2):026208, 2008.

[41] L. Landau. On the theory of slow combustion. *Acta physicochim. URSS*, 19(1):77–85, 1944.

[42] J. Langer and H. Müller-Krumbhaar. Mode selection in a dendritelike nonlinear system. *Physical Review A*, 27(1):499, 1983.

[43] J. S. Langer. Instabilities and pattern formation in crystal growth. *Reviews of Modern Physics*, 52(1):1, 1980.

[44] M. A. Liberman. *Introduction to physics and chemistry of combustion: explosion, flame, detonation.* Springer Science & Business Media, 2008.

[45] A. Lipatnikov. *Fundamentals of premixed turbulent combustion.* CRC Press, 2012.

[46] S. Lowe, M. Browne, S. Boudjelas, and M. De Poorter. *100 of the world's worst invasive alien species: a selection from the global invasive species database*, volume 12. Invasive Species Specialist Group Auckland, 2000.

[47] A. Manickam, K. Moudgalya, and A. Pani. Second-order splitting combined with orthogonal cubic spline collocation method for the Kuramoto-Sivashinsky equation. *Computers & Mathematics with Applications*, 35(6):5–25, 1998.

[48] M. Matalon. Intrinsic flame instabilities in premixed and nonpremixed combustion. *Annu. Rev. Fluid Mech.*, 39:163–191, 2007.

[49] H. Meinhardt. Models of biological pattern formation. *New York*, 1982.

[50] D. Michelson and G. Sivashinsky. Nonlinear analysis of hydrodynamic instability in laminar flames—II. Numerical experiments. *Acta Astronautica*, 4(11-12):1207–1221, 1977.

[51] D. Michelson and G. Sivashinsky. Thermal-expansion induced cellular flames. *Combustion and flame*, 48:211–217, 1982.

[52] I. Milkov. Basic Avalanche Safety. http://skibansko.bg/blog/basic-avalanche-safety-1/#prettyPhoto, 2016. [online; accessed 16 Oct. 2019].

[53] R. Mittal and G. Arora. Quintic B-spline collocation method for numerical solution of the Kuramoto–Sivashinsky equation. *Communications in Nonlinear Science and Numerical Simulation*, 15(10):2798–2808, 2010.

[54] J. D. Murray. *Mathematical Biology. II Spatial Models and Biomedical Applications* {*Interdisciplinary Applied Mathematics V. 18*}. Springer-Verlag New York Incorporated, 2001.

[55] J. D. Murray. *Mathematical biology I: An introduction, Vol. 17 of interdisciplinary applied mathematics*. Springer, New York, NY, USA,, 2002.

[56] J. Neufeld. Lobe-cleft patterns in the leading edge of a gravity current. *Master's Thesis, University of Toronto*, 2002.

[57] A. Novick-Cohen. Interfacial instabilities in directional solidification of dilute binary alloys: the Kuramoto-Sivashinsky equation. *Physica D: Nonlinear Phenomena*, 26(1):403–410, 1987.

[58] P. Pelcé and A. Libchaber. *Dynamics of curved fronts*. Elsevier, 2012.

[59] S. P. Pudasaini and K. Hutter. *Avalanche dynamics: dynamics of rapid flows of dense granular avalanches*. Springer Science & Business Media, 2007.

[60] Y. Rastigejev and M. Matalon. Nonlinear evolution of hydrodynamically unstable premixed flames. *Journal of Fluid Mechanics*, 554:371–392, 2006.

[61] T. s Vicsek. *Fractal growth phenomena*. World scientific, 1992.

[62] P. G. Saffman and G. I. Taylor. The penetration of a fluid into a porous medium or Hele-Shaw cell containing a more viscous liquid. *Proceedings of*

the Royal Society of London. Series A. Mathematical and Physical Sciences, 245(1242):312–329, 1958.

[63] B. Sandnes, E. Flekkøy, H. Knudsen, K. Måløy, and H. See. Patterns and flow in frictional fluid dynamics. *Nature communications*, 2:288, 2011.

[64] T. Shlang and G. Sivashinsky. Irregular flow of a liquid film down a vertical column. *Journal de Physique*, 43(3):459–466, 1982.

[65] B. I. Shraiman. Order, disorder, and phase turbulence. *Physical Review Letters*, 57(3):325, 1986.

[66] G. Sivashinsky. Diffusional-thermal theory of cellular flames. *Combustion Science and Technology*, 15(3-4):137–145, 1977.

[67] G. Sivashinsky. Nonlinear analysis of hydrodynamic instability in laminar flames—I. Derivation of basic equations. *Acta astronautica*, 4(11):1177–1206, 1977.

[68] G. Sivashinsky and D. Michelson. On irregular wavy flow of a liquid film down a vertical plane. *Progress of theoretical Physics*, 63(6):2112–2114, 1980.

[69] G. I. Sivashinsky. Instabilities, pattern formation, and turbulence in flames. *Annual Review of Fluid Mechanics*, 15(1):179–199, 1983.

[70] J. G. Skellam. Random dispersal in theoretical populations. *Biometrika*, 38(1/2):196–218, 1951.

[71] A. Soika, F. Dinkelacker, and A. Leipertz. Pressure influence on the flame front curvature of turbulent premixed flames: comparison between experiment and theory. *Combustion and flame*, 132(3):451–462, 2003.

[72] N. Swaminathan and K. N. C. Bray. *Turbulent premixed flames*. Cambridge University Press, 2011.

[73] O. Thual, U. Frisch, and M. Henon. Application of pole decomposition to an equation governing the dynamics of wrinkled flame fronts. In *Dynamics of Curved Fronts*, pages 489–498. Elsevier, 1988.

[74] A. M. Turing. The chemical basis of morphogenesis. *Bulletin of mathematical biology*, 52(1-2):153–197, 1990.

[75] M. Uddin, S. Haq, et al. A mesh-free numerical method for solution of the family of Kuramoto–Sivashinsky equations. *Applied Mathematics and Computation*, 212(2):458–469, 2009.

[76] T. Ureste. The Amazon Forest Fire. https://chargervoice.com/15149/news/the-amazon-forest-fire/, 2019. [online; accessed 16 Oct. 2019].